NASA CONTRACTOR REPORT

NASA CR-655

NASA CR-655

DEVELOPMENT AND APPLICATION OF A PHOTOELASTO-PLASTIC METHOD TO STUDY STRESS DISTRIBUTIONS IN VICINITY OF A SIMULATED CRACK

by A. R. Hunter and M. E. Schwarz

Prepared by
LOCKHEED AIRCRAFT CORPORATION
Sunnyvale, Calif.
for Langley Research Center

NATIONAL AERONAUTICS AND SPACE ADMINISTRATION • WASHINGTON, D. C. • DECEMBER 1966

NASA CR-655

DEVELOPMENT AND APPLICATION OF A PHOTOELASTO-PLASTIC METHOD TO STUDY STRESS DISTRIBUTIONS IN VICINITY OF A SIMULATED CRACK

By A. R. Hunter and M. E. Schwarz

Prepared under Contract No. NAS 1-4760 by
LOCKHEED AIRCRAFT CORPORATION
Sunnyvale, Calif.

for Langley Research Center

NATIONAL AERONAUTICS AND SPACE ADMINISTRATION

For sale by the Clearinghouse for Federal Scientific and Technical Information
Springfield, Virginia 22151 – Price $3.00

FOREWORD

This report has been prepared by Lockheed Missiles & Space Company for the Langley Research Center of the National Aeronautics and Space Administration under Contract No. NAS 1-4760. This report describes the development and application of a photoelasto-plastic method to study the elasto-plastic stress distributions in plates containing centrally located simulated cracks utilizing "frozen stress" techniques. The results are representative of aluminum alloys.

SUMMARY

The purpose of this program was to develop a photoelasto-plastic stress analysis method and to apply this method to study experimentally the stress distributions in the vicinity of simulated cracks. This method utilizes the frozen stress and creep characteristics of plastic materials to simulate the stress-strain behavior of aluminum alloys. During the development and verification of this method, two polymer materials were subjected to various thermal cycles, the maximum temperatures of which were significantly below the critical temperature. Below the critical temperature, polymer materials normally used in photoelasticity experience considerable creep. The strain and birefringence associated with this creep can be frozen into certain materials and subsequently sliced without relieving the frozen strain.

A material and thermal cycle was selected which exhibited an effective stress-strain curve similar to the uniaxial stress-strain behavior of 2024-T3 aluminum alloy. "Infinite plate" models were machined from the selected material and subjected to constant tensile load and the appropriate thermal cycle to simulate 2024-T3 aluminum. The infinite plate models contained centrally located holes 1/8in. in diameter.

Two thin plate models (1/8-in. thick) were subjected to tensile loads corresponding to $\sigma_\infty/\sigma_1 = 0.11$ and 0.71. The stress distribution along a centerline normal to the direction of loading was determined for the two cases of $\sigma_\infty/\sigma_1 = 0.11$ and 0.71.

Two thick plate models (0.4-in. thick) were subjected to tensile loads corresponding to $\sigma_\infty/\sigma_1 = 0.41$, 0.53. The stress distributions were determined adjacent to the hole along a line normal to the direction of load.

The method was then applied to plates containing centrally located simulated cracks. Crack lengths of 0.1, 0.5, and 0.8 in. were investigated for various plate thicknesses. For each crack length, plates with thicknesses of 0.1, 0.3, and 0.5 were each examined at two levels of plasticity. The stress distributions were determined adjacent to the crack tip along the line normal to the direction of load at the surface and the midplane.

The stress concentration factors determined for the infinite plates with centrally located holes are in very good agreement with theory. The stress concentration factor for the thick plates were slightly higher at the midplane of the plates than at the surface. Due to the higher stresses at the midplane of the thick plates, there results a σ_z stress normal to the load direction and parallel to the hole direction. This σ_z stress is maximum at the midplane and edge of hole and diminishes to zero a short distance from the hole.

Based on the elasto-plastic stress distributions determined for plates with centrally located simulated cracks, some general observations can be made. First, the stress component in the direction of the load has the maximum value, not at the crack tip, but a short distance from the tip. This is caused by the yield condition at the edge of the crack tip being one based on a uniaxial stress while at a short distance from the crack tip, the yield condition depends upon the biaxial stress state for the surface and a tri-axial state at the midplane. Second, the magnitude of the maximum σ_y stress occurs at approximately 6 to 7 mils from the crack tip. The magnitude of this stress tends to be higher at the midplane than at the surface. Third, at the midplane, at least for the thicker specimens, a rather high value for σ_z develops. It should also be noted that, similar to σ_x, the σ_z value is higher at a short distance from the crack tip than it is at the crack tip.

CONTENTS

ILLUSTRATIONS

Section 1
INTRODUCTION

1.1 SCOPE OF INVESTIGATION

The photoelasto-plastic method utilizes the creep and "frozen" stress characteristics exhibited by epoxy resins and other polymer materials when subjected to a thermal cycle whose maximum temperature is significantly less than the "critical" temperature of the material. The resulting "frozen" stress-strain behavior is characterized by the generation of nonlinear effective stress-strain curves. Effective stress-strain curves of this nature were generated for two polymer materials, an epoxy and a polycarbonate for various thermal cycles in order to arrive at a material and associated thermal cycle which could be used to simulate the stress-strain behavior of an aluminum alloy. Also the associated birefringence was determined (calibration). Stress-strain similarity was established by use of the Ramberg-Osgood method of stress-strain representation. Upon selection of an appropriate model material and thermal cycle, elasto-plastic stress distributions were determined for infinite plates with centrally located holes to verify the usefulness of the method. This photoelasto-plastic method of stress analysis was then applied to study stress distributions in the vicinity of a simulated crack.

1.2 BACKGROUND

Neuber (Ref. 1) has treated analytically the stress-distributions in the vicinity of a crack in an infinite plate. The analysis shows a very rapid decrease in stress level at the leading edge of the crack. Therefore, for small values of ℓ/w, the crack-length to plate-width ratio, an infinite plate behavior would be expected. For the case of intermediate values of ℓ/w, Brossman and Kies (Ref. 2) suggest that a correction factor be applied to the stress concentration factors as determined by Neuber's theory.

This correction factor is approximate and applies only for intermediate values of ℓ/w. According to Brossman and Kies, this correction factor is not necessary for values of ℓ/w less than 0.35. These methods are applicable only in the case of plane-stress.

The analytical solution of plane-stress plasticity problems of technical importance has proven to be forbiddingly complicated. Therefore, in recent years, attention has been given to experimental methods. The most popular experimental method is the use of bonded birefringent coatings. Wells and Post (Ref. 3) performed a photoelastic analysis of the dynamic stress distribution in the vicinity of a crack. Dixon (Ref. 4) has studied the effect of finite width for a centrally located crack. Dixon (Ref. 5) and Kawata (Ref. 6) have studied the elasto-plastic strain distributions for notches using the bonded birefringent coating method. Gerberich (Ref. 7) has applied the coating method to study strain distribution about a slowly growing crack. These methods assume elastic stress distributions and plane stress or only surface strains in the plastic range. It is known that even in the elastic range, the stress distribution is not uniform through the plate thickness for thick plates subjected to simple tension. This situation is more significant in the plastic range. Therefore, a three-dimensional method is needed. The developed photoelasto-plastic method described in this report could fulfill this need. In addition, this method could be utilized to study a wide variety of plasticity problems, particularly in design problems where it is desirable to utilize structural material in the plastic range to achieve high-strength and minimum-weight characteristics.

Section 2

TECHNICAL APPROACH

2.1 PHOTOELASTO-PLASTIC THEORY

The behavior of some photoelastic materials is elastic above a "critical" temperature. Therefore, using the "frozen stress" technique, it is possible to study three-dimensional elastic stress distribution in structural models by examination of slices removed from the models. This technique is well established and has provided very useful information concerning stress concentrations and stress distributions associated with very complex engineering structures.

At room temperature and temperature well below the critical temperature, some photoelastic materials experience a significant amount of creep. The occurrence of creep results in an effective stress-strain curve which is nonlinear. This behavior can be utilized in such a way as to provide a means of studying elasto-plastic stress distributions. The "frozen" stress feature provides for extension to three-dimensional situations.

The "frozen stress" method consists of application of a load to a transparent plastic model at room temperature. The model is then brought to the critical temperature of the model material and then slowly cooled (to prevent thermal stresses) to room temperature. Upon removal of the load a stress pattern similar to that which would have existed at room temperature may be observed. In addition, the model may be sliced without relieving the "frozen stress" fringe pattern. This photoelastic fringe pattern represents an elastic stress distribution. An understanding of this phenomena can be obtained by consideration of the "Multiphase Theory of Plastics" by Kuske*

*A. Kuske, "Multiphase Theory of Plastics," Experimental Mechanics, Sept. 1962, p. 278

Plastics may be considered to consist of two phases: an elastic phase and a plastic phase. Birefringence results from a contribution by each phase and can be expressed as

$$\Delta = C_p t(\sigma_1 - \sigma_2)_p + C_e t(\sigma_1 - \sigma_2)_e \quad (1)$$

where

c = stress optical coefficient
t = optical path
$\sigma_1 - \sigma_2$ = principal stress difference
p = pertaining to plastic phase
e = pertaining to elastic phase

The stress optical coefficients C_p and C_e are constants which depend upon the material. They are independent of temperature. The modulus of the elastic phase (E_e) is also independent of temperature. The modulus of the plastic phase (E_p) is a function of temperature, time and stress. When the photoelastic model is stressed, a portion of the stress is carried by each phase depending upon the relative modulus values of the two phases. At room temperature $E_p >> E_e$ and the stress in the elastic phase is insignificant. As the temperature is increased, the modulus E_p decreases and we find that the elastic phase carries more and more of the load until at the "critical" temperature ($E_p = 0$) all the load is carried by the elastic phase. Then Eq. (1) becomes

$$\Delta = C_e t(\sigma_1 - \sigma_2)_e \quad (2)$$

Therefore, the material behaves elastically at the "critical" temperature. Upon slowly cooling to room temperature, the plastic phase hardens, thus "freezing" the elastic phase in a state of deformation. Upon removal of the load, the photoelastic pattern remains. Slicing does not disturb this pattern since it is "frozen" on a molecular scale. Thus, slices may be removed from the model and stresses determined in the plane of the slices.

If a loaded photoelastic model is subjected to a thermal cycle of T_{max} significantly less than the critical temperature for the material, appreciable creep will be observed. In terms of the multi-phase theory, the modulus of the plastic phase diminishes with time and more load is carried by the elastic phase, resulting in a higher stress in this phase and greater elongation. Utilizing this creep feature, it is possible to generate an "effective" stress-strain curve that has nonlinear characteristics. "Effective" stress-strain curve refers to the relation between the "frozen stress" and strain defined as the permanent deformation per unit length measured after the specimen has undergone a specific thermal cycle.

If a simple tensile specimen experiences a given stress level (σ_1) at room temperature and then is subjected to a specific thermal cycle (Fig. 1) while under load, the resulting strain is composed of the elastic strain at maximum temperature and the strain resulting from creep which takes place during the thermal cycle. For various stress levels ($\sigma_1 > \sigma_2 > \sigma_3 > \ldots$), the resulting strains ($\epsilon_1 > \epsilon_2 > \epsilon_3 > \ldots$) are frozen into the material. From these data an effective stress-strain curve can be constructed which would represent the "frozen" stress-strain characteristics of the material for a given thermal cycle. Figure 2 represents a type of curve constructed in this manner. As a result of the "frozen" strain, there corresponds a birefringence which is also frozen into the material due to the loading and thermal cycle. Measurement of this birefringence yields a curve of the type shown in Fig. 3. This amounts to essentially the calibration.

After establishing the frozen stress-strain-birefringence characteristics for a given material and thermal cycle, a structural model may be subjected to a load system and the thermal cycle used in the calibration. Analysis of "frozen" birefringence in the structural model may then be interpreted in terms of the stress using the effective stress-birefringence curve. The experimental results obtained in this manner can be applied to any material that exhibited a stress-strain curve similar to the "effective" stress-strain obtained for the model material.

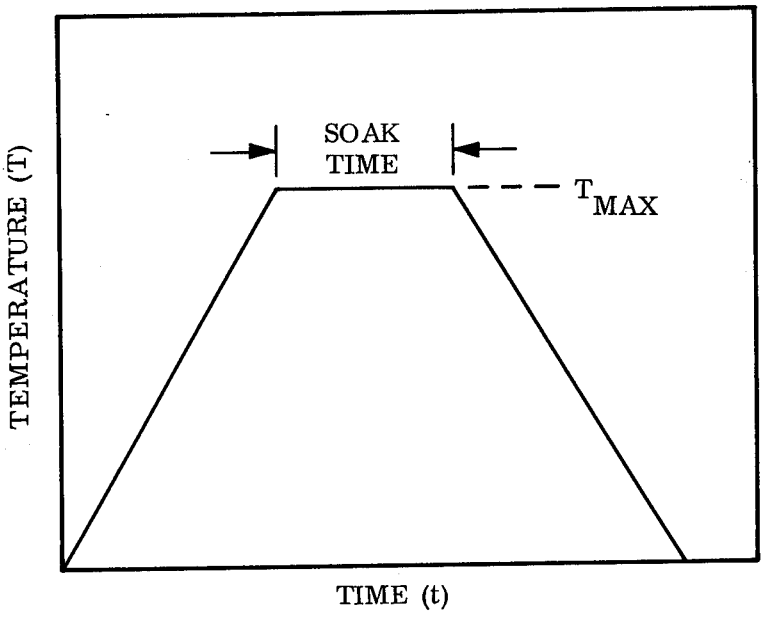

Fig. 1 Typical Thermal Cycle

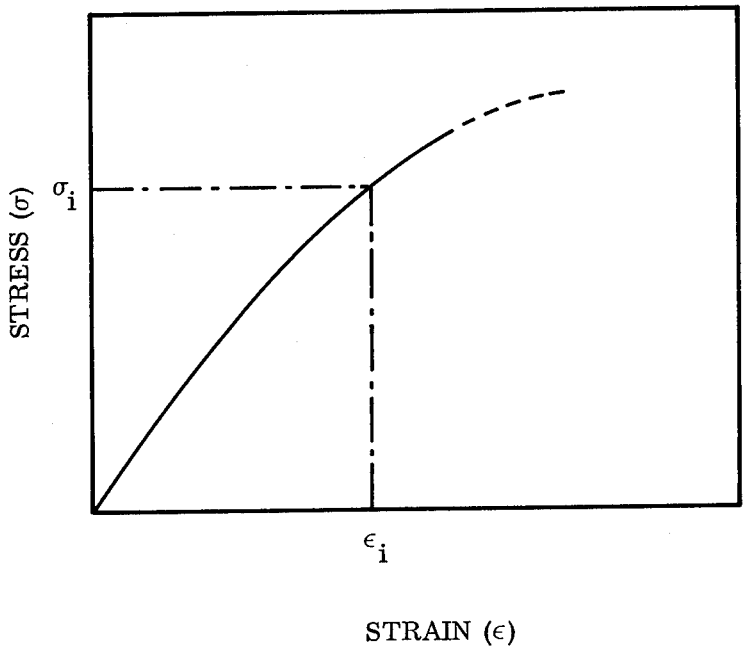

Fig. 2 Typical Effective Stress-Strain Curve

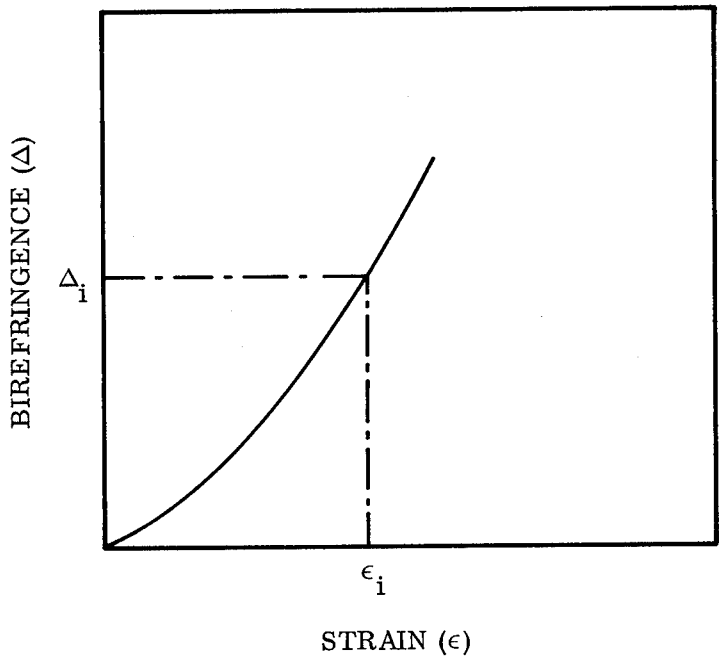

Fig. 3 Typical Birefringence Strain Curve

2.2 STRESS-STRAIN SIMILARITY

Ramberg and Osgood (Ref. 9) have suggested a relation to describe stress-strain curves for materials. This relationship is

$$e = \frac{S}{E} + K\left(\frac{S}{E}\right)^n \tag{3}$$

where

e = strain
S = stress
E = modulus of elasticity
K and n = material constants

This equation in dimensionless form is

$$\epsilon = \sigma + \frac{1 - m_1}{m_1}\sigma^n \tag{4}$$

where

$$\epsilon = \frac{eE}{S_1}$$

$$\sigma = \frac{S}{S_1}$$

S_1 = secant yield strength ($E_1 = m_1 E$)

Also, m_1 represents a chosen constant $0 < m_1 < 1$. Choosing $m_1 = 0.7$, Eq. (4) becomes

$$\epsilon = \sigma + \frac{3}{7}\sigma^n \tag{5}$$

Equation (5) represents all stress-strain curves which have the same shape factor n. Therefore, the "effective" stress-strain curve of the model material must have the same shape factor as the stress-strain curve for the prototype material in order that similarity exist.

Section 3

DEVELOPMENT AND VERIFICATION OF METHOD

3.1 CALIBRATION PHASE

3.1.1 Test Procedure

During the calibration phase of this program two materials were investigated, an epoxy resin cured with 10 pbw* of diethanolamine curing agent and a polycarbonate material.

The epoxy material was purchased in liquid resin form and cured in sheets 30 in. × 15 in. × 1/2 in. From these sheets 0.1-in. thick tensile specimens were machined. Even though the calibration specimens were only 0.1-in. thick, it was necessary to prepare them from thick plates so that the calibration would be applicable to the thick infinite plates, since the properties of polymers are to some degree a function of the casting mass. Figure 4 shows an as-cast plate of the epoxy material along with the mold.

The polycarbonate material was purchased in precast sheet 1/8-in. thick from which the calibration specimens were machined. The polycarbonate material, as received, possesses considerable residual stresses in the plane of the sheet and a large stress distribution through the thickness. Therefore, it was necessary to stress relieve the polycarbonate material before testing. Stress relief was accomplished by heating slowly (5° F/hr) to 325° F and soaking at this temperature for approximately 12 hours and then cooling slowly (5° F/hr) to room temperature.

The specimen configuration is shown in Fig. 5. A 2-in. gage length was scribed on the specimen surface for gage-length measurement prior to and after the test. From these gage-length measurements the axial strain was determined. Gage-length measurements were performed utilizing the x-y micrometer stage mounted on the polariscope. This

*parts by weight

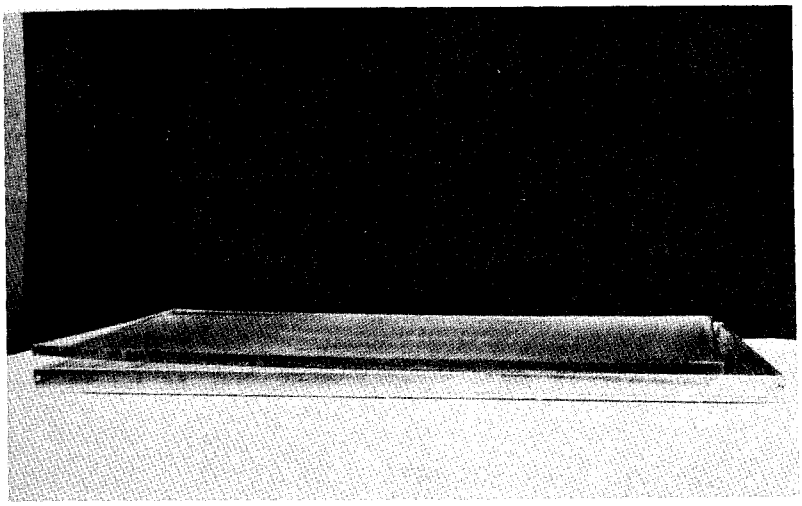

Fig. 4 As-Cast Epoxy Plate and Associated Mold

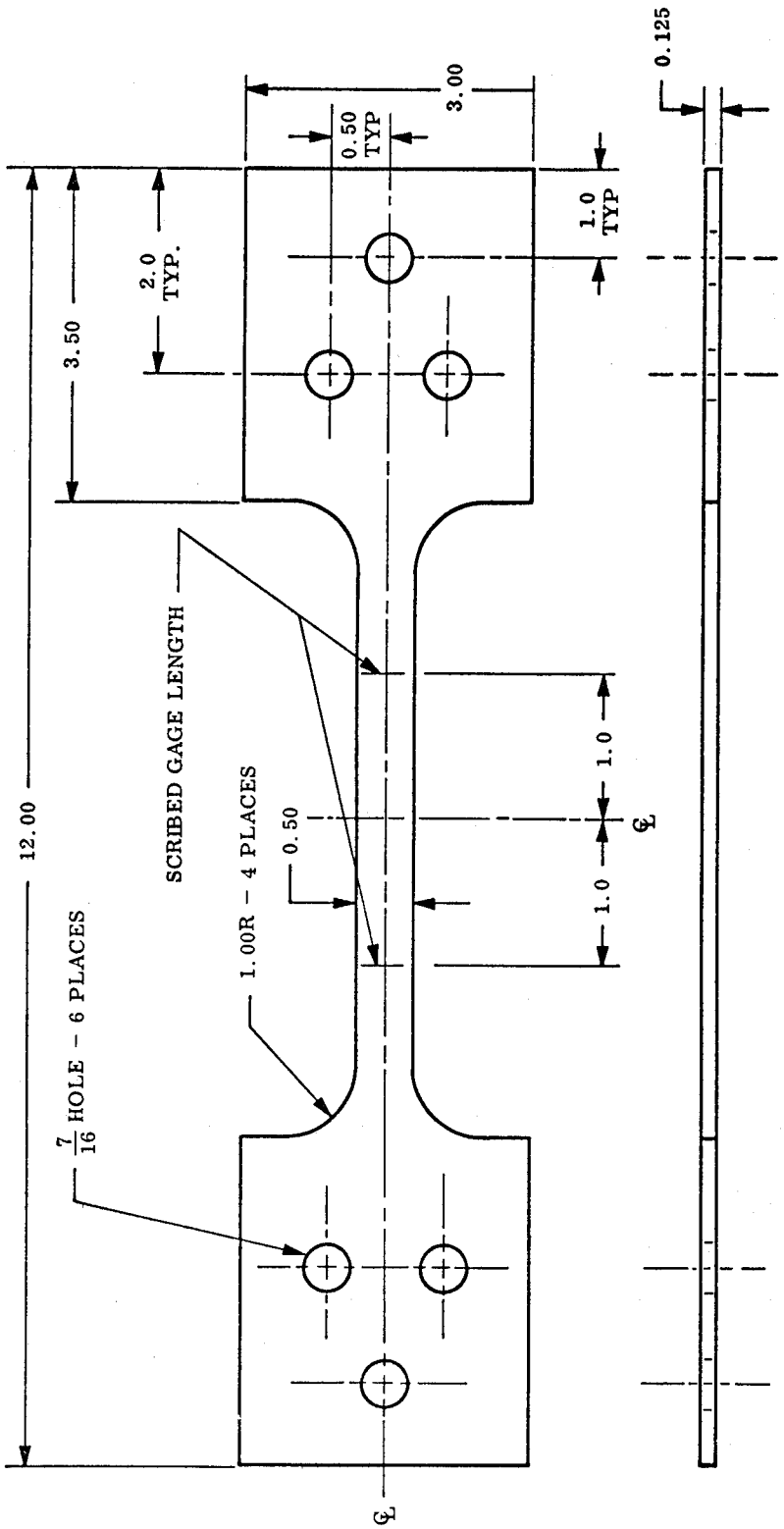

Fig. 5 Calibration Specimen Configuration

micrometer stage has a 0.0001-in. readout. The specimen was mounted on the micrometer stage surface and the scribeline viewed on the ground-glass screen of the polariscope by use of transmitted light. The cross-hair marking on the ground-glass screen was placed at one of the scribe marks. The micrometer stage was adjusted until the other scribeline appeared at the cross-hair. The distance of the adjustment designates the gage length. The axial strain was computed from the change in gage length (before and after test) divided by the original gage length ($e = \Delta\ell/\ell_o$). Figure 6 shows the appearance of the scribe line on the ground-glass screen of the polariscope. The scribe line image is projected on the ground-glass screen as 10× magnification. After the initial gage lengths (ℓ_o) have been recorded along with the initial thickness (t_o) and width (w_o), the specimens are then subjected to dead-weight loads. The specimens and test frame are placed in the stress-freezing oven, as shown in Fig. 7. The specimens were then subjected to a programmed thermal cycle consisting of the appropriate maximum temperature (T_{max}), a heating-and-cooling rate of approximately 5° F/hr, and a soak time at T_{max} of two hours except where otherwise noted.

After completion of the thermal cycle, the specimens are unloaded and removed from the stress-freezing oven. Then the final gage lengths ℓ_f are measured in the manner previously described, along with t_f and w_f. Also, birefringence measurements are taken after testing. Figure 8 represents typical frozen fringe order distribution and indicates uniform stress in the reduced section of the calibration specimen.

3.1.2 Experimental Results (Calibration Phase)

From the experimental data, effective stress-strain curves, nondimensionalized stress-strain curves and birefringence-strain curves were constructed. These curves are represented in Figs. 9 through 19.

For the epoxy plus diethanolamine material, there are two sets of curves presented, designated as batch A and batch B. The only difference between batch A and batch B is that the material was cast at different times from a different lot of the basic epoxy

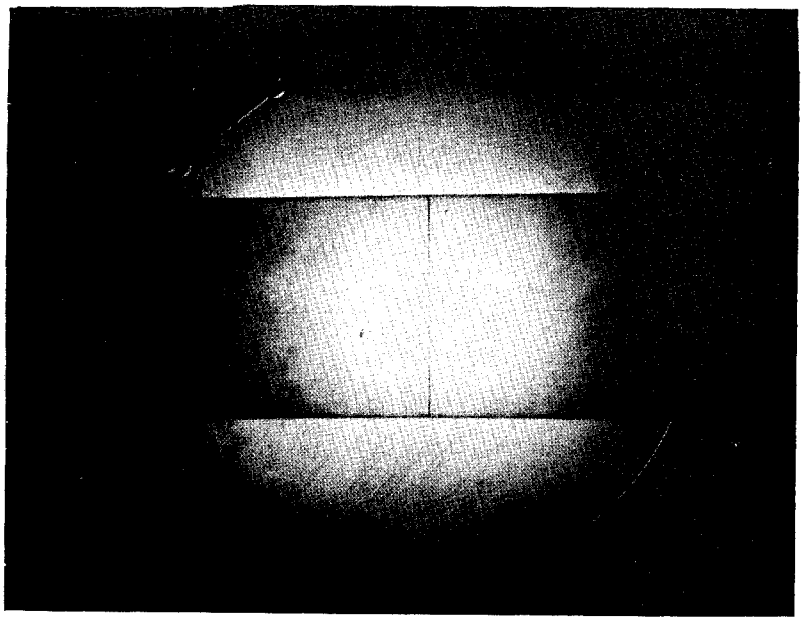

Fig. 6 Calibration Specimen Scribe Line as It Appears on Polariscope Projection Screen

Fig. 7 Loaded Calibration Specimens and Associated Test Frame in Furnace

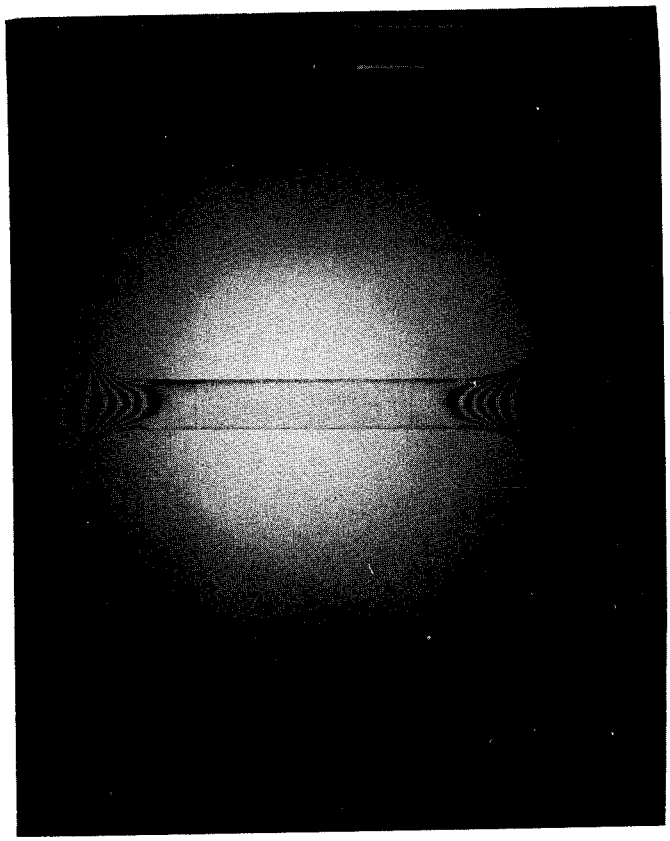

Fig. 8 Typical Frozen Stress Fringe Pattern for Calibration Specimen

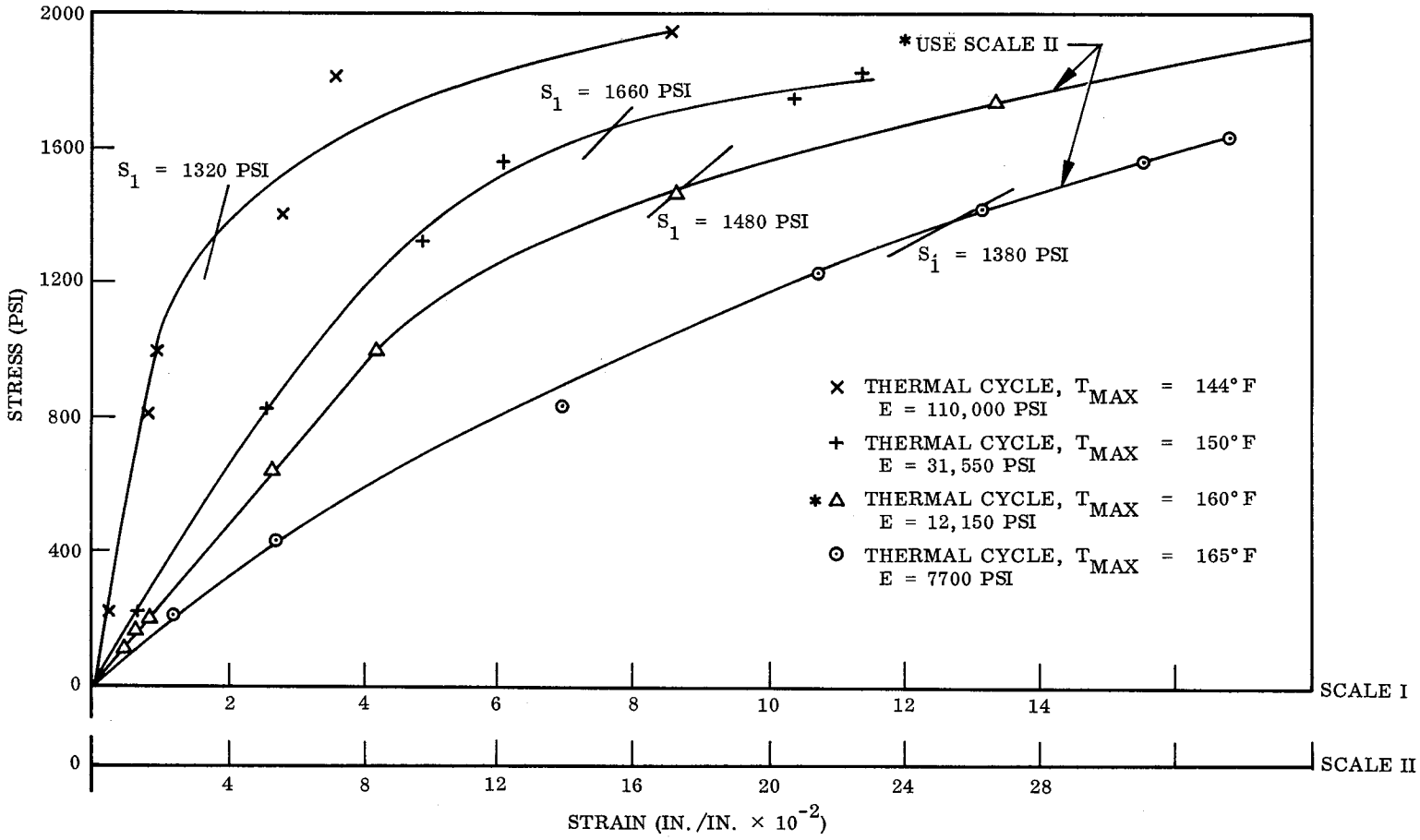

Fig. 9 Effective Stress-Strain Curves for Epoxy Material Batch B at Various Thermal Cycles

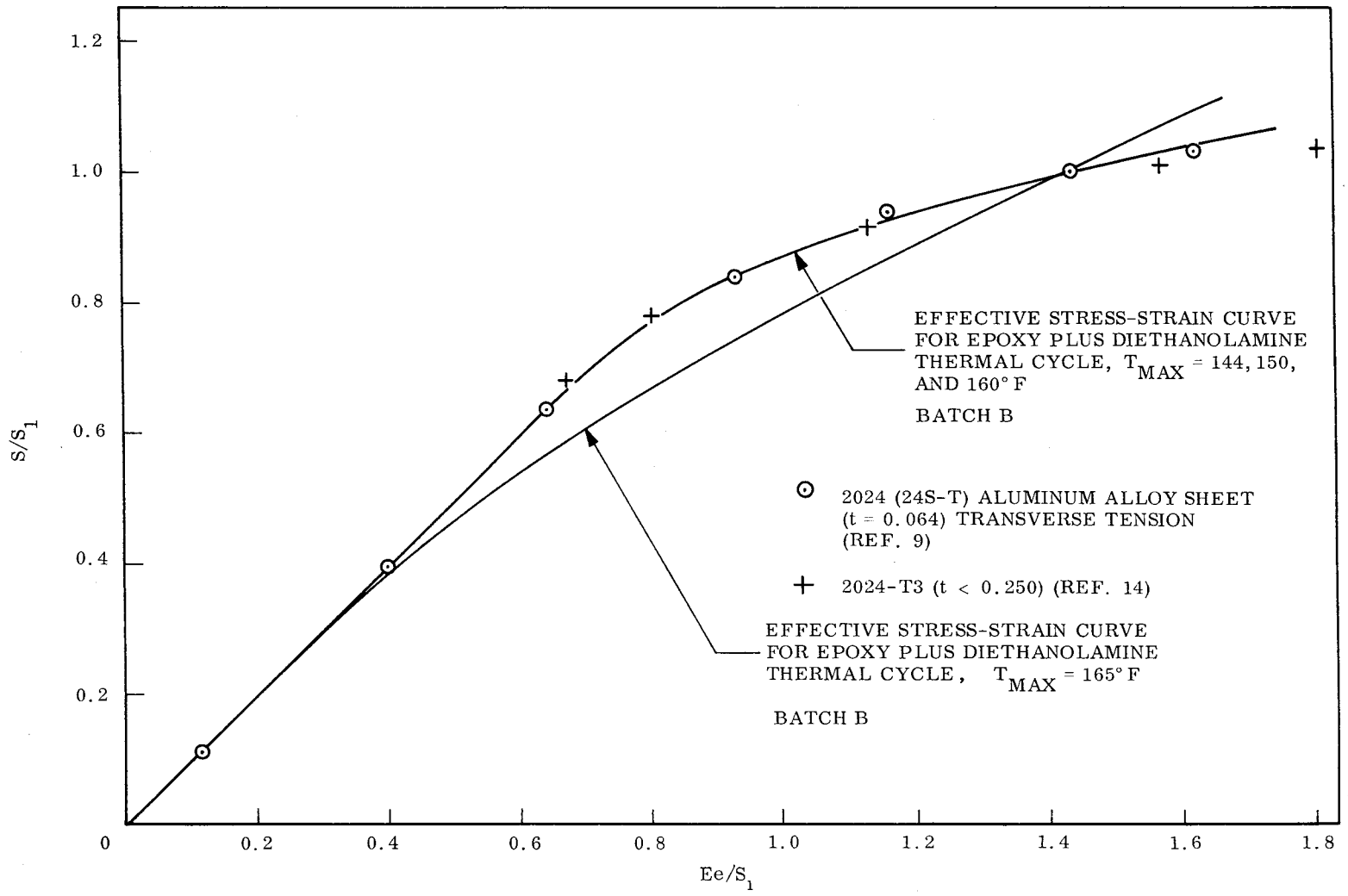

Fig. 10 Non-Dimensionalized Stress-Strain Curves for Epoxy Material Batch B

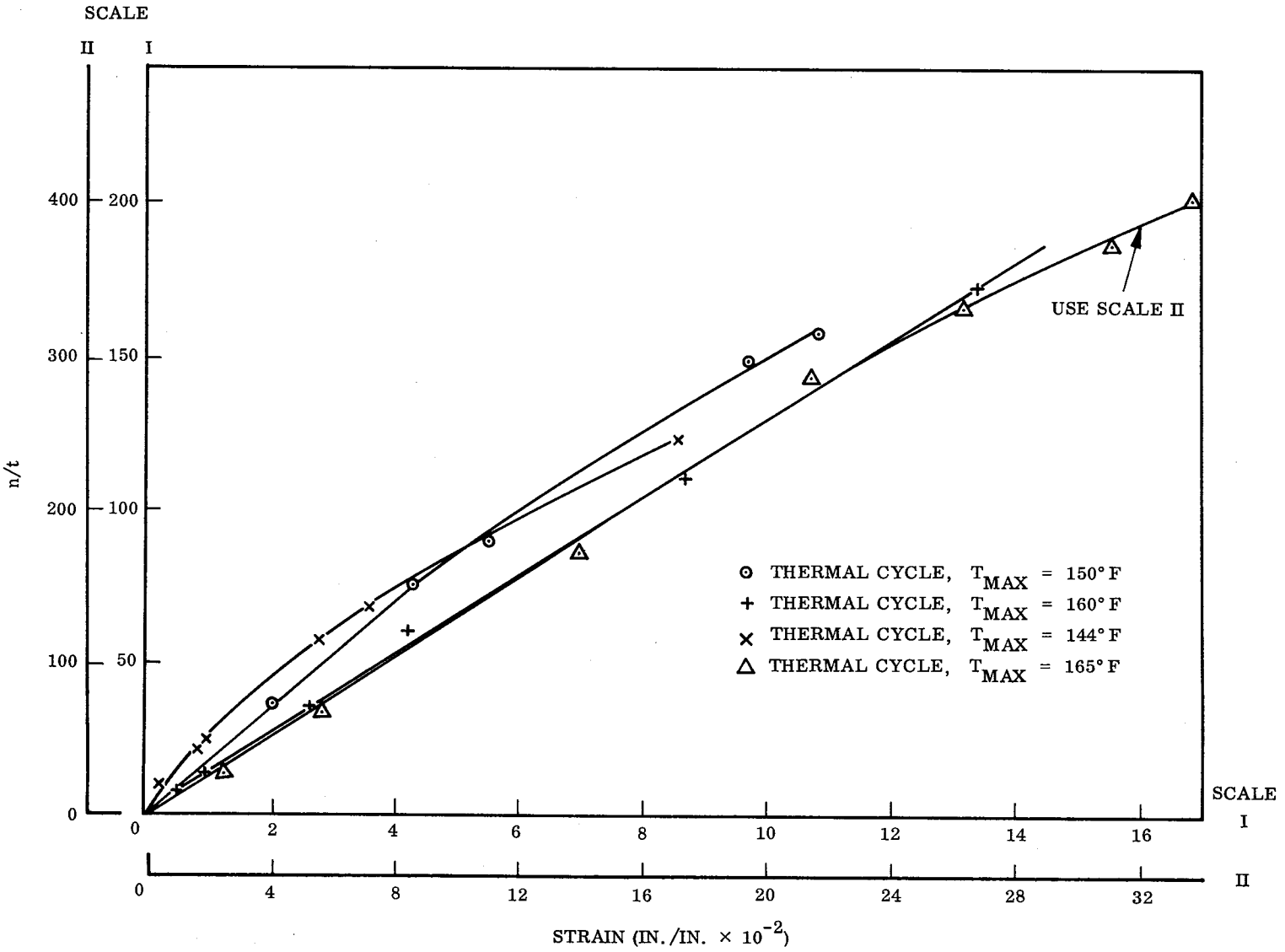

Fig. 11 Strain-Birefringence Curves for Epoxy Material Batch B at Various Thermal Cycles

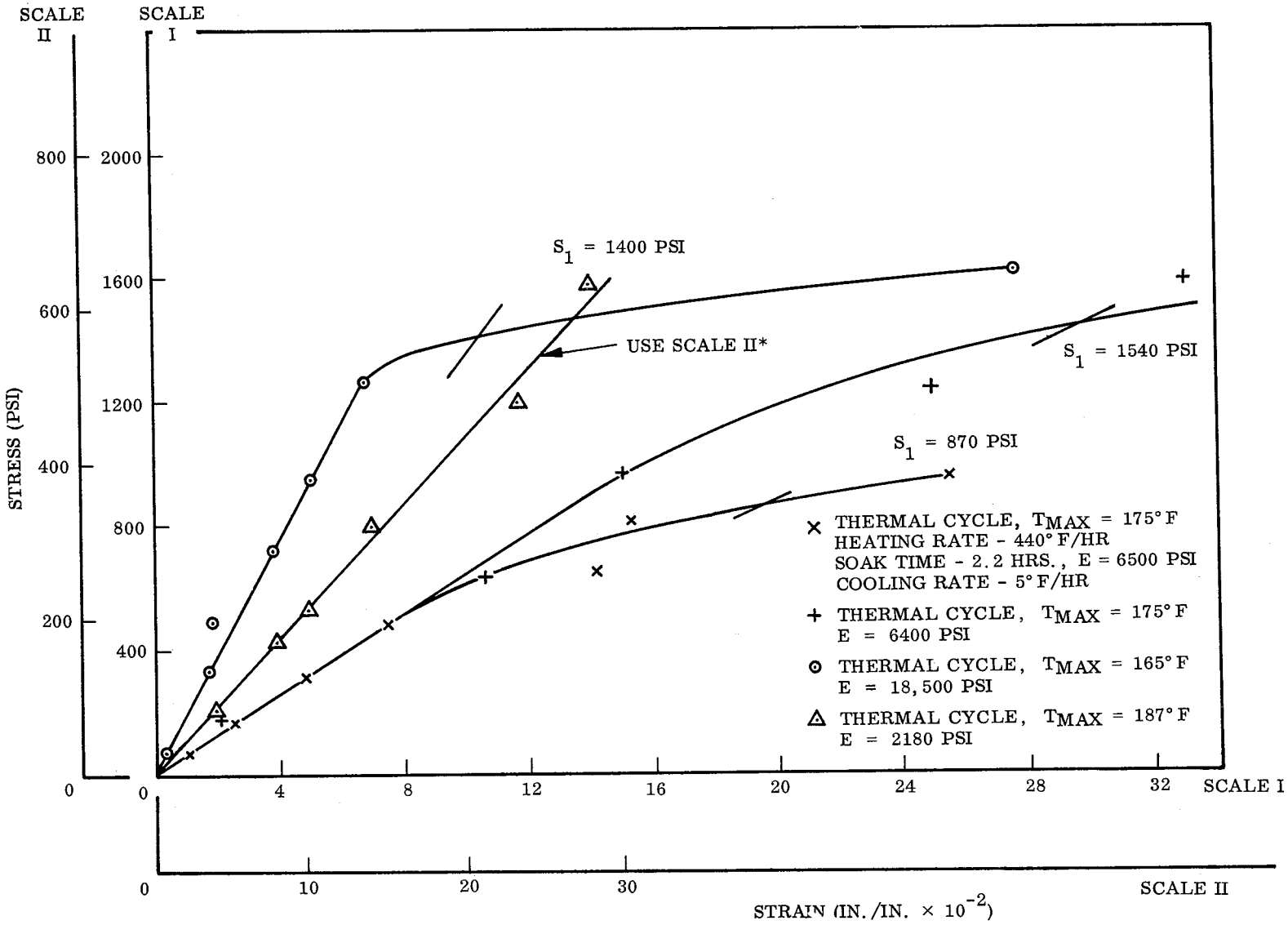

Fig. 12 Effective Stress-Strain Curves for Epoxy Material Batch A at Various Thermal Cycles.

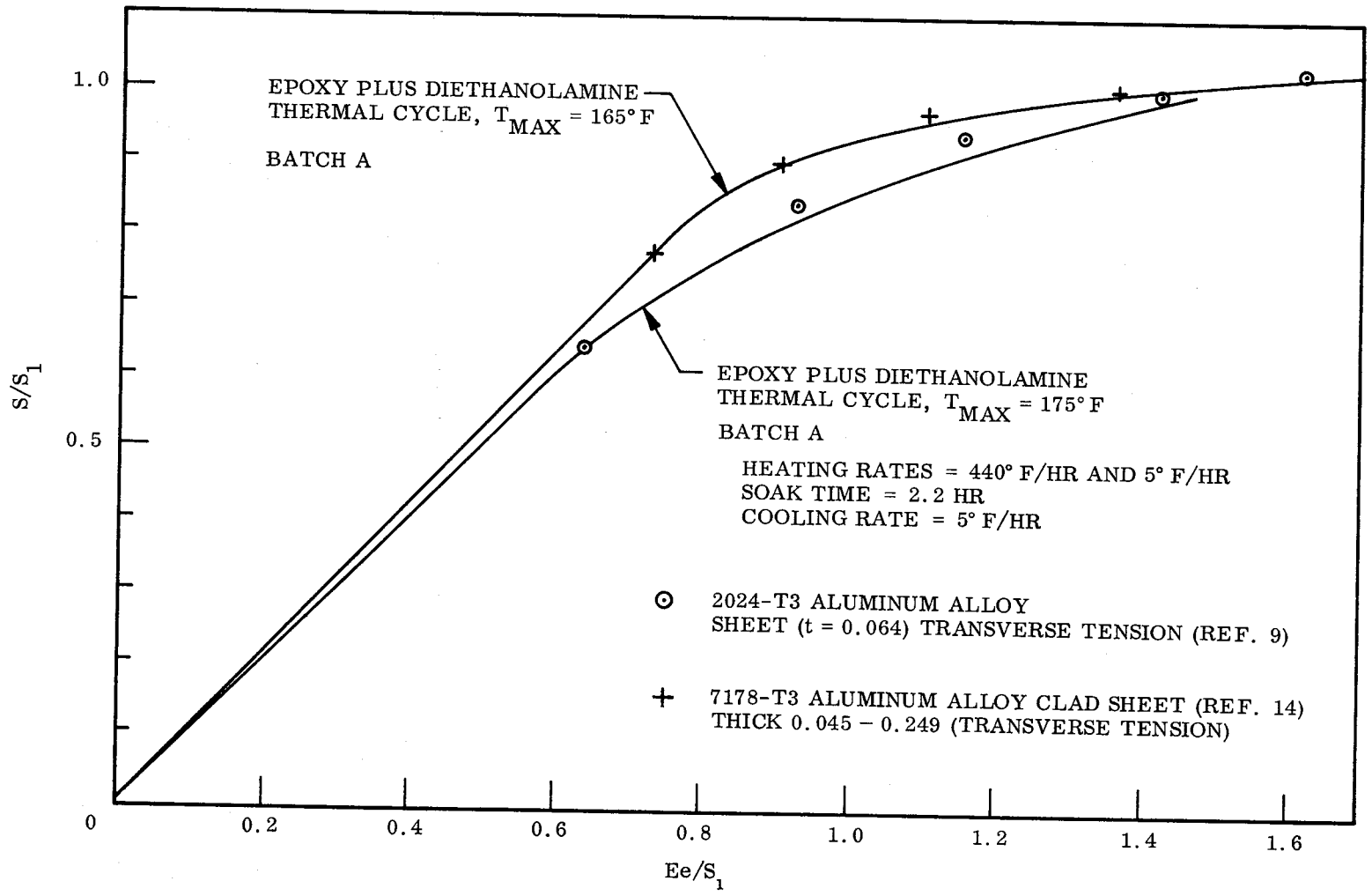

Fig. 13 Non-Dimensionalized Stress-Strain Curves for Epoxy Material Batch A at Various Thermal Cycles

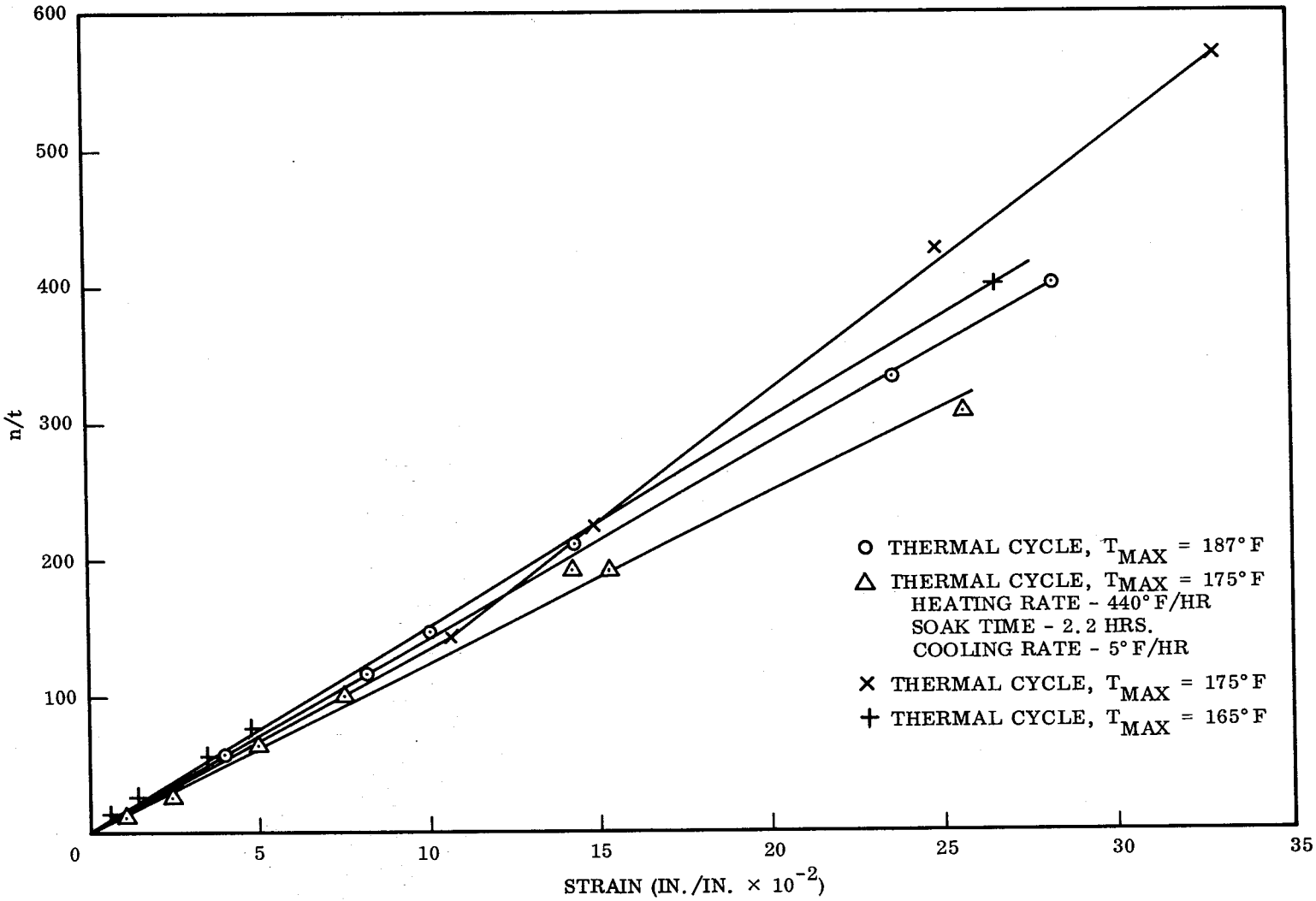

Fig. 14 Strain-Birefringence Curves for Epoxy Material Batch A at Various Thermal Cycles

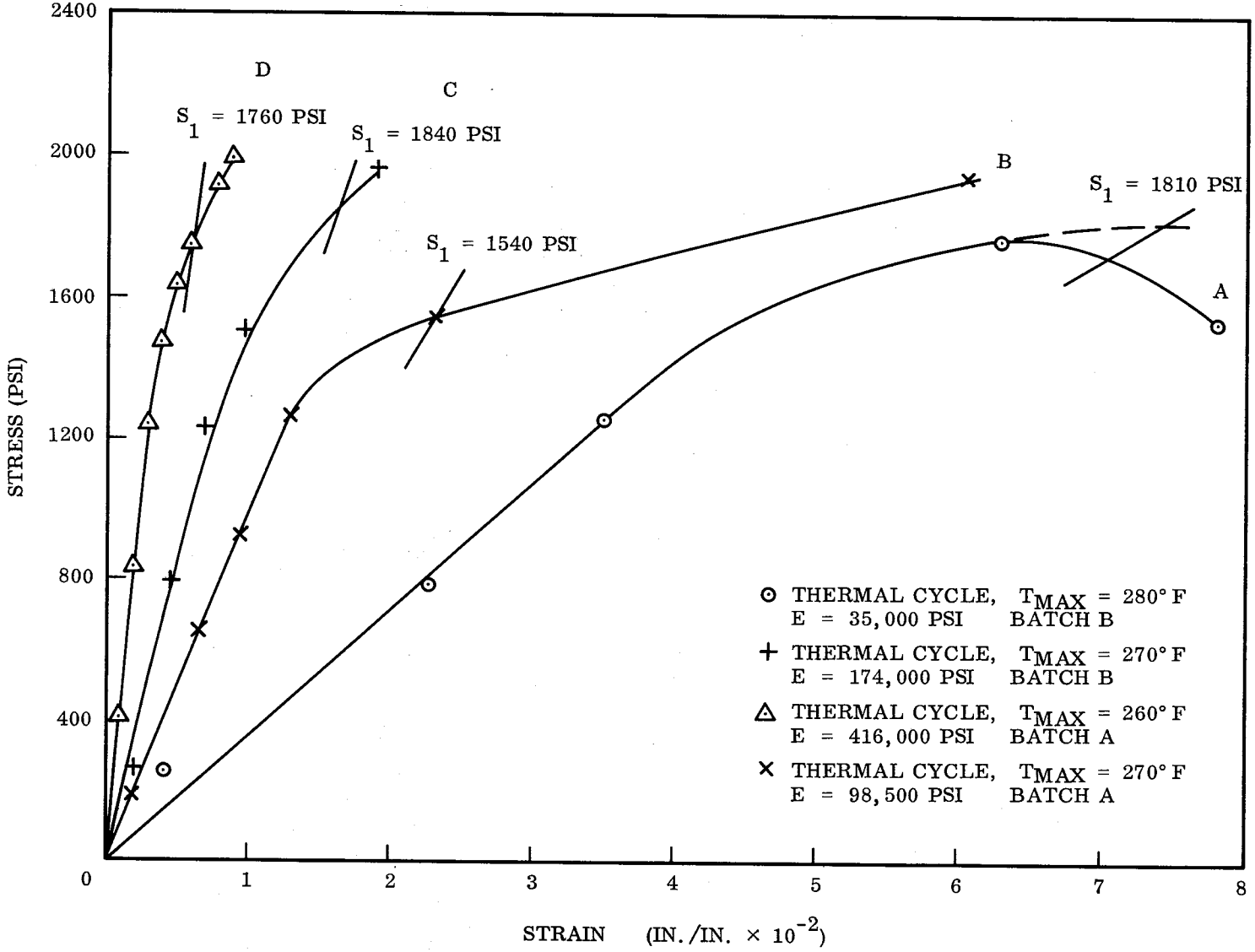

Fig. 15 Effective Stress-Strain Curves for Polycarbonate

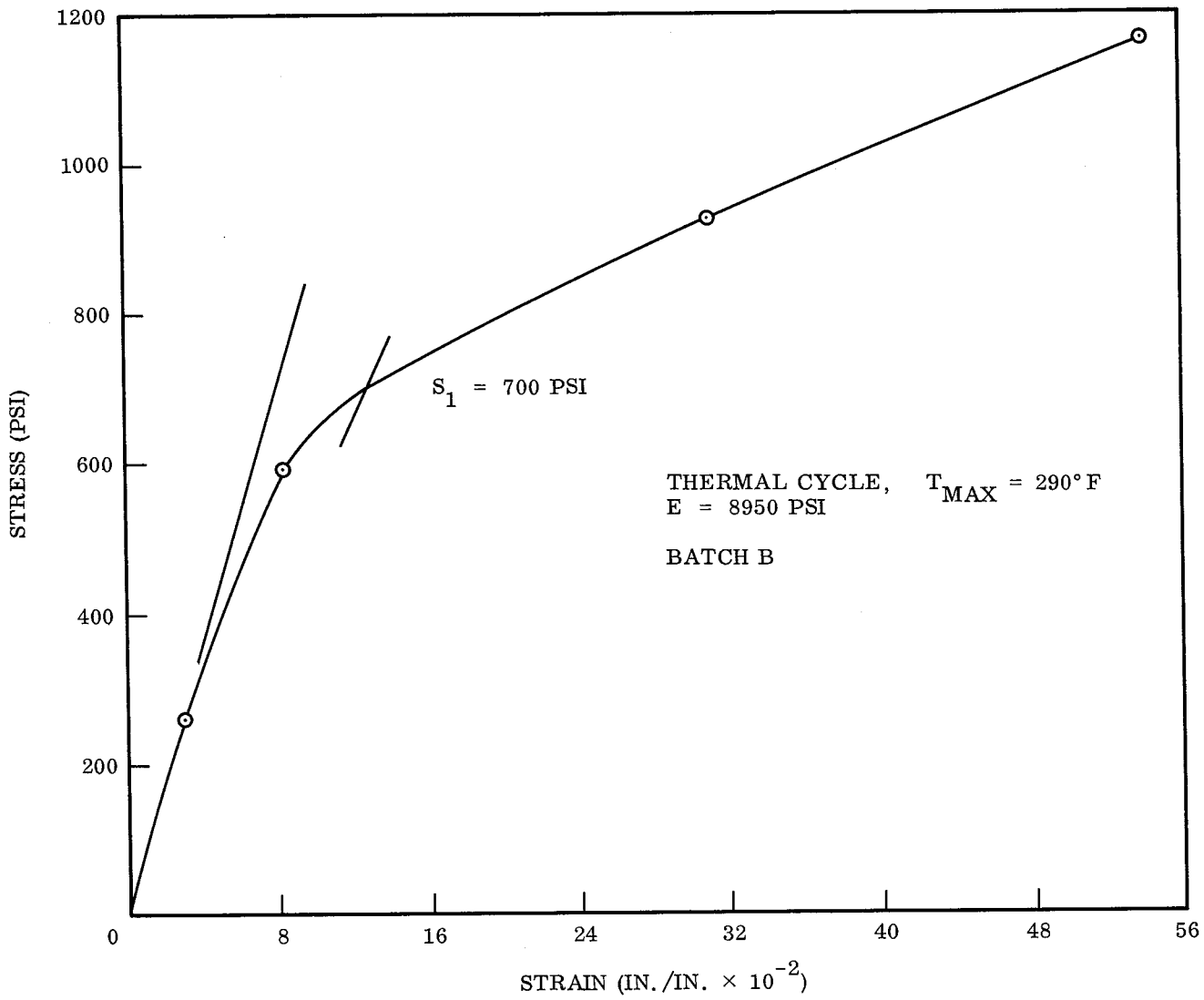

Fig. 16 Effective Stress-Strain Curve for Polycarbonate

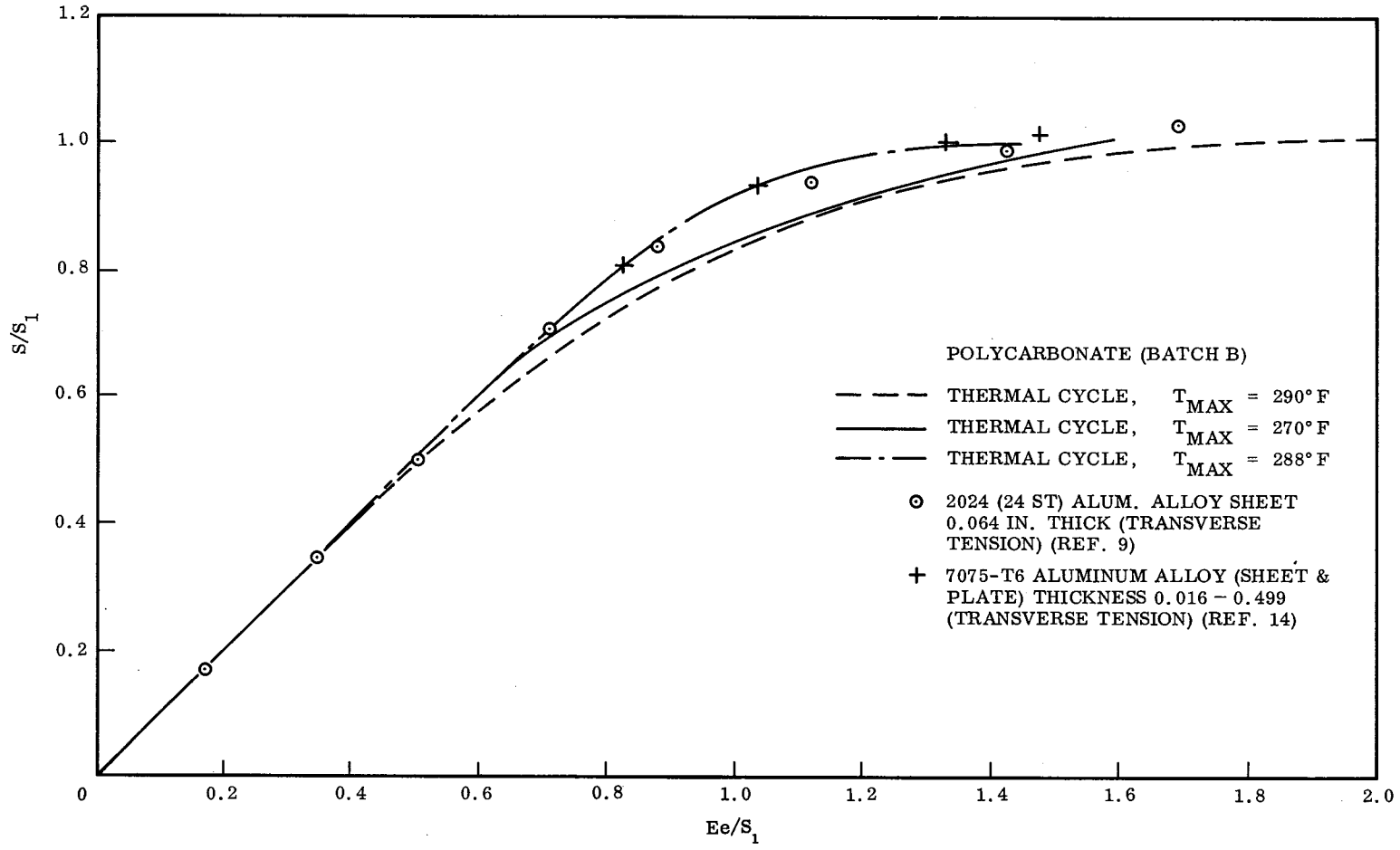

Fig. 17 Non-Dimensionalized Stress-Strain Curve for Polycarbonate Batch B at Various Thermal Cycles

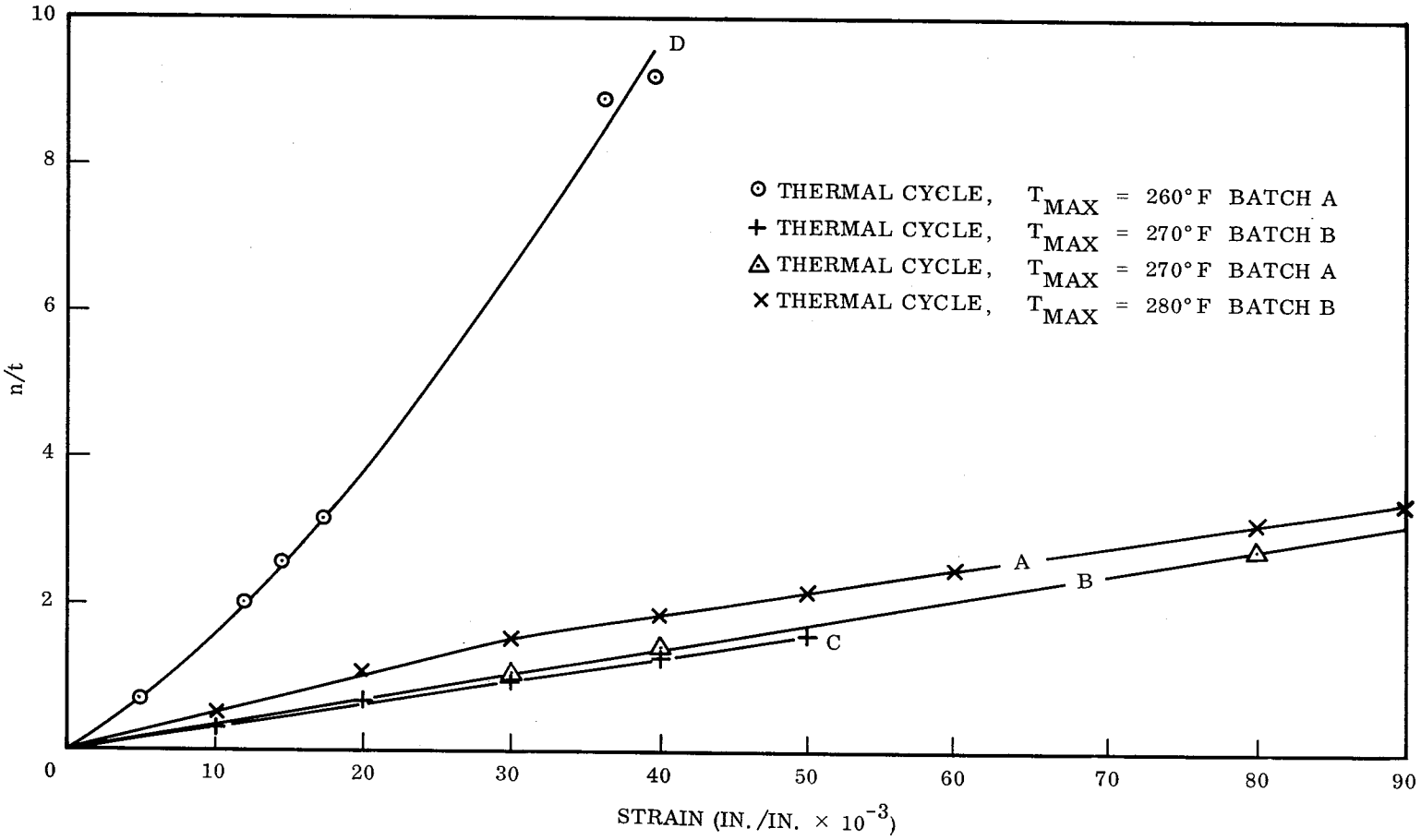

Fig. 18 Strain-Birefringence Curves for Polycarbonate Batch A and B at Various Thermal Cycles

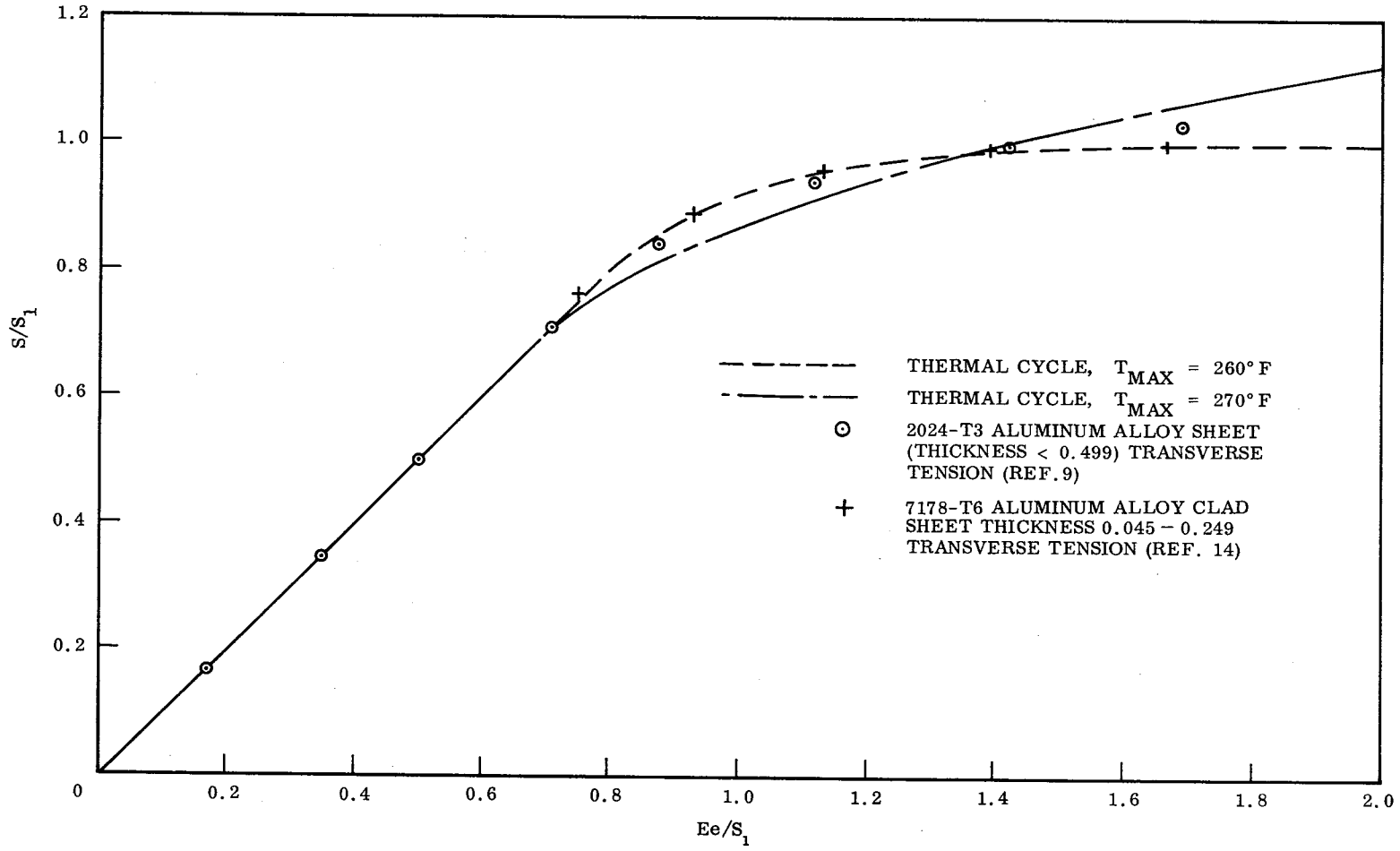

Fig. 19 Non-Dimensionalized Stress-Strain Curves for Polycarbonate Batch A at Various Thermal Cycles

resin. It should be noted that the experimental data differ significantly between the two batches. Sufficient material (batch B) was cast from the same lot of basic resin (and at the same time) for calibration of the epoxy material and for analysis of infinite plates with holes.

Also, two sets of curves are presented for the polycarbonate material designated as batch A and batch B. The polycarbonate calibration specimens were prepared from 1/8-in. sheet stock, which is commercially available in already cast form. Sheets designated as batch A and batch B were purchased at different times and exhibited significantly different properties. This difference indicates that control of material properties is not part of the manufacturing procedure. It is even possible that manufacturing techniques were different for the two batches of material.

3.1.2.1 Epoxy Material (Batch B)

Effective stress-strain and birefringence curves were generated for the epoxy material (batch B) for thermal cycles consisting of maximum temperatures of 144, 150, 160, and 165° F. The heating-and-cooling rates of these thermal cycles were approximately 5° F/hr and soak time was two hours.

The effective stress-strain data for batch B are represented in Fig. 9. The nondimensionalized stress-strain curves are shown in Fig. 10 along with the nondimensionalized stress-strain data for 2024(24S-T) aluminum alloy. The nondimensionalized stress-strain curves for thermal cycles with T_{max} = 144, 150, and 160° F are identical and compare favorably with the aluminum alloy 2024(24S-T). Figure 11 represents the strain-birefringence curves for the thermal cycles of T_{max} = 144, 150, 160, and 165° F. The birefringence is approximately linearly related to strain.

3.1.2.2 Epoxy Material (Batch A)

Effective stress-strain and birefringence curves were generated for the epoxy material designated as batch A for four thermal cycles. Three of these thermal cycles

consisted of maximum temperatures of 165, 175, and 187° F, heating-and-cooling rates of 5° F per hour, and soak times of two hours. The remaining thermal cycle consisted of a maximum temperature of 175° F, heating rate of 440° F per hour, soak time of two hours, and a cooling rate of 5° F per hour. The effective stress-strain curves for batch A are represented in Fig. 12. It should be noted that the two thermal cycles with T_{max} = 175° F yield significantly different effective stress-strain curves. Since the creep characteristics of the materials are utilized in generating the effective stress-strain curves it would be expected that the effective stress-strain curve for high heating rates would be represented by strain values lower than those for low heating rates for comparable stress levels, due to the longer time duration for the test. The difference between the stress-strain curves for low and high rates indicates that some post curing (hardening) takes place during the heating portion of the cycle due to the longer time at temperature during the heating portion of the thermal cycle for the stress-strain curve with low heating rate. Even though there is a significant difference between the effective stress-strain curves for T_{max} = 175° F, these curves yield the same non-dimensionalized stress-strain curve which is similar to 2024(24S-T) aluminum alloy. The nondimensionalized stress-strain curves for epoxy material, batch A are shown in Fig. 13.

For batch A, a thermal cycle consisting of a maximum temperature of 187° F yields an elastic stress-strain curve and standard frozen-stress properties. In other words, the maximum temperature is near enough to the critical temperature of the material so that creep causes unloading of the plastic phase and complete loading of the elastic phase (loading of the molecular chain) during the thermal cycle.

Figure 14 represents the strain birefringence curves for batch A material. Strain is approximately linearly related to birefringence.

3.1.2.3 Polycarbonate Material (Batch B)

Effective stress-strain and birefringence curves were generated for the polycarbonate material (batch B) for thermal cycles consisting of maximum temperatures of 270, 280, and 290° F. The heating-and-cooling rates of these cycles were approximately 5° F per hour and soak times were eight hours. . The effective stress-strain curves are represented in Fig. 15, curves A and C, and Fig. 16. These curves have been nondimensionalized in Fig. 17. The associated strain birefringence curves are shown in Fig. 18, curves A and C, except for T_{max} = 190° F. In this case it was not possible to measure birefringence due to the very high fringe order involved. On the basis of other data, fringe orders exceeding 150 were present in the 0.125-in. thick specimen for the lowest stress level (260 psi).

3.1.2.4 Polycarbonate Material (Batch A)

Two maximum temperatures (260 and 270° F) were used to generate the effective stress-strain curves for batch A. The same heating-and-cooling rates and soak times were used as for batch B. The effective stress-strain curves are shown in Fig. 15, curves B and D. The stress-strain curves have been nondimensionalized and compared with 2024(24ST) aluminum alloy in Fig. 19. The strain-birefringence data are shown in Fig. 18, curves B and D.

3.2 PHOTOELASTO-PLASTIC ANALYSIS OF INFINITE PLATES

3.2.1 Test Procedure

Based upon the results of the calibration phase, a material and thermal cycle was selected which would exhibit an effective stress-strain curve similar to an aluminum alloy. The material selected for use in the infinite plate study was an epoxy resin cured with 10 pbw* of diethanolamine curing agent, batch B. The infinite plate models

*Parts by weight

were subjected to a thermal cycle consisting of a maximum temperature of 160° F, heating and cooling rates of 5° F per hour and soak time at maximum temperature of two hours while under a constant load. Four infinite plate models of the configuration shown in Fig. 20 were machined from the selected material and batch number. These plates were 4 in. wide and contained a 1/8-in. diameter centrally located hole. Two models each were machined to a thickness of 0.125 in. and 0.400 in. Each plate was subjected to constant tensile load throughout the thermal cycle. The load was applied and controlled by means of a hydraulic ram, hydraulic power supply, and servo control system. The furnace, test frame, hydraulic ram, and associated instrumentation are shown in Fig. 21.

In Fig. 22, the birefringence n/t has been replotted in terms of shear stress (τ) from the curves of strain vs. birefringence and stress vs. strain for epoxy material, batch B, and thermal cycle T_{max} = 160° F. Stresses were determined from birefringence measurements utilizing the curve in Fig. 22.

3.2.2 Experimental Results (Verification Phase)

3.2.2.1 Thin-Plate Models

The thin-plate models had a thickness-to-hole-diameter ratio of 1.0. It was assumed that the condition of plane stress was approximately satisfied. Therefore, only the stress distributions along the y axis were determined. The two thin-plate models were subjected to tensile loading which would produce two different levels of plasticity, namely

$$\sigma_\infty/\sigma_1 = 0.11 \text{ (elastic)} \quad \text{and} \quad \sigma_\infty/\sigma_1 = 0.71$$

The coordinate axes are identified for the thin-plate models in Fig. 23. The thin-plate models were optically viewed with polarized light incident normal to the x-y plane. Observation in this direction provides information concerning the principal

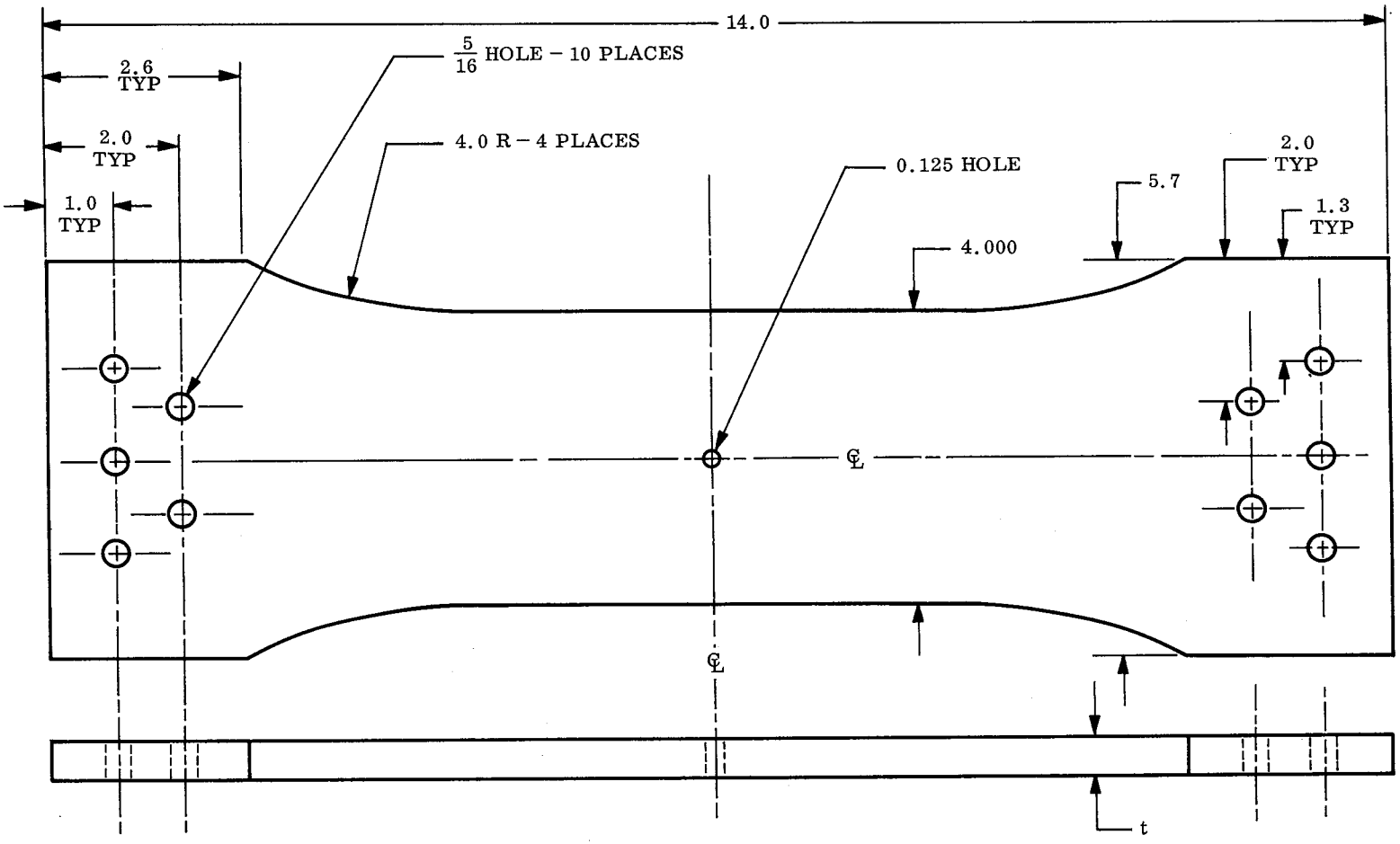

Fig. 20 Infinite Plate Model Configuration

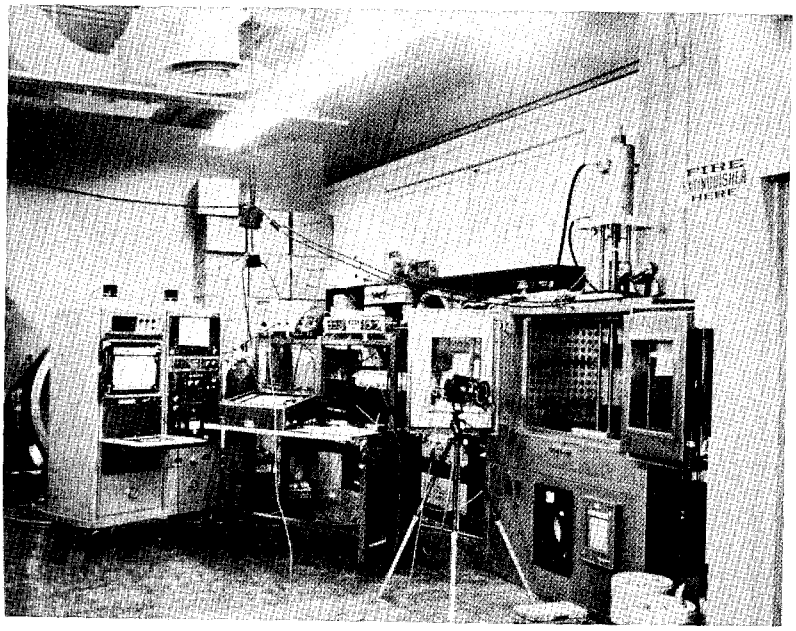

Fig. 21 Hydraulic Ram, Servo Control, Test Frame, Furnace, and Associated Instrumentation for Infinite Plate Study

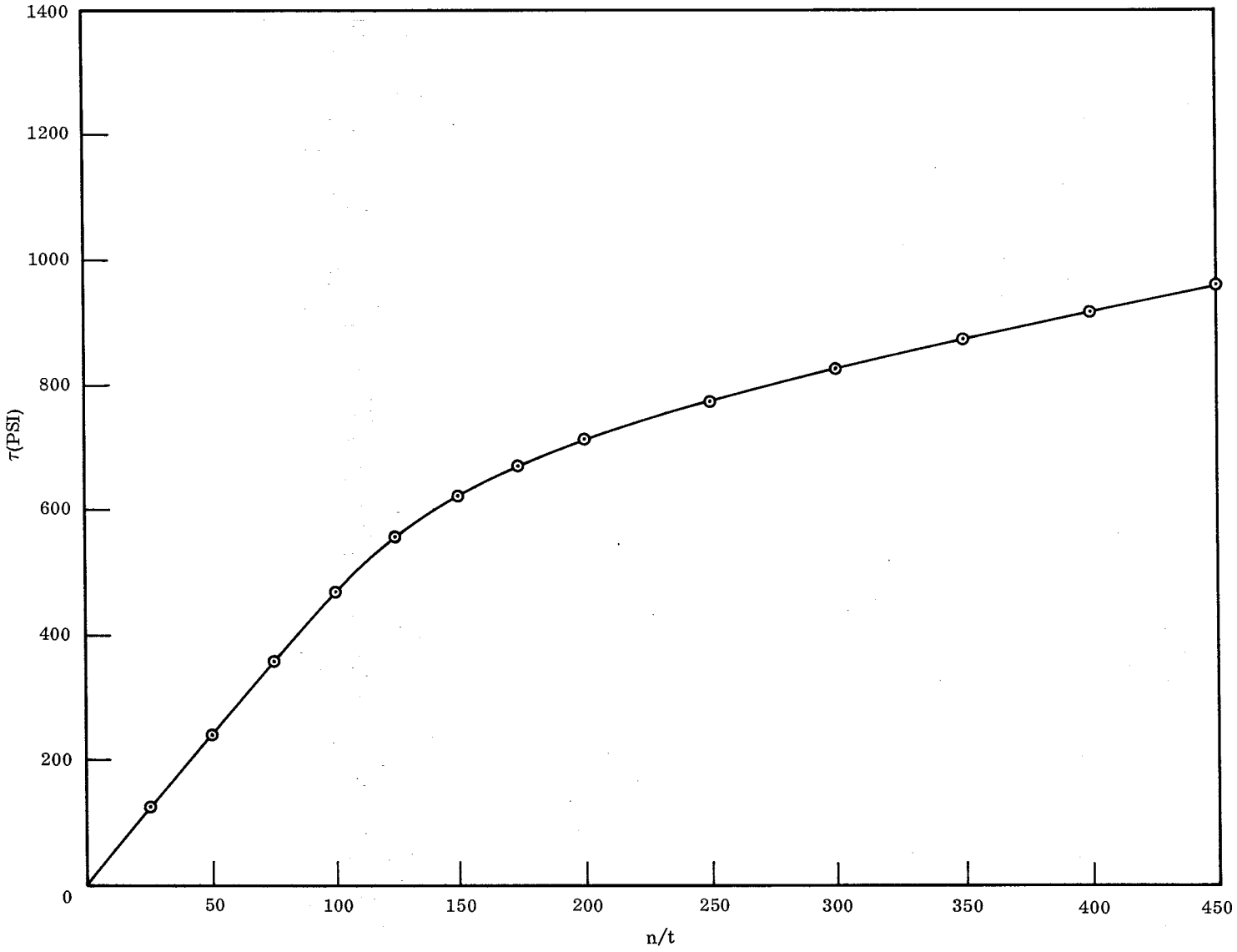

Fig. 22 Stress-Birefringence Curve at Thermal Cycle $T_{max} = 160° F$

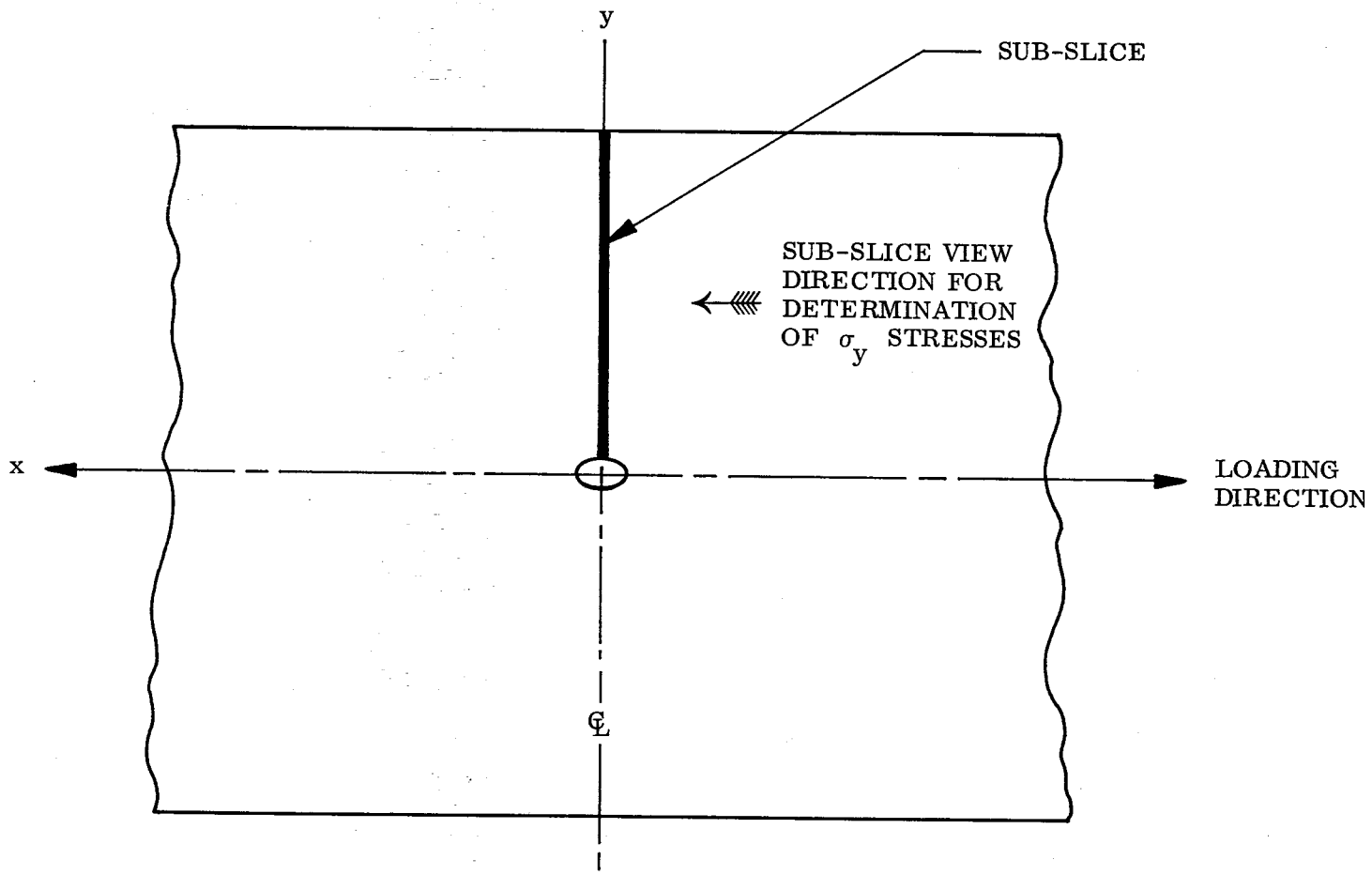

Fig. 23 Co-ordinate Orientation, Slice Location, and Viewing Direction for Plane Stress Models

stress difference in the x-y plane. Fringe order measurements were made along the y axis in the vicinity of the hole using the Tardy compensation technique. It was necessary to reduce the thickness to approximately 0.027 in order to determine a reference fringe. Fringe order measurements along the y axis provide the distribution of the $(\sigma_x - \sigma_y)$ stresses. At the free boundary, $(\sigma_x)_{max}$ could be measured directly. A sub-slice was cut from the specimen, as shown in Fig. 23. Fringe order measurements taken for this sub-slice, when viewed in the x direction, provided the distribution of the σ_y stresses along the y axis. From the distribution of the $(\sigma_x - \sigma_y)$ stresses and the σ_y stresses, the σ_x stress distributions were determined for the two thin plates. The stress distributions for the thin-plate models are shown in Figs. 24 and 25. The stress distributions are plotted in terms of the ratio of the stress at the point σ to the stress in the net section σ_∞ which was determined from P/A.

The infinite plate of $2r_o/h = 1.00$ and load condition of $\sigma_\infty/\sigma_1 = 0.11$ represents an elastic stress distribution. Referring to the effective stress-strain curve shown in Fig. 22, the maximum stress is approximately 160 psi. This is well below the elastic limit.

The dashed curves in Fig. 24 represent the theoretical stress distributions assuming a plane stress condition. The maximum stress concentration factor α_k measured experimentally is 3.3 which is approximately 10 percent higher than the theoretical value for the plane stress condition. The experimental stress distribution represented in Fig. 24 is actually representative of the midplane stresses. Therefore, the high stress-concentration factor tends to indicate the condition of plane stress is violated for a plate with a $2r_o/h$ ratio of 1.00.

According to an analysis of infinite plates with centrally located holes by J. B. Alblas (Ref. 10), a stress concentration factor of 3.1 is indicated for the condition of $2r_o/h = 1.0$ at the midplane.

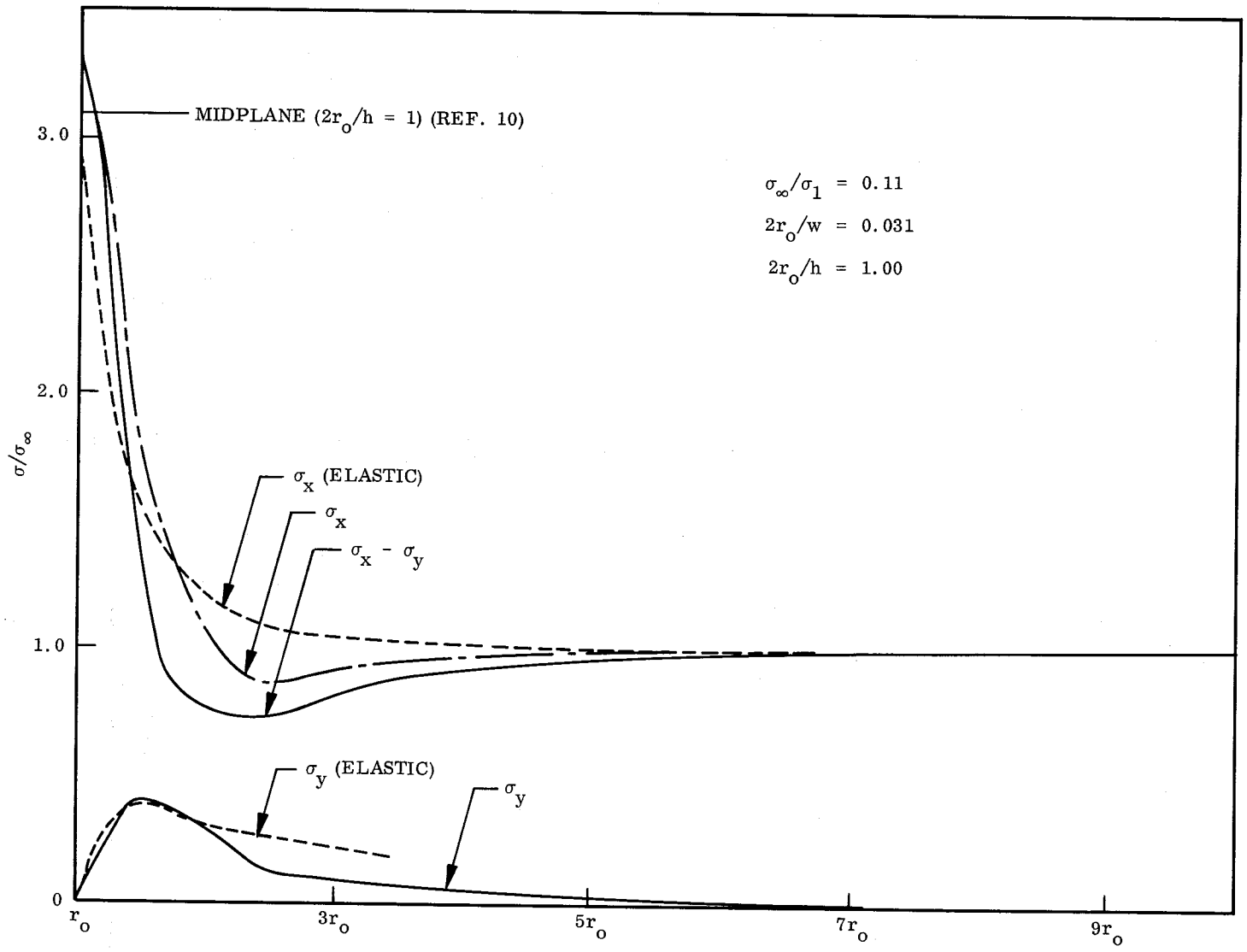

Fig. 24 Elastic-Stress Distribution for Thin Infinite Plate With Centrally Located Hole σ_∞/σ_1

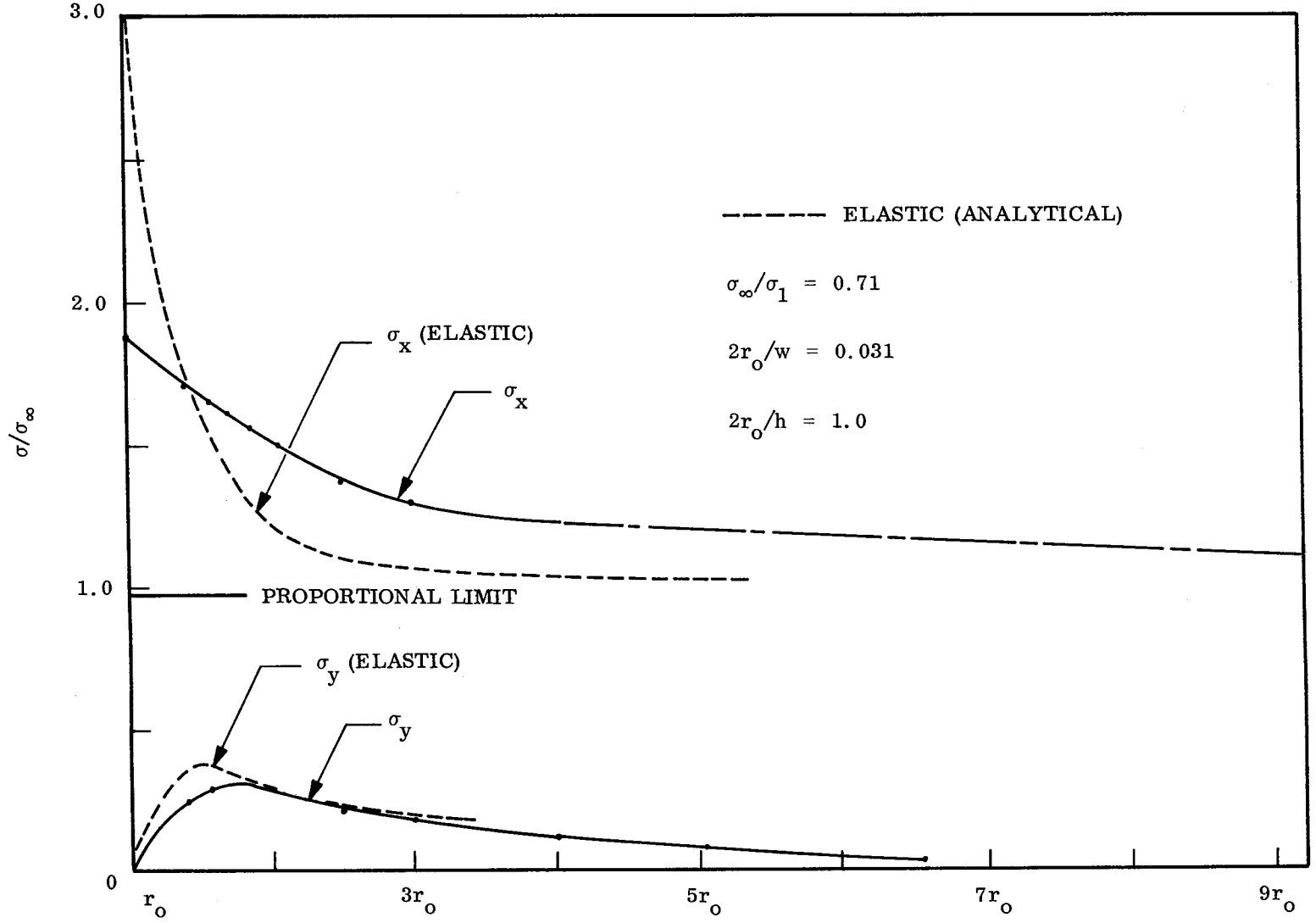

Fig. 25 Elasto-Plastic Stress Distribution for Thin Infinite Plate With Centrally Located Hole $\sigma_\infty/\sigma_1 = 0.71$

For the infinite plate ($2r_o/h = 1.0$) and load condition $\sigma/\sigma_\infty = 0.71$, considerable plastic flow occurs. The stress disturibution for the midplane of this model is shown in Fig. 25. Here again the dashed curves represent the analytical solution for the plane stress elastic condition.

3.2.2.2 Thick-Plate Models

The thick-plate models had a hole-diameter-to-thickness ratio of 0.33. The two thick-plate models were subjected to tensile loading which would produce two different levels of plasticity, $\sigma_\infty/\sigma_1 = 0.41$ and 0.53.

The slicing scheme used for the thick-plate models is shown in Fig. 26. The diagram in (a) shows the location and orientation of the surface slice (slice thickness of 0.012 in.) and midplane slice (slice thickness of 0.025 in.). Observation of these slices in the z direction provided information concerning the distribution of $(\sigma_x - \sigma_y)$ stresses as a function of y at $z = 0$ and $z = h/2$.

Assuming symmetry of stresses at opposite sides of the hole, a slice was prepared for determination of the σ_z stresses. The slice location and orientation for determination of σ_z stresses is shown in (b) of Fig. 26. The slice was observed in the x direction. Optical measurements, performed on this slice for $z = h/2$ as a function y, provided for the distribution of the σ_y stresses as a function y. The σ_x stress does not produce an optical effect for the slice because observation is in the x direction.

Optical measurements, for the slice in (b) of Fig. 26, taken for $z = 0$ along the y axis, provide the distribution of the σ_z stresses as a function of y at $z = 0$ where the σ_z stresses are maximum, assuming σ_y constant through the thickness.

The stress distribution for the thick infinite plate ($2r_o/h = 0.31$), loaded to $\sigma_\infty/\sigma_1 = 0.41$, is shown in Fig. 27. The dashed curves represent the analytically determined stress distribution for the elastic plane stress condition. Also shown is the distribution of the σ_z stresses at the midplane where they are a maximum.

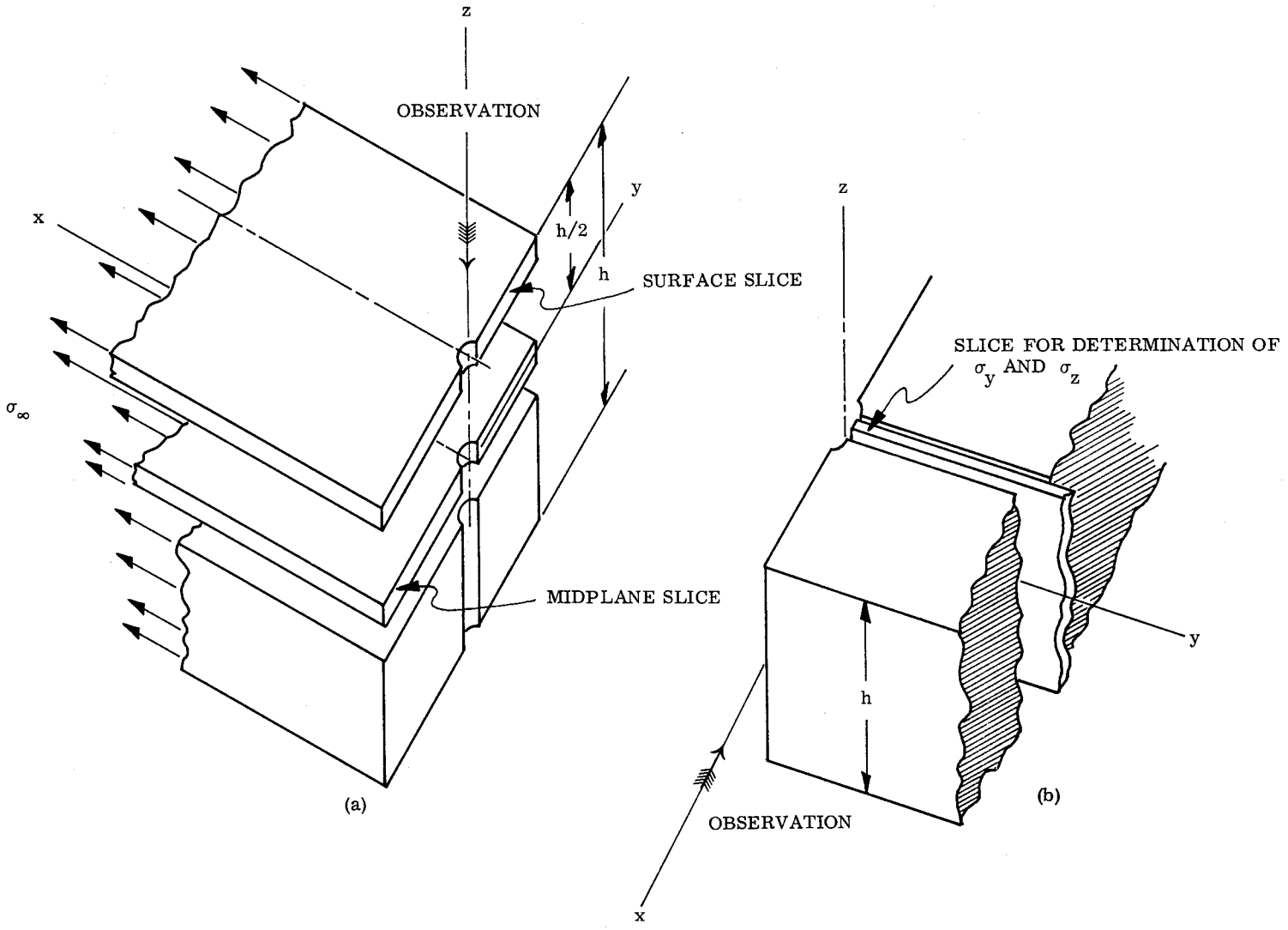

Fig. 26 Co-ordinate Orientation, Slice Location, and Viewing Direction for Elasto-Plastic Models

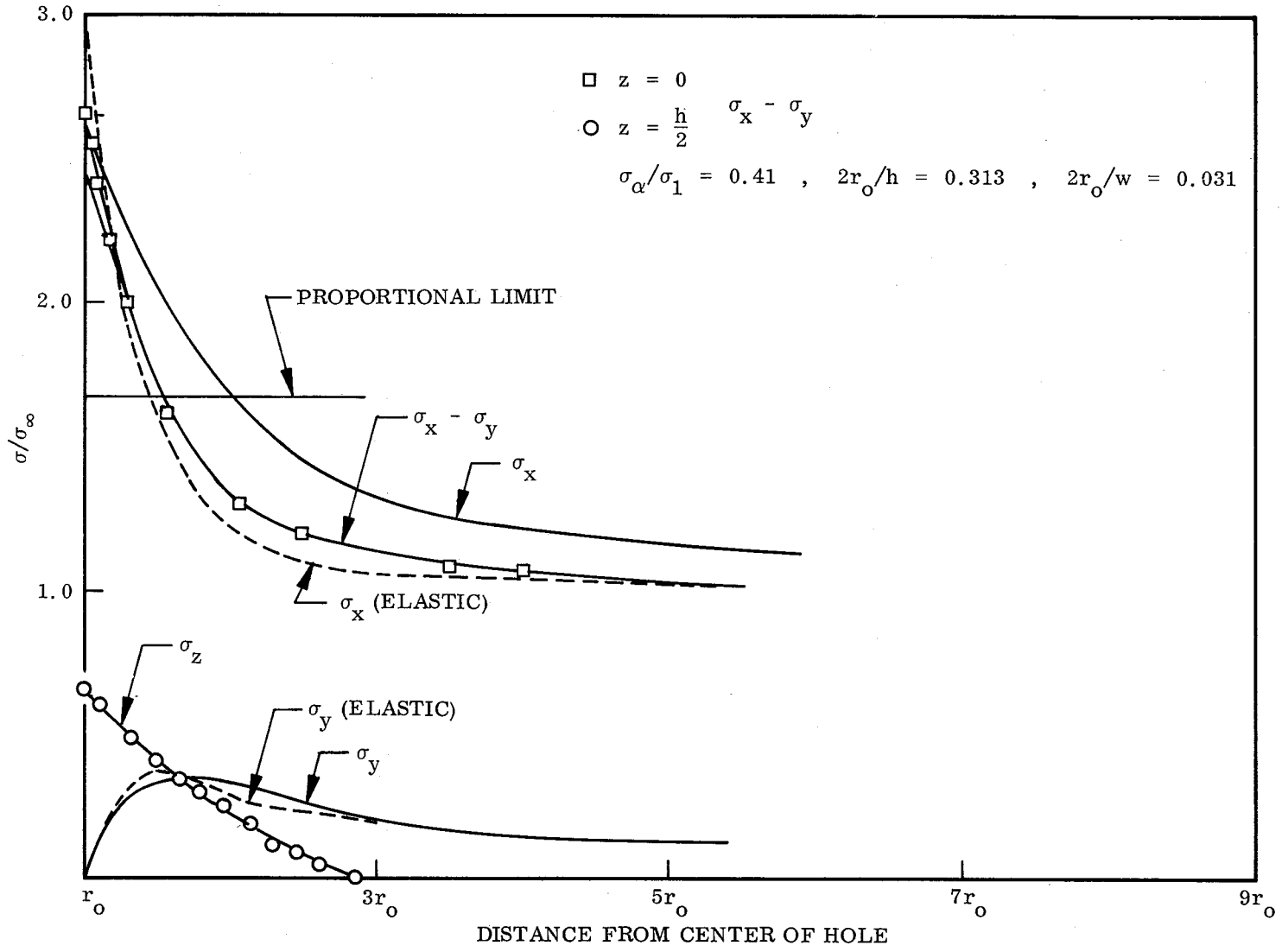

Fig. 27 Elasto-Plastic Stress Distribution for Thick Infinite Plate With Centrally Located Hole $\sigma_\infty/\sigma_1 = 0.41$

The stress distribution for the thick infinite plate $(2r_o/h = 0.31)$ loaded to $\sigma_\infty/\sigma_1 = 0.53$ is shown in Fig. 28. Here, again, the dashed curves represent the analytically determined elastic plane stress condition. Figure 29 shows a typical frozen fringe order pattern for slices removed from the thick plate models used for determination of $\sigma_x - \sigma_y$ stresses.

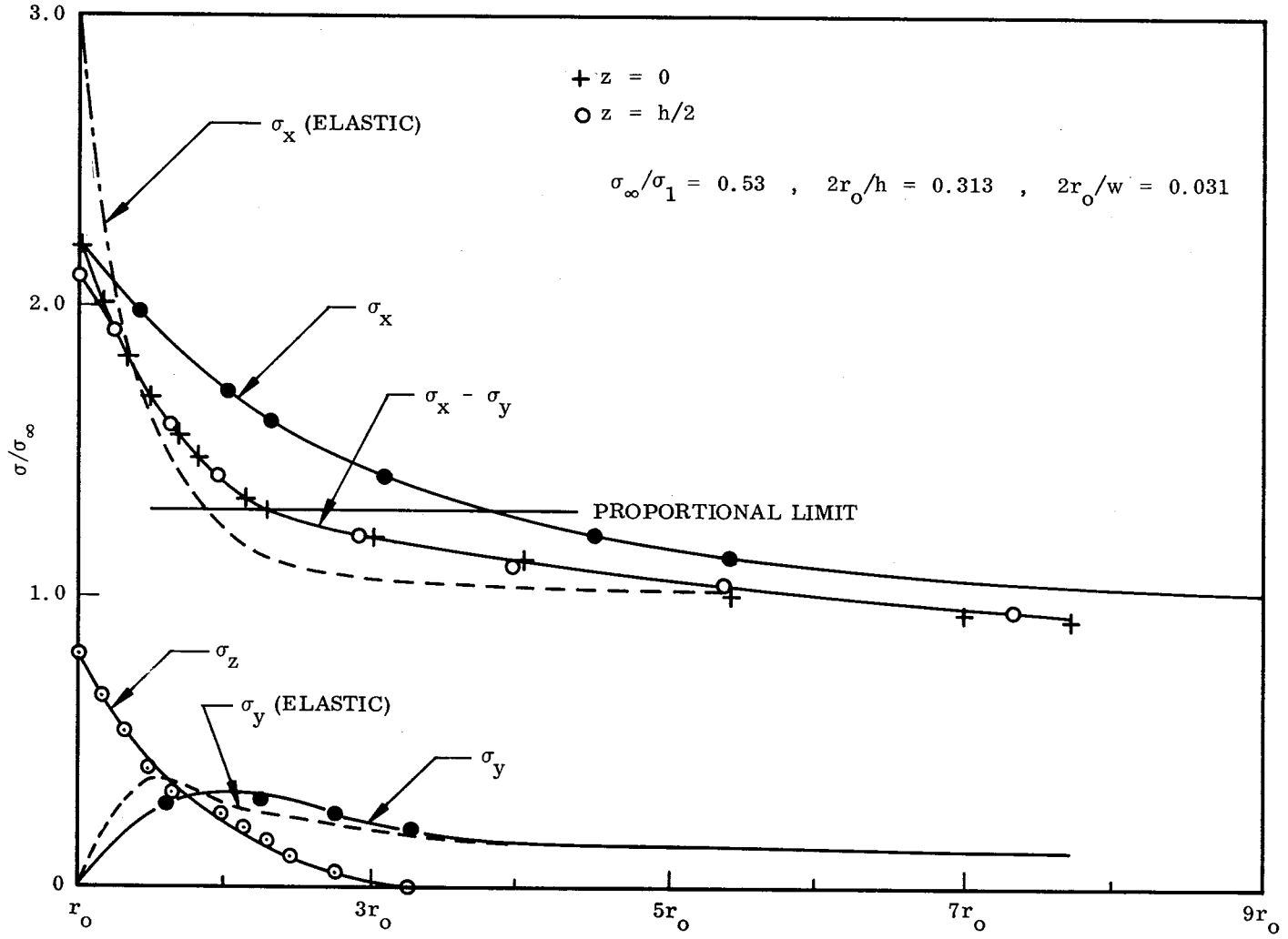

Fig. 28 Elasto-Plastic Stress Distribution for Thick Infinite Plate With Centrally Located Hole $\sigma_\infty/\sigma_1 = 0.53$

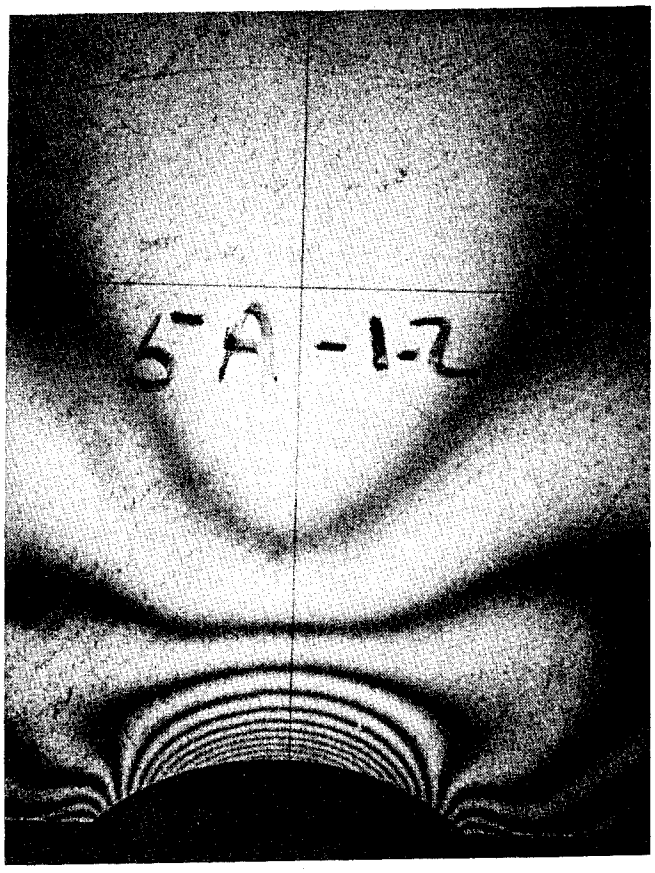

Fig. 29 Typical Photoelasto-Plastic Fringe Pattern for Midplane Slice in Thick Infinite Plate in Vicinity of Hole

Section 4

DISCUSSION OF RESULTS

4.1 DEVELOPMENT AND VERIFICATION

4.1.1 Calibration Phase (Development Phase)

The effective stress-strain curves generated during the course of this program were nondimensionalized by plotting stress S/S_1 versus strain Ee/S_1, where S_1 represents the secant yield strength for 0.7E. These curves were compared with nondimensionalized stress-strain curves for several aluminum alloys plotted in terms of the same parameters. If similarity exists between the effective stress-strain curve for the photoelasto-plastic material and an aluminum alloy, they will yield the same nondimensional stress-strain curves.

It was found that the epoxy material (batch B) yields an effective stress-strain curve similar to 2024-T3 aluminum alloy (transverse tension) when subjected to a thermal cycle consisting of a heating-and-cooling rate of 5° F per hr and any maximum temperature from 144° F through 160° F. The epoxy material (batch A) yielded an effective stress-strain curve which simulates the uniaxial stress-strain behavior of 7178-T6 aluminum alloy alclad sheet in transverse tension for a thermal cycle of heating-and-cooling rate of 5° F per hr and a maximum temperature of 165° F.

The similarities mentioned above consider cases where the nondimensionalized stress-strain curves are almost identical. However, the epoxy resin could be used to approximate almost any of the aluminum alloys for which the stress-strain curve has a gradual change in slope in the nonlinear range to determine empirical data concerning the elasto-plastic stress distributions resulting from flow.

Also, the epoxy material possesses very good machinability, making it possible to prepare the very thin slices (to 0.005 in.) required for three-dimensional analysis in the vicinity of sharp notches.

The polycarbonate material can be used to approximately simulate most aluminum alloys which exhibit gradual change in slope for their stress-strain curve in the non-linear range. However, the high residual stress in the as-received condition and the very poor machinability would make it virtually impossible to study three-dimensional problems where slicing is required.

4.1.2 Infinite Plate Study (Verification Phase)

Utilizing an effective stress-strain and associated birefringence curve generated during the calibration phase, an analysis of the elasto-plastic stress distributions in infinite plates with centrally located holes was conducted.

The stress concentration factors are shown in Fig. 30 as a function of the level of plasticity (σ_∞/σ_1). The thin infinite plate ($2r_o/h$) was loaded to $\sigma_\infty/\sigma_1 = 0.11$. This represented an elastic condition. The specimen was milled to 0.027-in. thick to determine a reference fringe for application of the Tardy method of compensation assuming a plane-stress condition, therefore representing a midplane slice. The measured stress-concentration factor was about 10 percent higher than for the theoretical plane-stress value. This would indicate that the assumption of plane stress for this condition was not correct. J. B. Alblas (Ref. 10) has computed an elastic stress concentration of 3.1 at the midplane of this condition ($2r_o/h$). The experimental value is about 6-1/2 percent higher than computed by Alblas. The thin plate loaded to $\sigma_\infty/\sigma_1 = 0.7$ yields an experimental stress concentration factor of 1.88. This value is approximately 4-1/2 percent higher than predicted by Budiansky (Ref. 11), and 14 percent higher than Neuber's theory predicts. The value predicted by Budiansky is for stress-strain curve with shape factor $n = 9$, whereas $n = 7$ for the experimental case. Neuber's theory (Ref. 12) considers any arbitrary stress-strain curve; the curve in Fig. 30 was derived from Neuber's theory for the stress-strain curve of the model material.

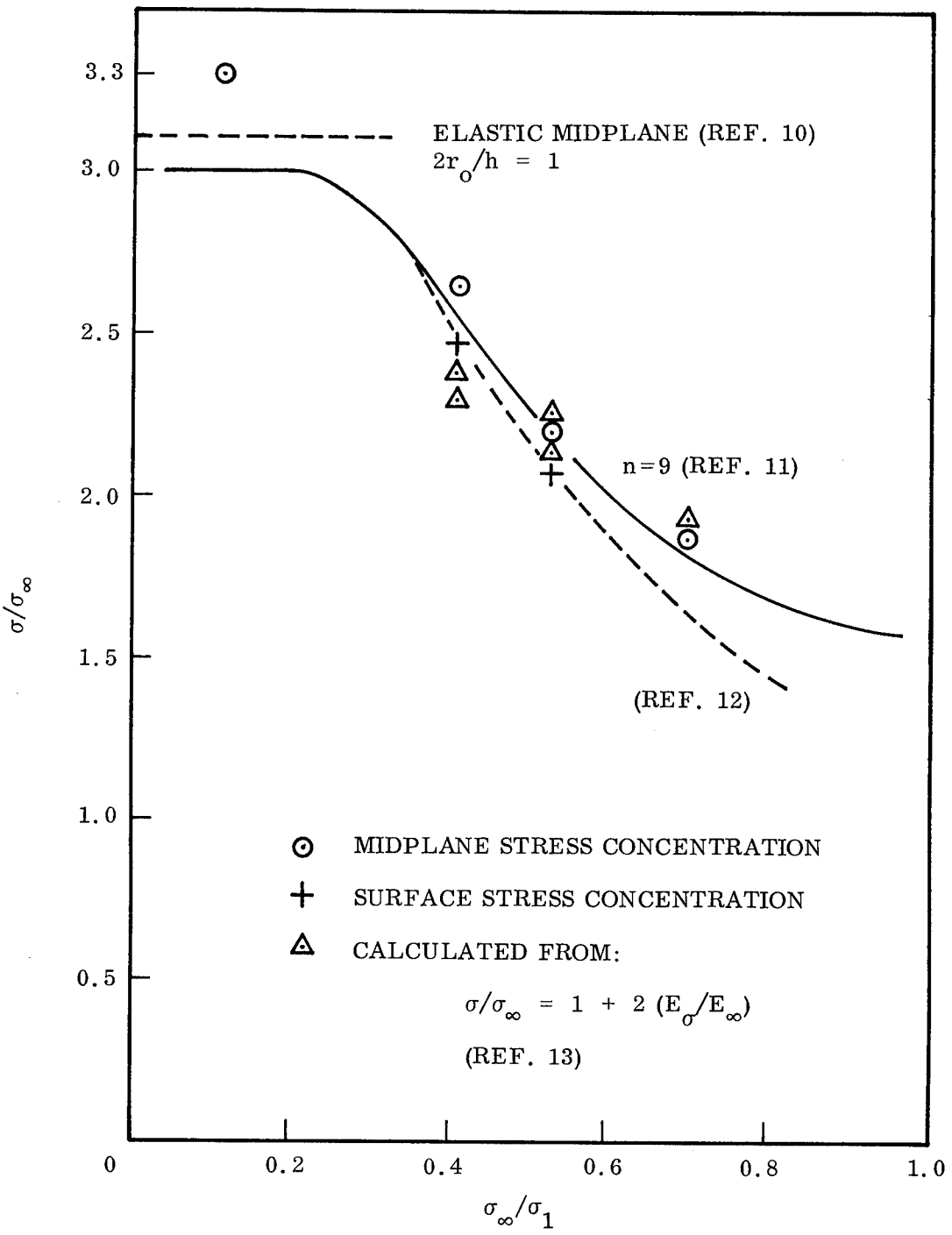

Fig. 30 Stress Concentration Factors for Various Levels of Plasticity

The thick-plate models were tested at $\sigma_\infty/\sigma_1 = 0.41$ and 0.53. The stress distributions were determined for a surface slice and for a midplane slice. The measured stresses were higher at the midplane than at the surface in the vicinity of the hole. At a short distance from the hole the stresses did not vary through the thickness. The surface and midplane stress concentrations are shown in Fig. 30. The stress concentration factors at the midplane agree very well with Budiansky (Ref. 11), and the surface stress concentration factors agree with Neuber. Due to the higher σ_x stresses at the midplane of the thick-plate models, there arises a tensile σ_z which is a maximum at midplane and edge of the hole. The σ_z stresses are zero at the surface of the thick specimens. For $\sigma_\infty/\sigma_1 = 0.41$ the maximum $\sigma_z/\sigma_\infty = 0.65$ and for $\sigma_\infty/\sigma_1 = 0.53$ the maximum $\sigma_z/\sigma_\infty = 0.8$.

Section 5

APPLICATION OF METHOD TO SIMULATED CRACKS

5.1 SPECIMEN FABRICATION FOR SIMULATED CRACKS

Molds were fabricated for casting plates with centrally located simulated cracks. These molds were made of the same epoxy resin as the specimens to eliminate the relative shrinkage between mold and casting. A 3/4-in. thick aluminum template of the configuration shown in Fig. 20 was used to cast the molds. A provision was incorporated into the molds for suspending a centrally located piece of removable shim stock to make the simulated crack in the casting. The shim stock was 0.010 in. thick and of appropriate width to provide crack lengths of 0.1, 0.5, and 0.8 in. A total of twelve molds to cast 3/4-in. thick specimens were fabricated. One such mold with shim stock in place is shown in Fig. 31. Using the shim stock to provide simulated cracks in the plates yielded a crack configuration of the type shown in Fig. 32. Twelve castings were made for each crack length, ten with simulated cracks and two unperforated plates to be used for calibration specimens. The castings were subjected to a cure cycle consisting of 160° F for 12 hr and cooled at a rate of 5° F/hr. All castings were then annealed using an annealing cycle consisting of a heating rate of 3° F/hr, soak time of 24 hr at maximum temperature of 230° F and a cooling rate of 2° F/hr. Test specimens were then machined to the appropriate thickness by fly cutting of the surface. Figure 33 shows a finished plate specimen with centrally located crack. Calibration specimens were machined to the configuration shown in Fig. 5 from the plane unperforated plates.

5.2 CALIBRATION (SIMULATED CRACK STUDY)

Calibration and generation of effective stress-strain curve was accomplished by subjecting specimens loaded to various levels of constant stress to a thermal cycle of T_{max} = 175° F. After completion of the thermal cycle, specimens were unloaded and the "frozen" strain and birefringence (n/t) were determined as a function of the

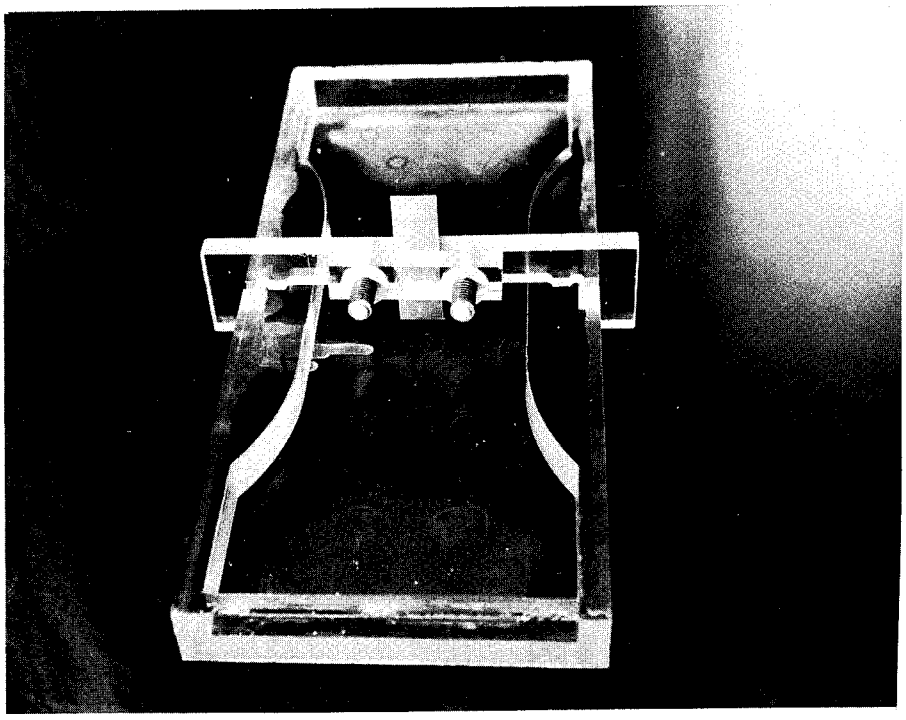

Fig. 31 Mold For Casting Plates with Simulated Cracks

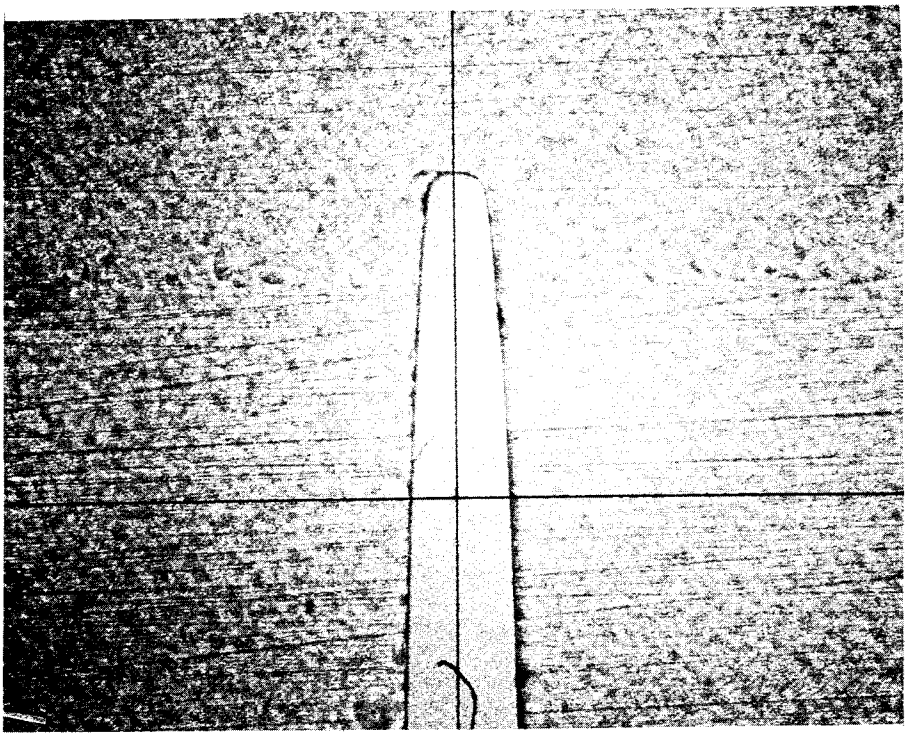

Fig. 32 Simulated Crack Tip Configuration (After Test)

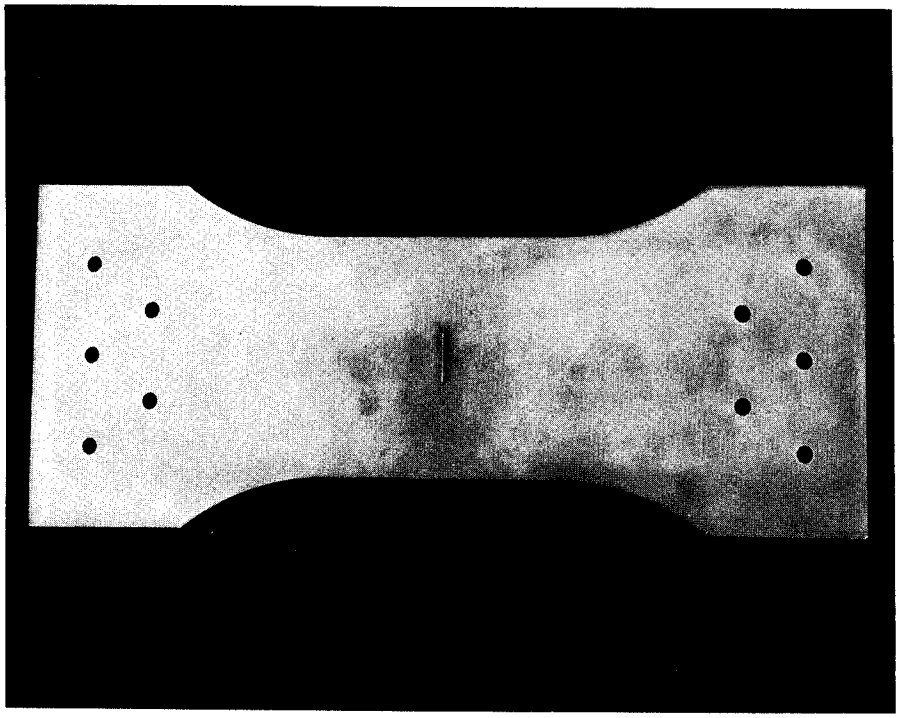

Fig. 33 Plate Specimen with Centrally Located Simulated Crack

stress. The details of the calibration were similar to those described previously in Section 3.1.1.

The results of the calibration are shown in Figs. 34 through 37. Figure 34 represents the relationship between stress and "frozen" strain for a thermal cycle of $T_{max} = 175°F$. Calibration tests were not performed for samples representative of castings of all three crack lengths. Great care was taken to ensure that all castings experienced the same cure and annealing environment. It was therefore assumed that calibration tests performed on samples representative of the 0.5 crack length castings would be valid for the other crack lengths. To check the validity of this assumption, three samples representative of the 0.8 crack length castings were tested. These data are shown in the figures. Figure 35 shows this stress-strain curve in nondimensional form. Figure 36 shows the relation between stress and birefringence and Fig. 37 between strain and birefringence. This information will be used to determine the photoelastoplastic stress distributions from birefringence (n/t).

5.3 PHOTOELASTIC ANALYSIS OF SIMULATED CRACKS

Plates containing centrally located cracks were tested to determine the elastic stress distribution in the vicinity of the crack tip. For the elastic analysis plates of 0.1 in. thick were tested, having crack lengths (ℓ_{cr}) of 0.1, 0.5, and 0.8 in. The photoelastic "frozen" stress technique and shear difference method was used. The coordinate system used here is as shown in Fig. 23. That is, x corresponds to the load direction and y normal to the load direction with origin at the crack tip. The results are shown in Figs. 38 through 40. The stress concentration factor in a very flat ellipse or a narrow crack with a very small notch radius can be approximately calculated by:

$$\frac{\sigma_x}{\sigma_g} = 2\sqrt{c/\rho} + 1 \quad \text{(Ref. 15)} \tag{6}$$

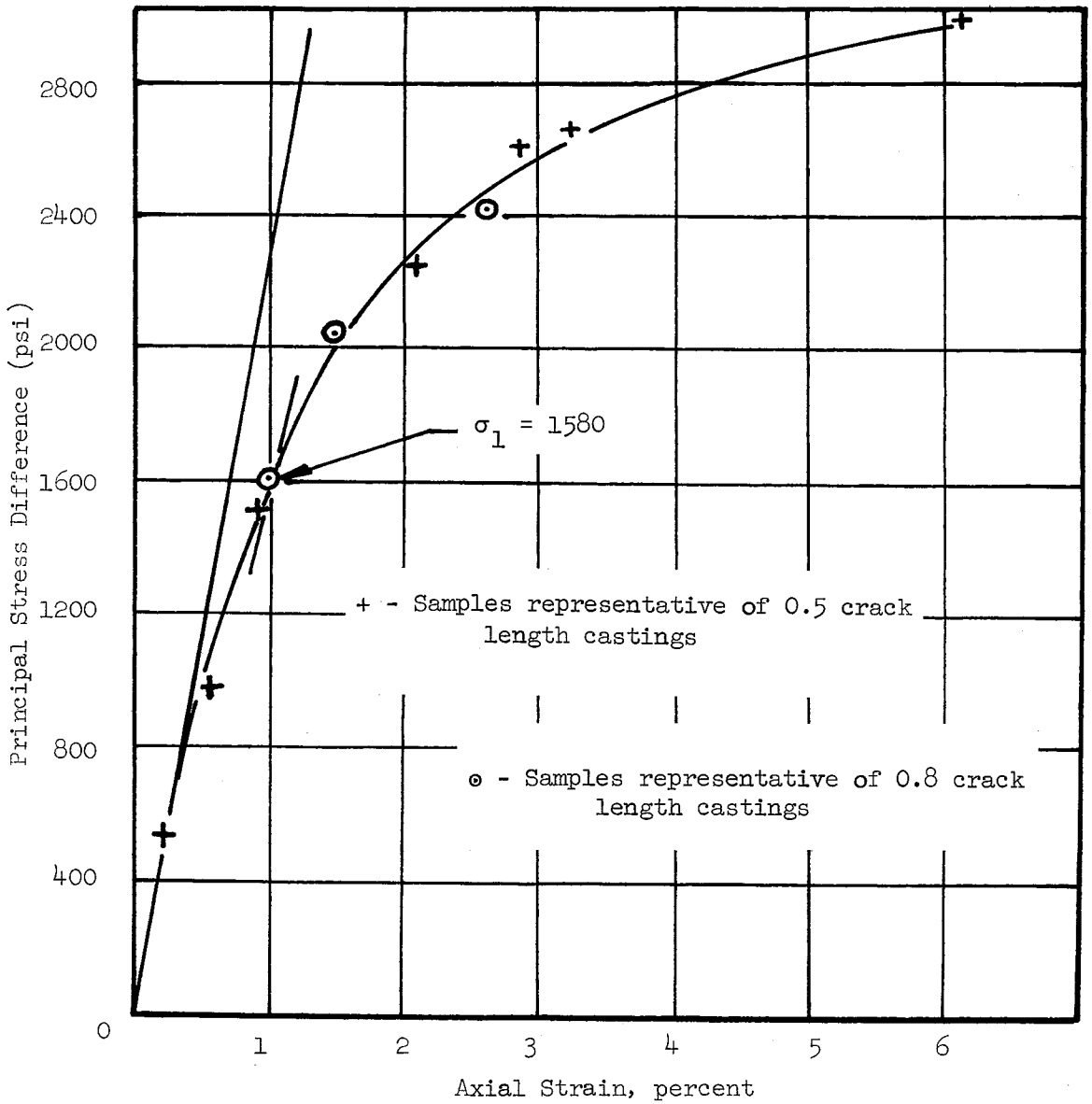

Fig. 34 Effective Stress-Strain Curve For Thermal Cycle (T_{max} = 175°F), E = 213,000 psi

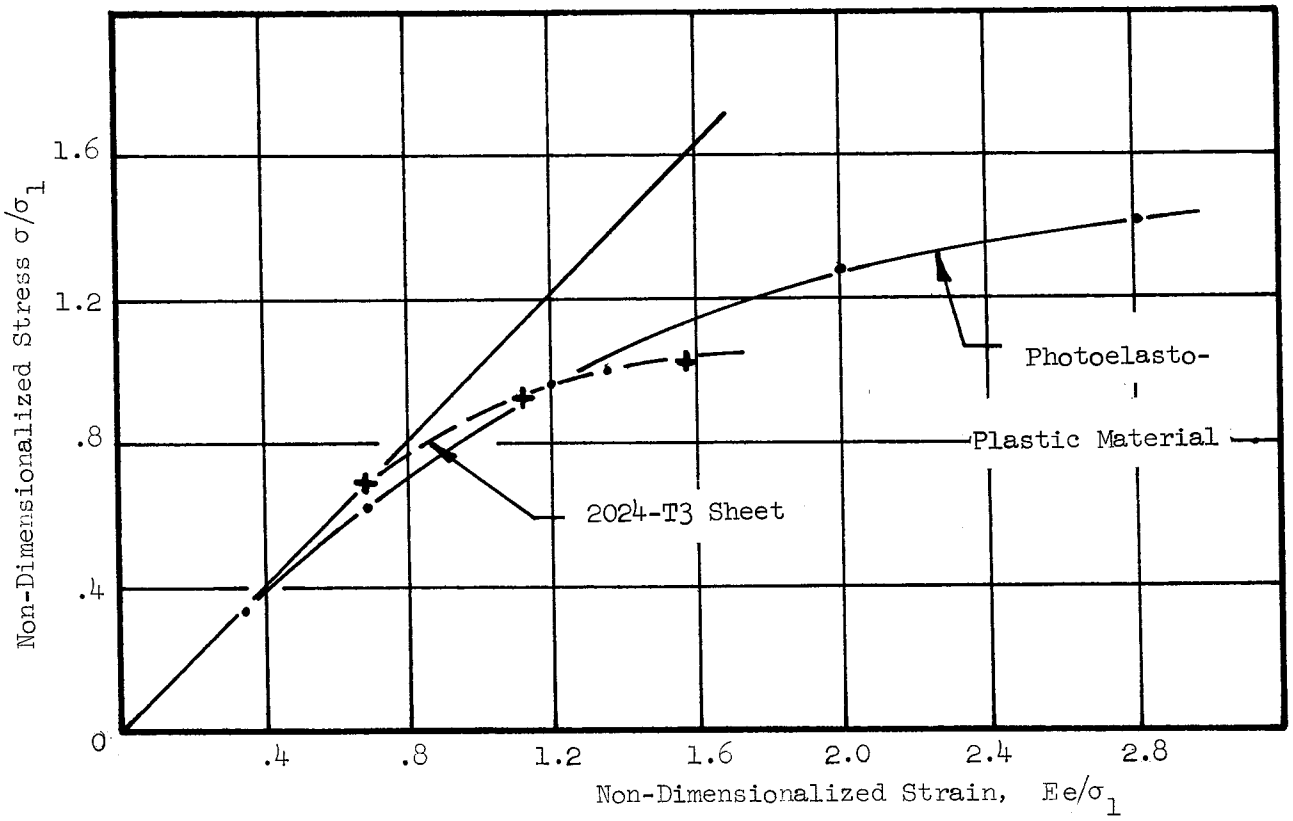

Fig. 35 Non-Dimensionalized Stress-Strain Curve for Simulated Crack Study (T_{max} = 175°F)

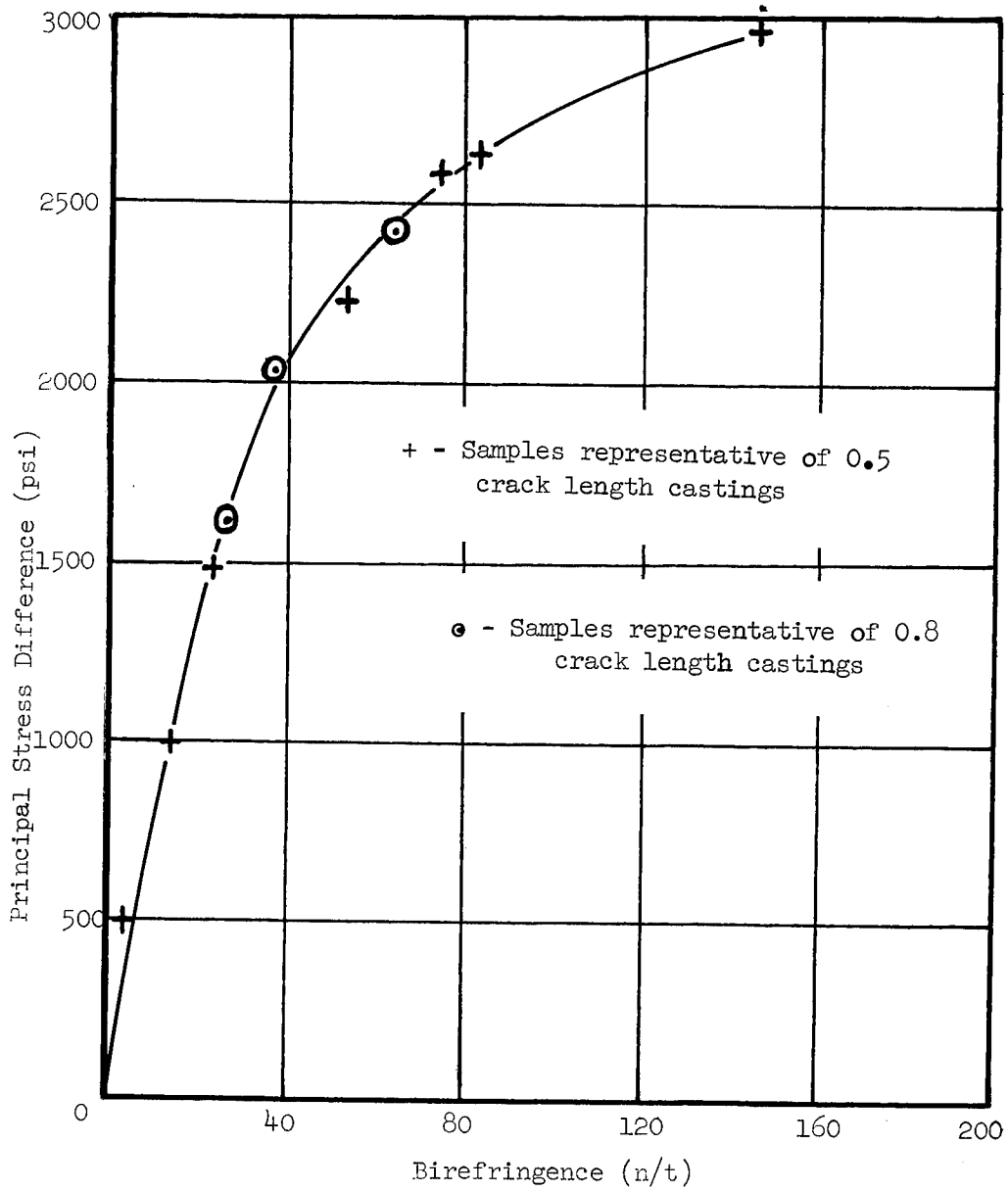

Fig. 36 Stress-Optical Calibration Curve For Thermal Cycle (T_{max} = 175°F)

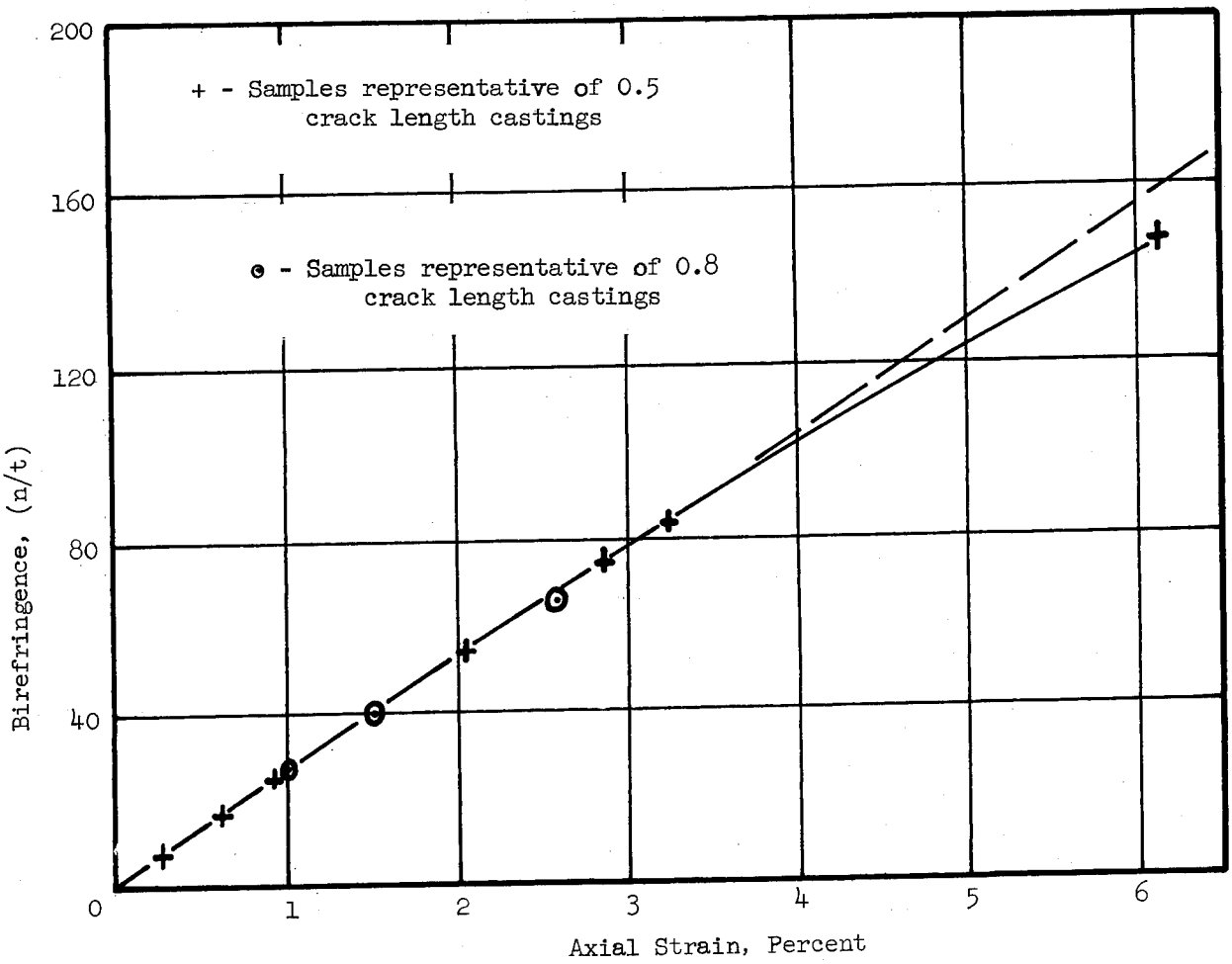

Fig. 37 Strain-Optical Calibration Curve For Thermal Cycle (T_{max} = 175°F)

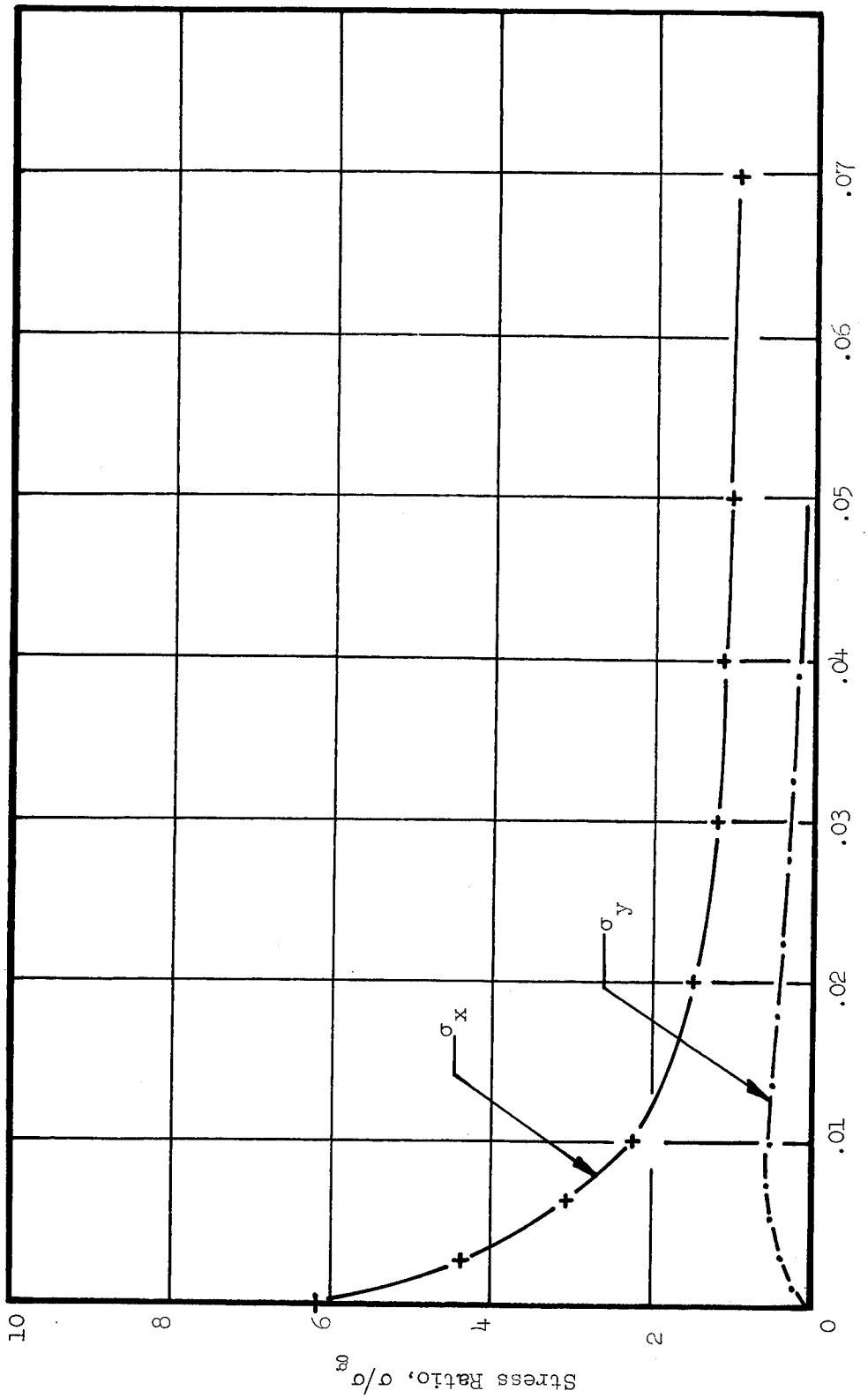

Fig. 38 Elastic Stress Distribution, ℓ_{cr} = .10 and t = .10

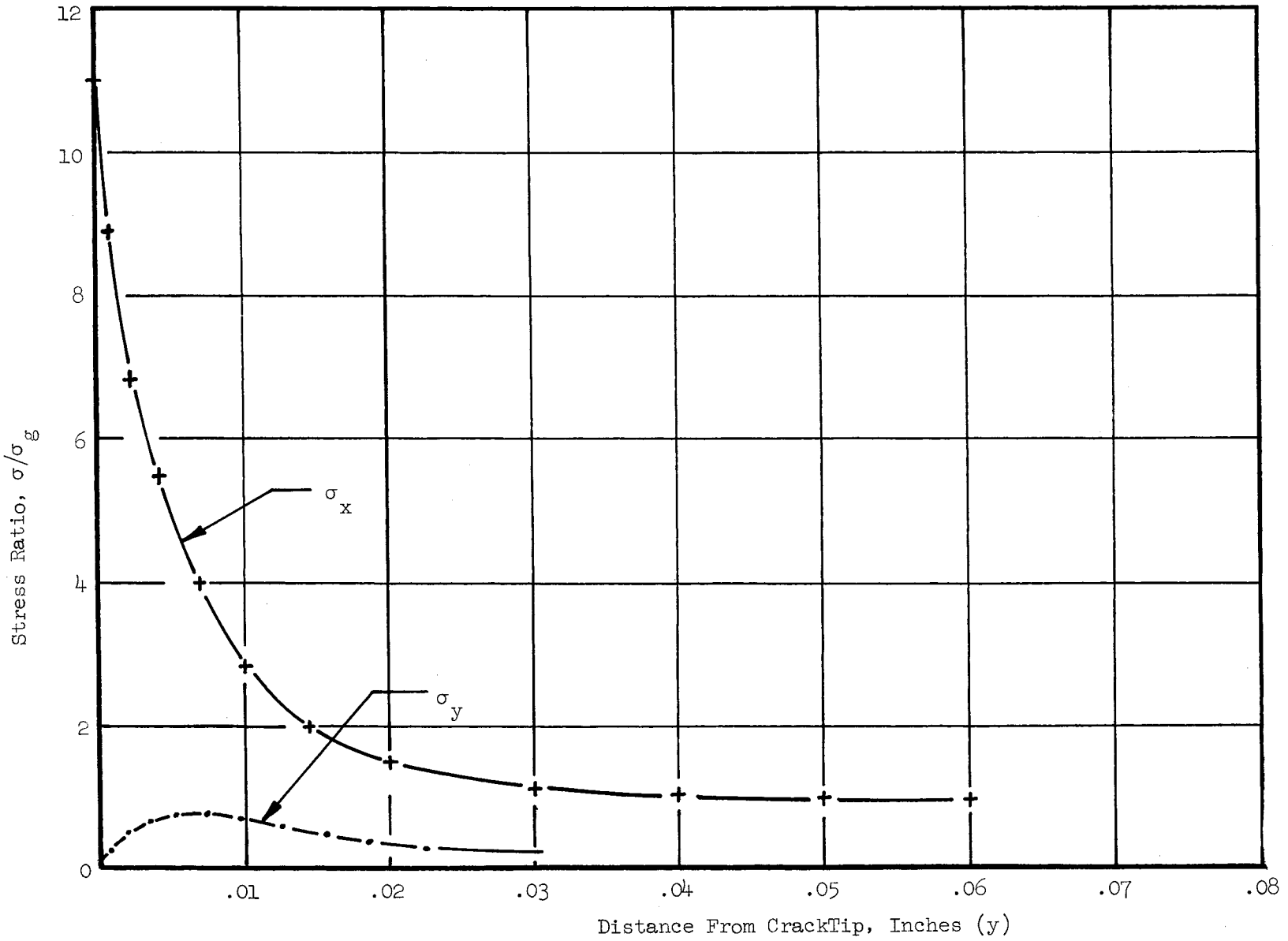

Fig. 39 Elastic Stress Distribution, ℓ_{cr} = 0.5 and t = 0.1

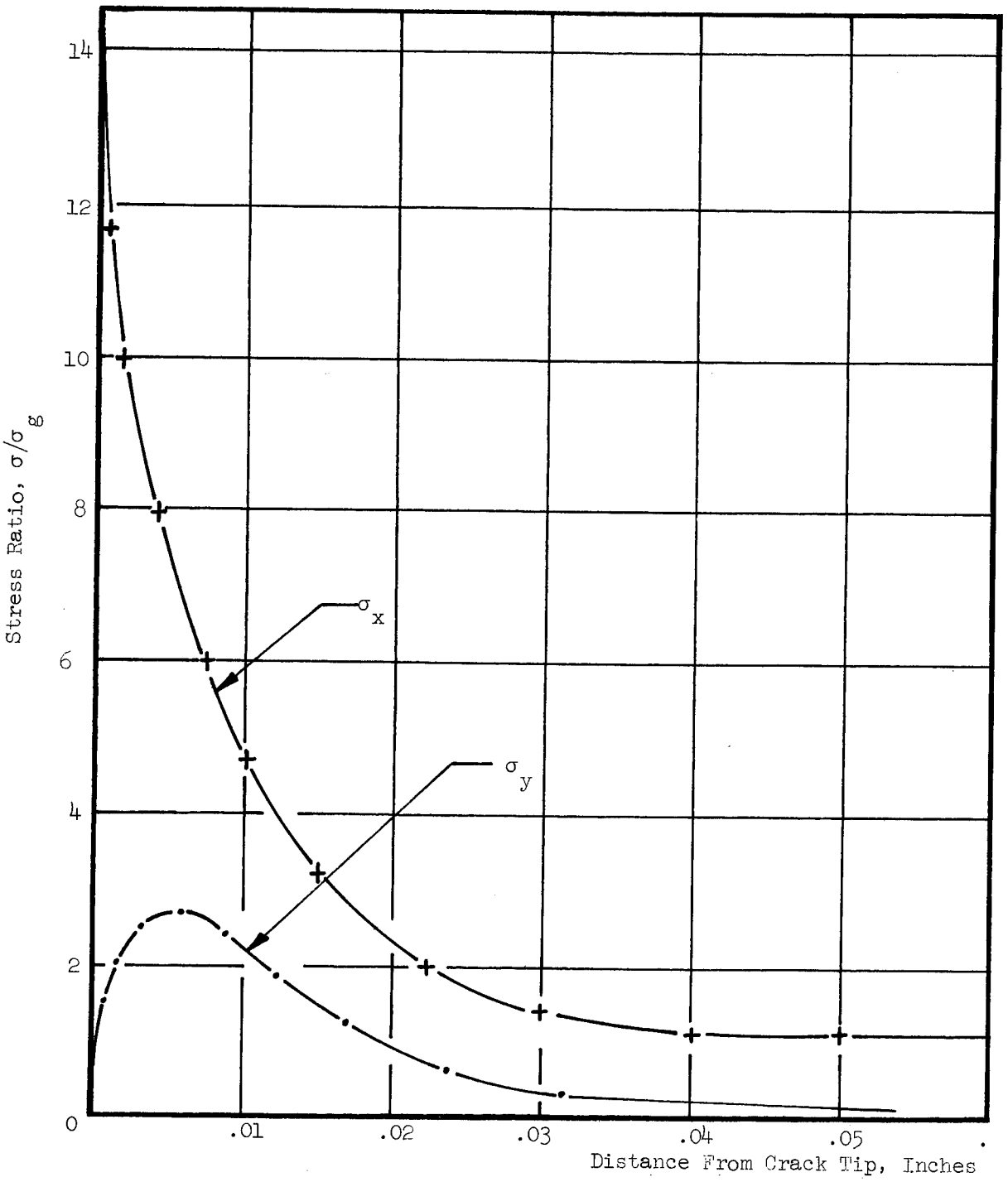

Fig. 40 Elastic Stress Distribution, ℓ_{cr} = .80 and t = .10

where

c = one-half the crack length

ρ = radius of curvature of the notch $\rho \cong 0.005$

Using this simple relationship, we obtain a calculated elastic stress concentration factor for the 0.8 in. crack length of 18.9 and for the 0.5 in. crack a value of 15.2, and for the 0.1 in. crack length a value of 7.35. A comparison between measured stress concentration factors and those computed from the above equation are compared in Fig. 41.

5.4 PHOTOELASTO-PLASTIC ANALYSIS OF SIMULATED CRACKS

Plates containing centrally located simulated cracks were tested to determine the effect of plate thickness and crack length on three-dimensional elasto-plastic stress distributions. Three crack lengths were considered (ℓ_{cr} = 0.1, 0.5, and 0.8 in.). For each crack length three plate thicknesses (t = 0.1, 0.3, and 0.5 in.) were tested at two levels of plasticity. Table I summarizes the test conditions for the photoelasto-plastic analysis of plates containing centrally located simulated cracks.

5.4.1 Acquisition and Reduction of Photoelasto-Plastic Data

After freezing the elasto-plastic stress patterns into the plates for each of the test conditions shown in Table I, the plates were sliced according to the same scheme used for the infinite plates with holes (Fig. 26). Surface slices were approximately 0.010 in. thick while midplane slices were of the order of 0.020 in. thick. Measurement of birefringence was accomplished by use of a photo cell connected to a photo multiplier. Light intensity was recorded as a function of the y coordinate on an x-y plotter. Calibration of the system is necessary. This was accomplished using a diametral disk for which the fringe distribution is known or can be calculated along the line of symmetry normal to load direction by:

$$\frac{n}{t} = \frac{2P}{\pi dtf}\left[\left(\frac{d^2 - 4x^2}{d^2 + 4x^2}\right) + \frac{4d^4}{(d^2 + 4x^2)^2} + 1\right] \quad \text{(Ref. 16)} \qquad (7)$$

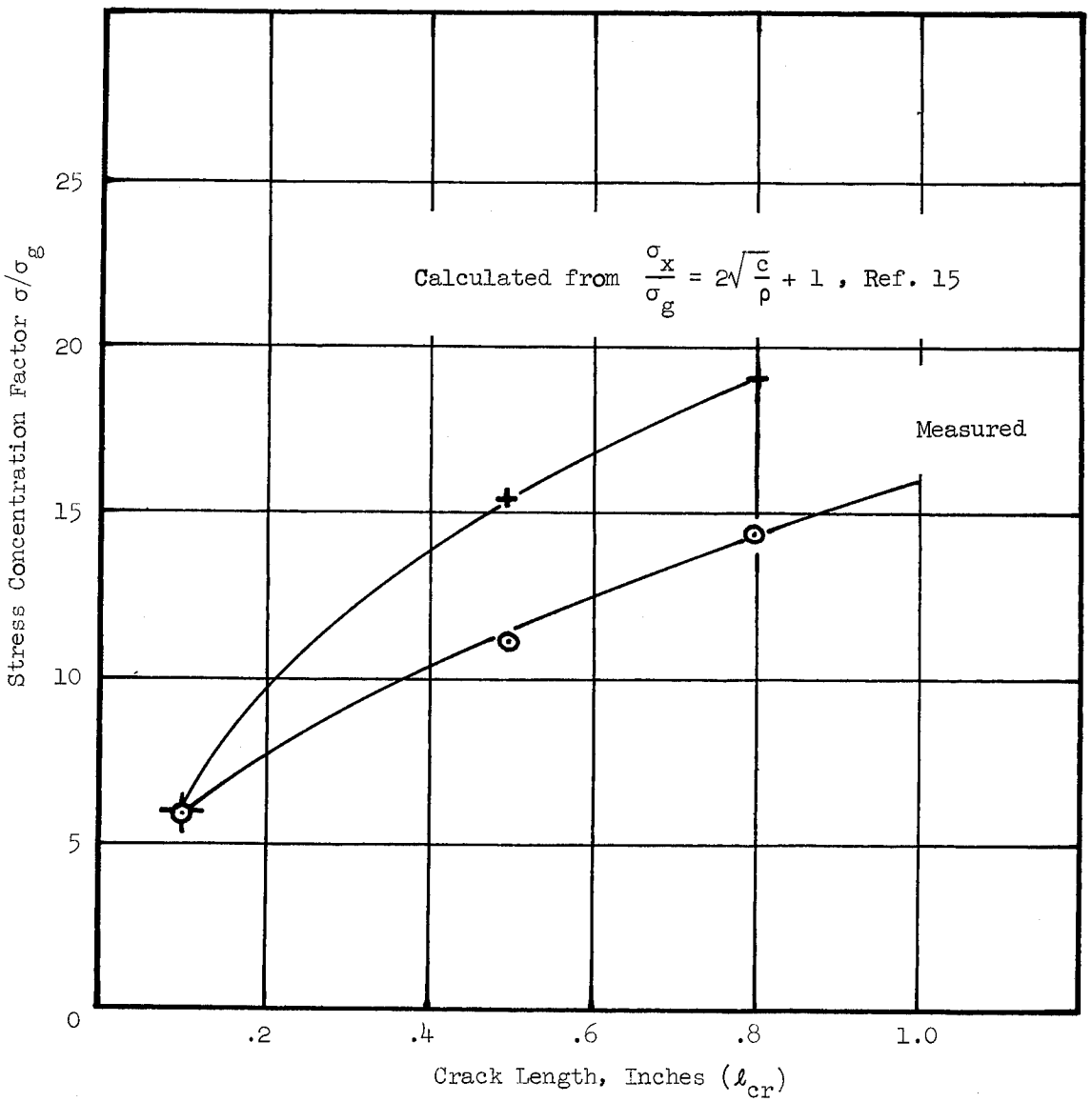

Fig. 41 Comparison of Measured and Computed Elastic Stress Concentration Factors as a Function of Crack Length

Table I

SUMMARY OF TEST CONDITIONS FOR PHOTOELASTO-PLASTIC ANALYSIS OF PLATES CONTAINING CENTRALLY LOCATED SIMULATED CRACKS

ℓ_{cr}	t	$\frac{\sigma_g}{S_1}$	$\frac{\ell_{cr}}{w}$	$\frac{\ell_{cr}}{t}$	$\left(\frac{\sigma_x}{\sigma_g}\right)_s$	$\left(\frac{\sigma_x}{\sigma_g}\right)_{MP}$	$\left(\frac{\sigma_x}{\sigma_g}\right)_{s\ max}$	$\left(\frac{\sigma_x}{\sigma_g}\right)_{MP\ max}$	$\left(\frac{\sigma_y}{\sigma_g}\right)_{s\ max}$	$\left(\frac{\sigma_y}{\sigma_g}\right)_{MP\ max}$	$\left(\frac{\sigma_z}{\sigma_g}\right)_{MP\ max}$	$\left(\frac{\sigma_z}{\sigma_g}\right)_{MP}$
0.1	0.1	.177	.025	1.00	4.30	4.20	4.50	4.25	0.70	0.73	1.45	1.0
0.1	0.1	.262	.025	1.00	3.35	3.40	3.56	4.05	0.73	0.87	1.50	0.85
0.1	0.3	.177	.025	0.33	3.05	3.70	3.16	3.84	0.77	0.73	1.63	1.34
0.1	0.3	.248	.025	0.33	3.25	2.94	3.66	3.30	1.18	1.20	1.75	1.05
0.1	0.5	.158	.025	0.20	3.58	3.56	3.68	3.72	0.78	0.80	1.20	0.84
0.1	0.5	.240	.025	0.20	3.18	2.64	3.58	3.05	0.85	0.82	1.55	1.30
0.5	0.1	.209	.125	5.00	6.15	6.10	6.80	6.90	1.77	2.80	-	-
0.5	0.1	.280	.125	5.00	4.80	5.60	5.65	7.30	1.80	2.75	-	-
0.5	0.3	.280	.125	1.67	4.34	4.96	4.72	5.35	1.00	1.41	2.25	1.70
0.5	0.3	.354	.125	1.67	4.06	4.40	4.58	5.32	1.45	2.30	2.80	1.30
0.5	0.5	.209	.125	1.00	4.70	5.30	5.20	5.80	2.05	2.20	3.05	1.80
0.5	0.5	.278	.125	1.00	4.60	4.80	5.50	5.90	2.60	2.80	3.55	1.70
0.8	0.1	.095	.20	8.00	10.30	11.30	11.80	12.50	4.00	4.20	-	-
0.8	0.1	.126	.20	8.00	11.00	11.00	12.50	11.60	4.20	4.05	-	-
0.8	0.1	.190	.20	8.00	-	7.60	-	9.80	-	3.80	-	-
0.8	0.3	.126	.20	2.67	6.00	8.10	6.80	10.95	2.55	3.60	4.50	1.38
0.8	0.3	.190	.20	2.67	5.30	7.30	7.00	10.30	3.00	4.00	5.20	1.40
0.8	0.5	.126	.20	1.60	7.10	7.20	9.50	9.40	4.02	4.00	5.50	2.10
0.8	0.5	.190	.20	1.60	4.90	5.80	7.30	7.50	3.75	4.00	5.80	2.20

MP - Indicates midplane, $z = 0$

s - Indicates surface, $z = h/2$ where h is plate thickness

where

P = diametral load
d = diameter of disk
f = stress optical coefficient
t = disk thickness

The diametral disk is then placed in the polariscope and at the same magnification (40×) as used for the slice analysis the disk is traversed past the photo cell opening. The photo cell measures the average light intensity within its field (aperture). This field size and magnification determines essentially the gage length of the measurement. The field size (aperture opening) of the photocell sensor was approximately 0.005 in. in diameter. At 50× magnification this would result in a gage length of 0.0001 in. The traverse across the disk provides on an x-y recorder the light intensity distribution as a function of the distance from the edge of the disk. A typical curve of this nature is shown in Fig. 42. Based upon the dimensions of the disk, applied load, and stress optical coefficient, a plot of fringe order as a function of distance from the edge of the disk can be made. A typical plot of this nature is shown in Fig. 43.

From Figs. 42 and 43 a cross plot is made of fringe order as a function of light intensity and such a plot is shown in Fig. 44. Therefore from traverses made on an actual slice it is possible to determine the fringe order at each point from the measured light intensity. Figure 45 represents a plot of light intensity as a function of distance from crack tip for an actual slice.

5.4.1.1 Photoelasto-Plastic Measurement Procedure

A traverse of the type shown in Fig. 45 is generated along line OY (Fig. 46). This provides a distribution of the principal stress difference along the line of symmetry. Another traverse is then made along a line O'Y' displaced from the line of symmetry by a small amount $\Delta x/2$ (0.003 in.). Also the directions of the principal stresses were determined along O'Y' by use of the photo cell (measuring angle θ at minimum intensity). A typical distribution of the directions (θ) are shown in Fig. 47.

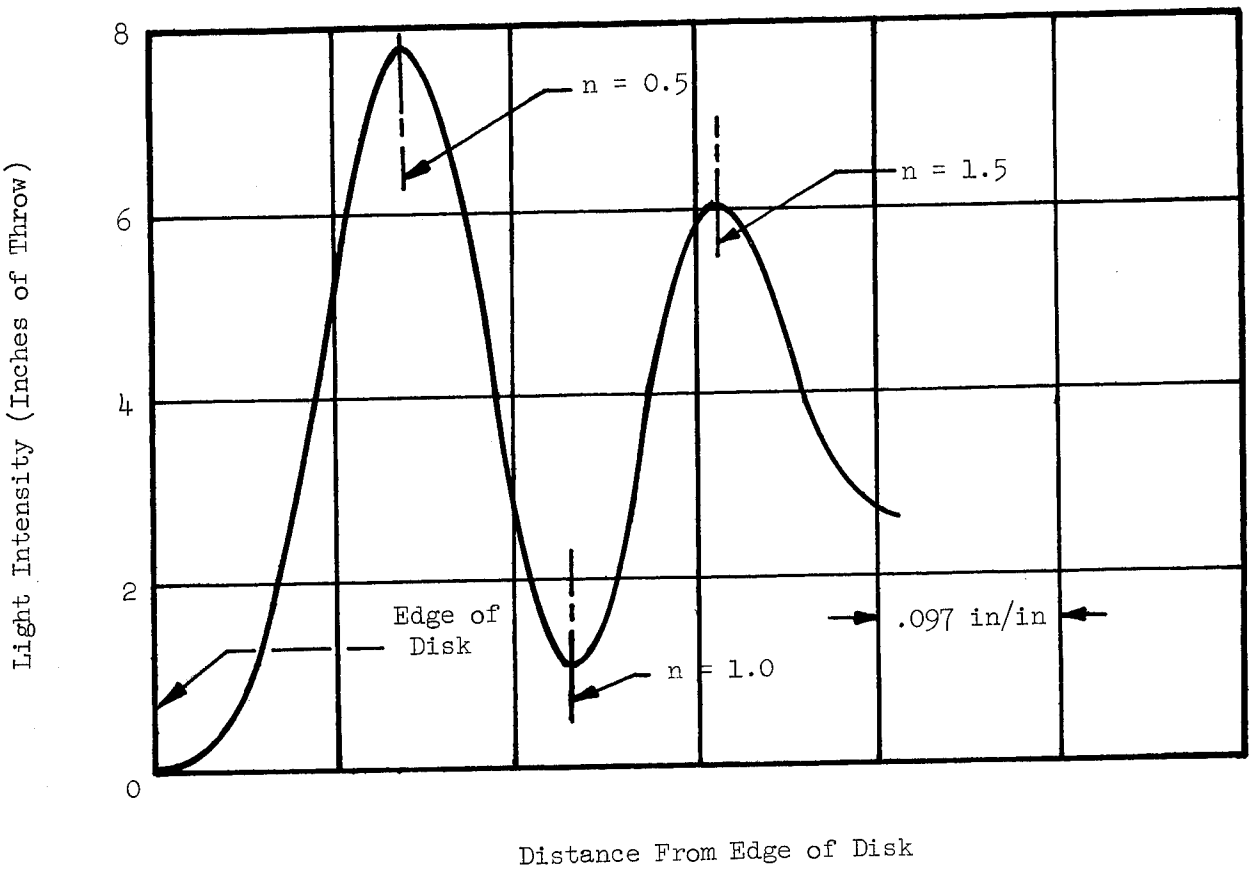

Fig. 42 Light Intensity Distribution as Function of Distance From Edge of Diametral Compression Disk

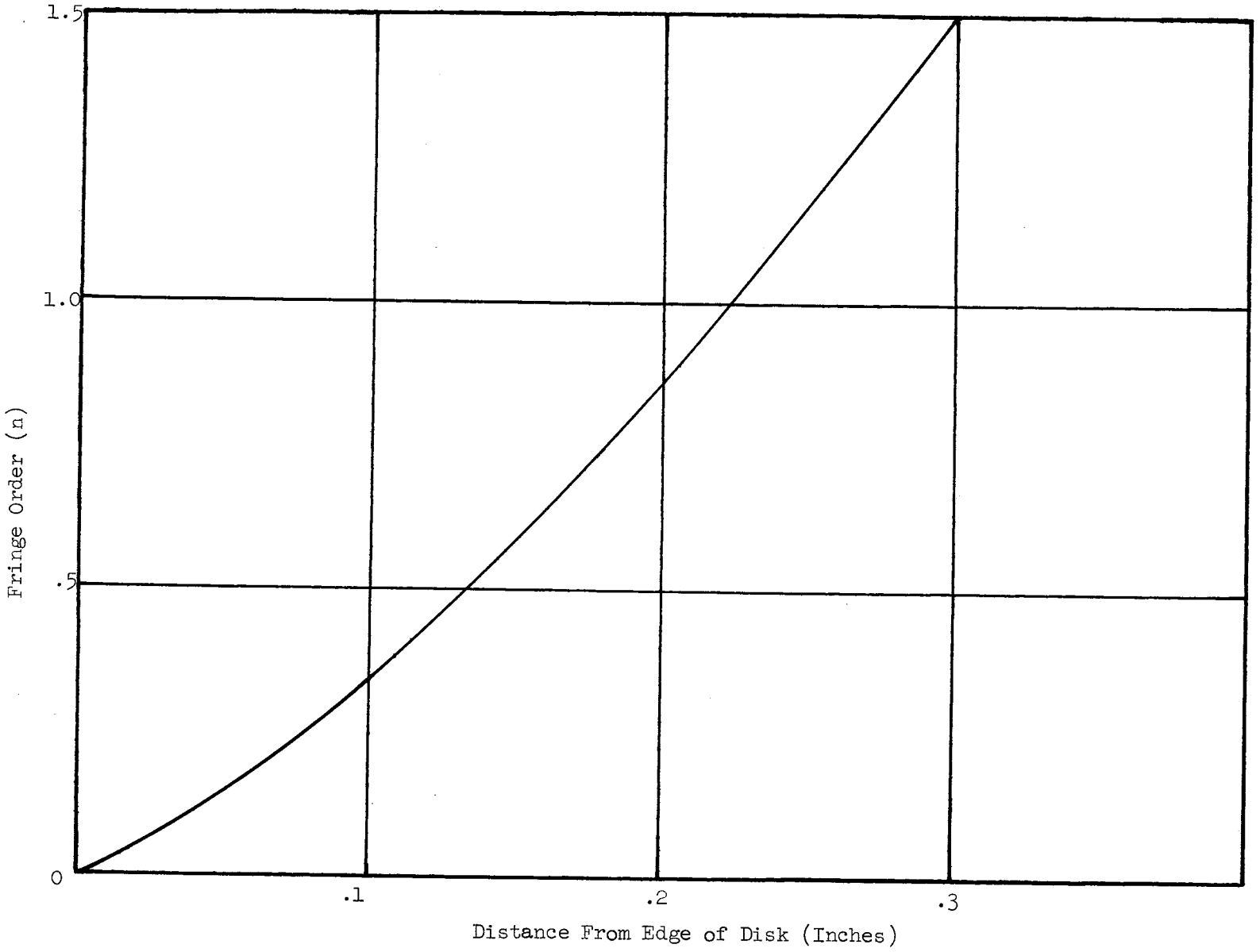

Fig. 43 Fringe Order Distribution From Edge of Diametral Compression Disk

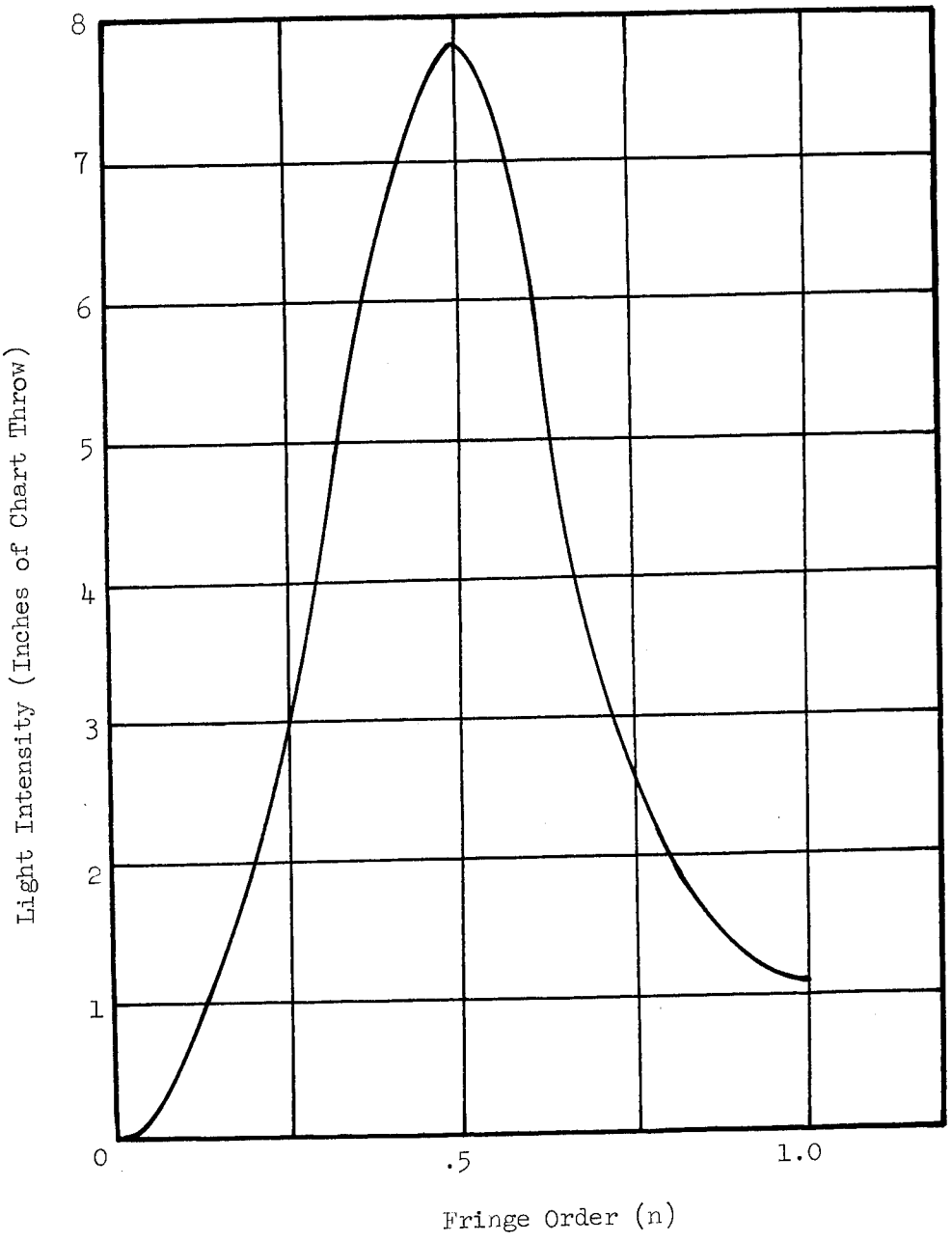

Fig. 44 Light Intensity as a Function of Fringe Order

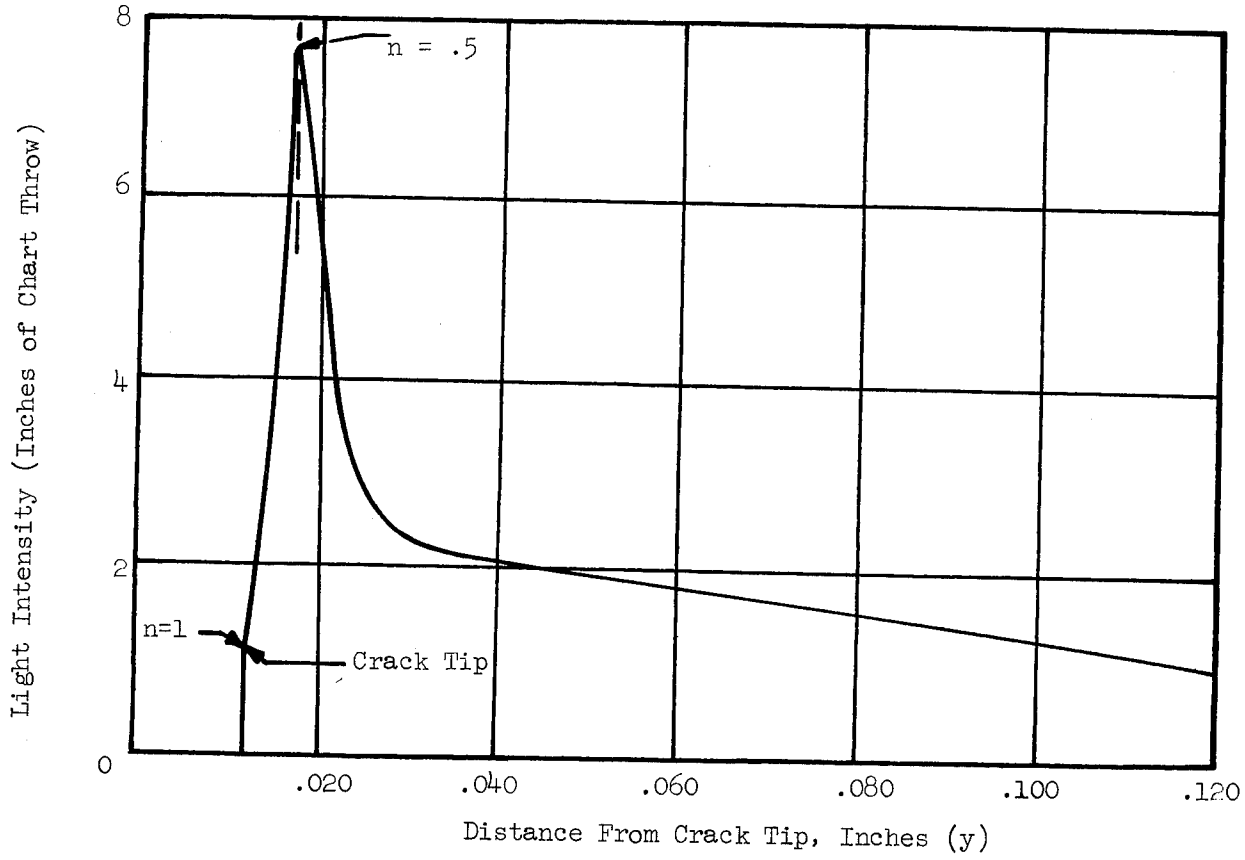

Fig. 45 Typical Light Intensity Distribution from Tip of Crack

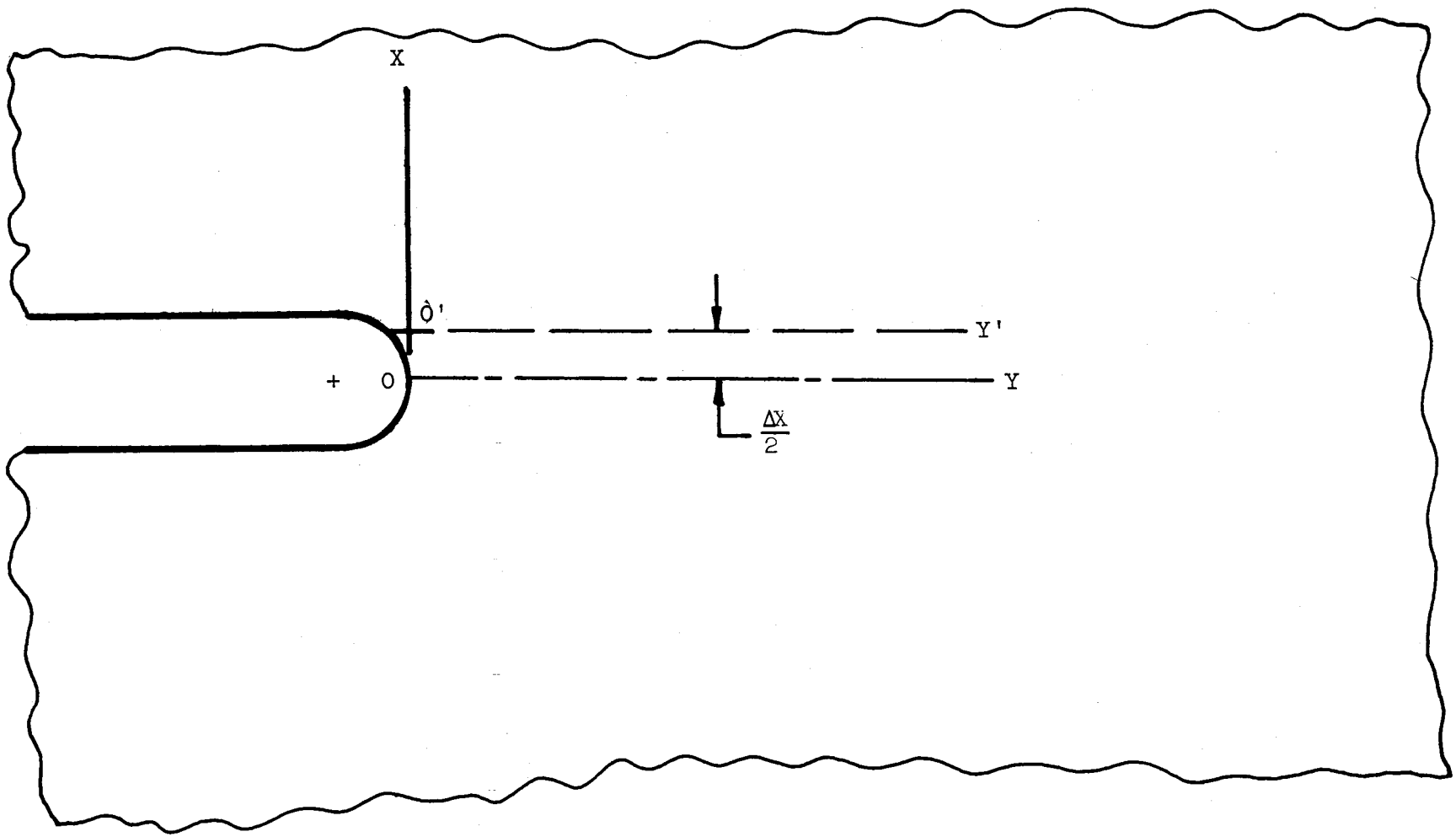

Fig. 46 Typical Slice Configuration Showing Measurement Coordinates

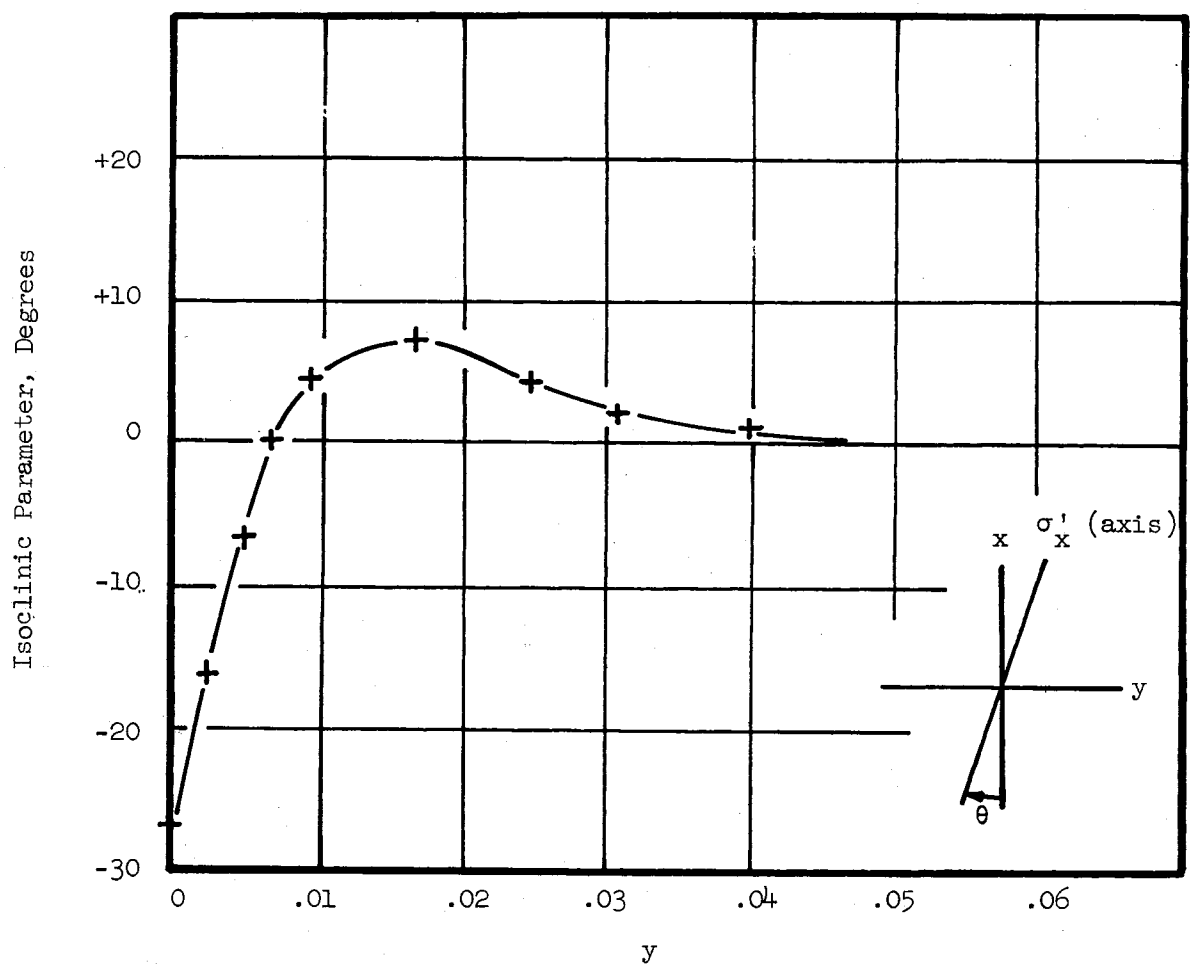

Fig. 47 Distribution Principal Stress Direction Along O'Y'

Consider the equation of equilibrium

$$\frac{\partial \sigma_y}{\partial y} + \frac{\partial \tau_{xy}}{\partial x} + \frac{\partial \tau_{zy}}{\partial z} = 0 \tag{8}$$

from which we have

$$(\sigma_y)_i = (\sigma_y)_o - \sum_o^i \frac{\Delta \tau_{xy}}{\Delta x} \Delta y - \sum_o^i \frac{\Delta \tau_{zy}}{\Delta z} \Delta y \tag{9}$$

Assuming

$$\frac{\Delta \tau_{zy}}{\Delta z} \cong 0$$

then,

$$(\sigma_y)_i = (\sigma_y)_o - \sum_o^i \frac{\Delta \tau_{xy}}{\Delta x} \Delta y \tag{10}$$

Using data of the type shown in Figs. 45 and 47, the shear stress distribution along O'Y' is computed by

$$\tau_{xy} = (\sigma_x - \sigma_y/2) \sin 2\theta \tag{11}$$

$$\frac{\Delta \tau_{xy}}{2} = (\tau_{xy})_{OY} - (\tau_{xy})_{O'Y'} \tag{12}$$

From this equation the $\Delta\tau_{xy}/\Delta x$ as a function of y may be derived. A typical curve for $\Delta\tau_{xy}/\Delta x$ is shown in Fig. 48. Since $\sigma_y = 0$ at $x = 0$, $y = 0$, Eq. (10) becomes

$$(\sigma_y)_i = -\sum_{o}^{i} \frac{\Delta\tau_{xy}}{\Delta x} \Delta y \tag{13}$$

Therefore, by graphical integration of data of type shown in Fig. 48, information is provided as to the σ_y stress distribution along the y axis. Knowing the $\sigma_x - \sigma_y$ distribution and σ_y distribution along y, the principal stress distribution (σ_x) can be determined.

The distribution of the stress component σ_z was determined along the y axis for $z = 0$. Information as to the $\sigma_z - \sigma_y$ stresses was determined from photoelasto-plastic observations of a transverse slice as illustrated in Fig. 26b. A typical distribution of the $\sigma_z - \sigma_y$ stresses as a function of y for $z = 0$ is shown in Fig. 49. Then from the σ_y distribution, the σ_z distribution is determined.

5.4.2 Presentation of Results for Photoelasto-Plastic Analysis of Plates Containing Cracks

The coordinate axis used in the presentation of the photoelasto-plastic results for plates with cracks is indicated in Fig. 26. Three slices were removed from the test specimens, midplane, surface and transverse slices as indicated in Fig. 26. The photoelasto-plastic analysis of these slices yield the σ_x, σ_y, and σ_z stress distributions as a function of y at the crack tip. The shear difference method of analysis was used to determine these stress components. The details concerning this analysis procedure was described in Section 4.4.1.1.

The elasto-plastic analysis was performed for three crack lengths, each for three plate thicknesses and each combination tested at two levels of plasticity. These test conditions are summarized in Table I. The results are shown in Figs. 50 through 86.

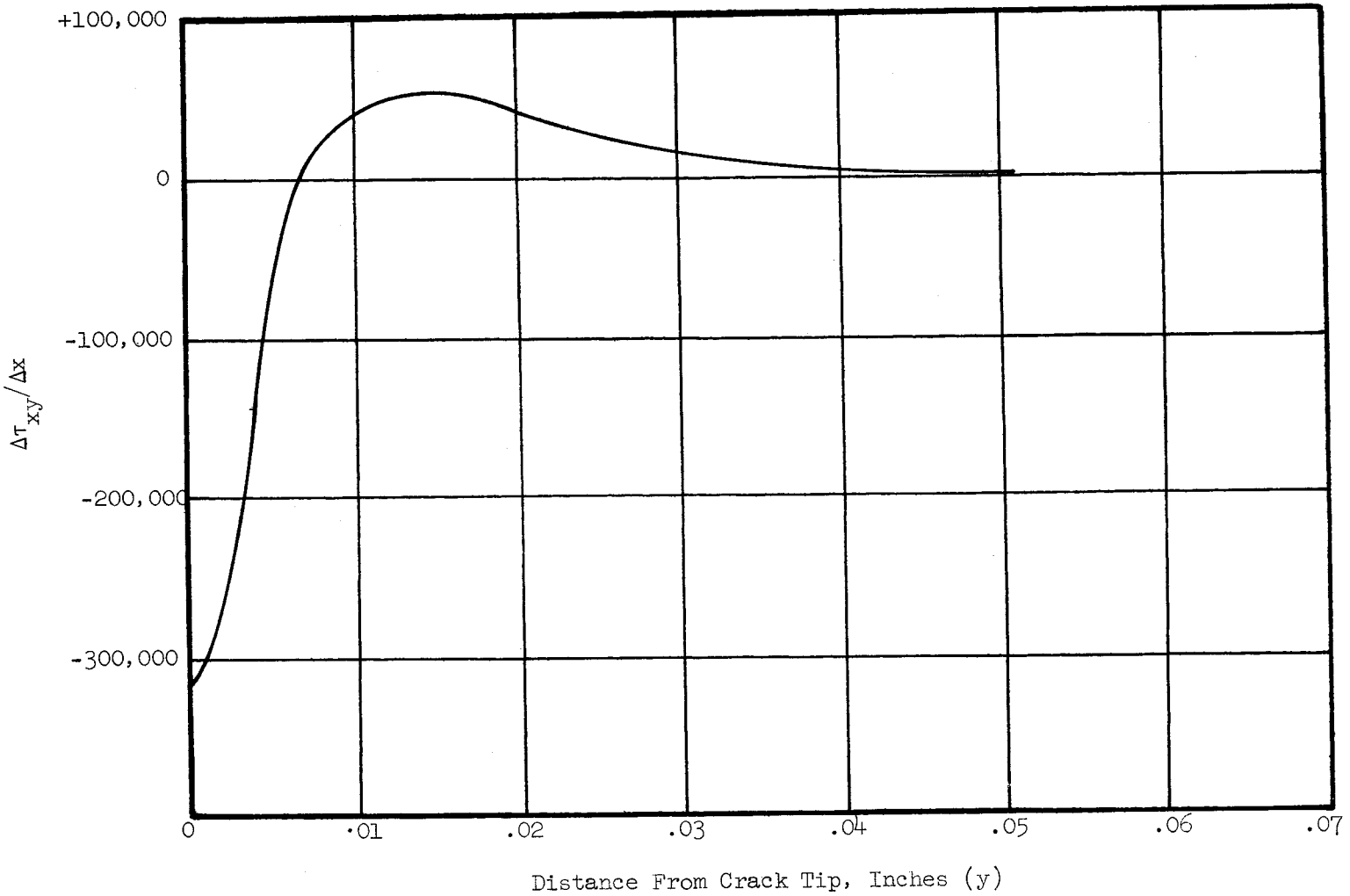

Fig. 48 Typical Distribution of $(\Delta\tau_{xy}/\Delta x)$ as a Function of y

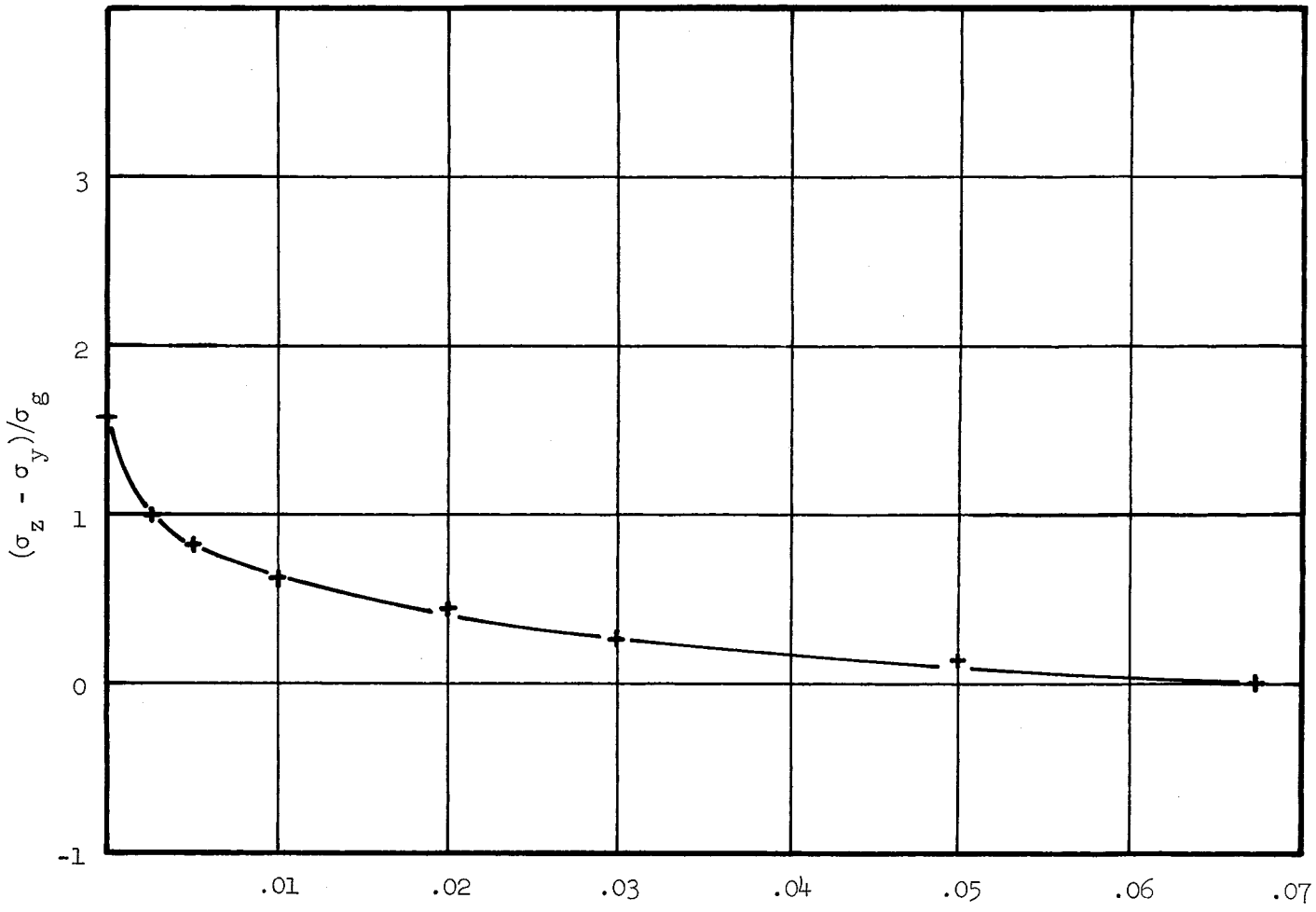

Fig. 49 Typical Distribution of $(\sigma_z - \sigma_y)$ Stresses Along y for z = 0

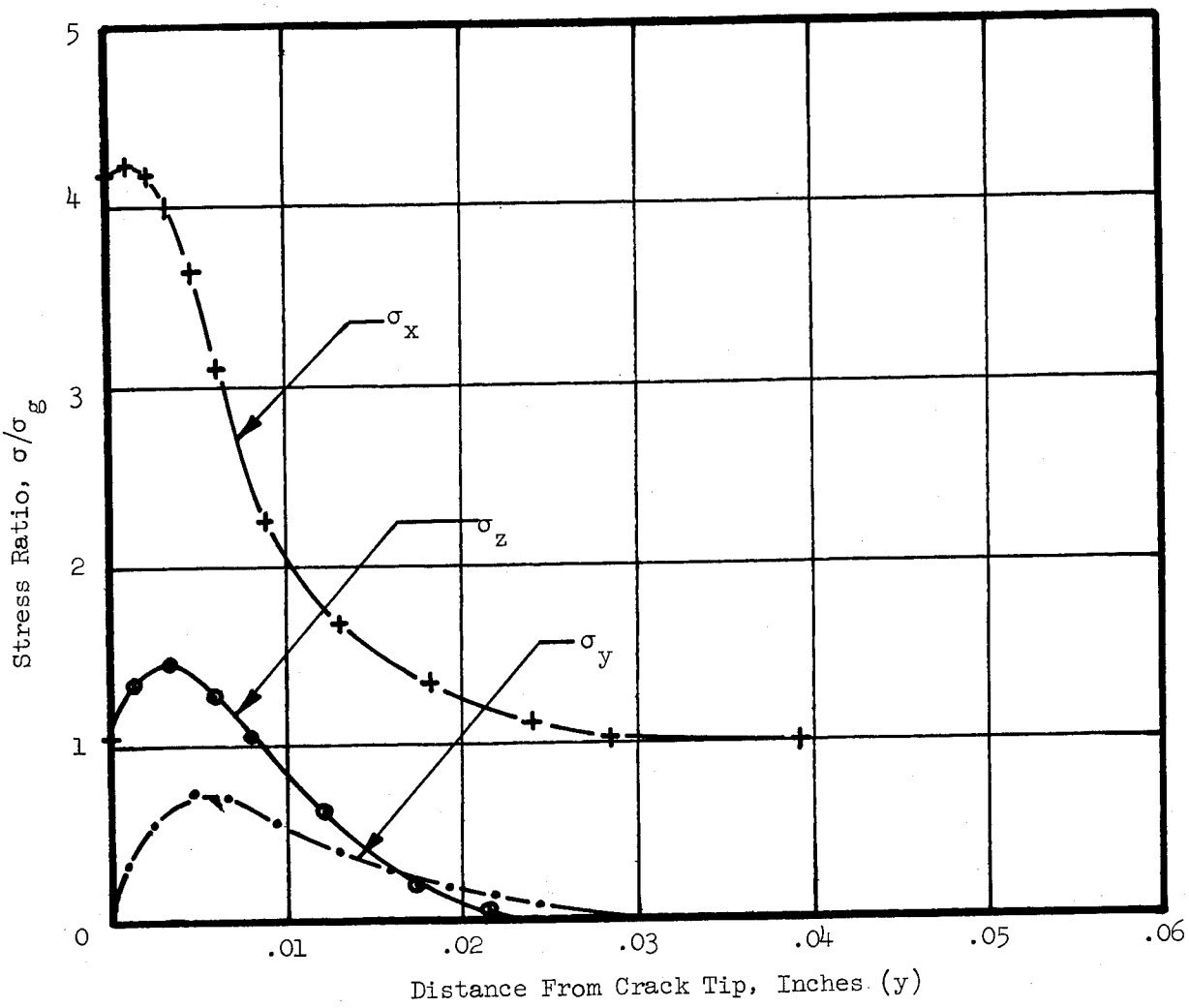

Fig. 50 Elasto-Plastic Stress Distributions, $\ell_{cr} = 0.1$, $t = 0.1$, $z = 0$, and $\sigma_g/\sigma_1 = .177$

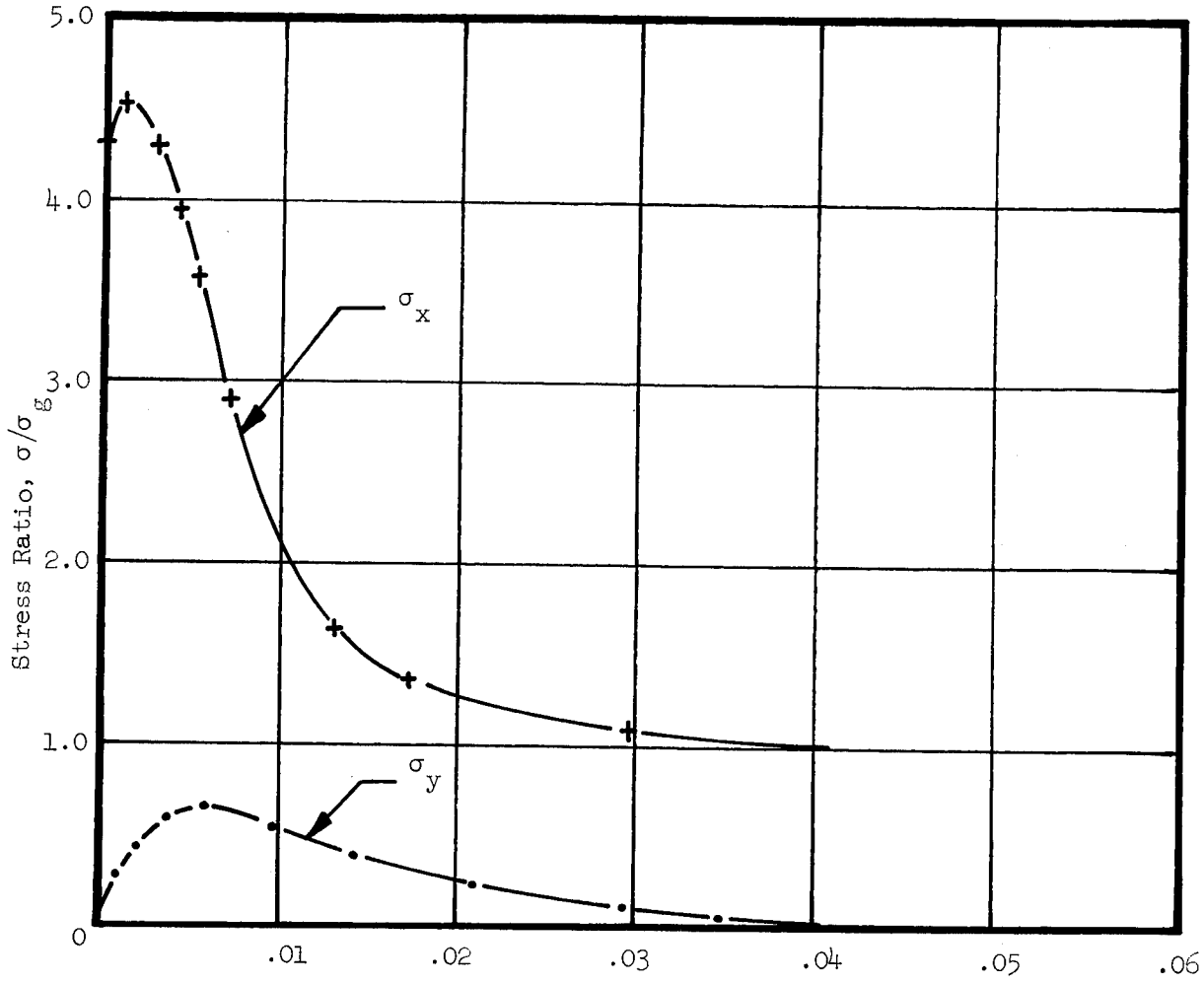

Fig. 51 Elasto-Plastic Stress Distributions, $\ell_{cr} = 0.1$, $t = 0.1$, $z = .05$ and $\sigma_g/\sigma_1 = .177$

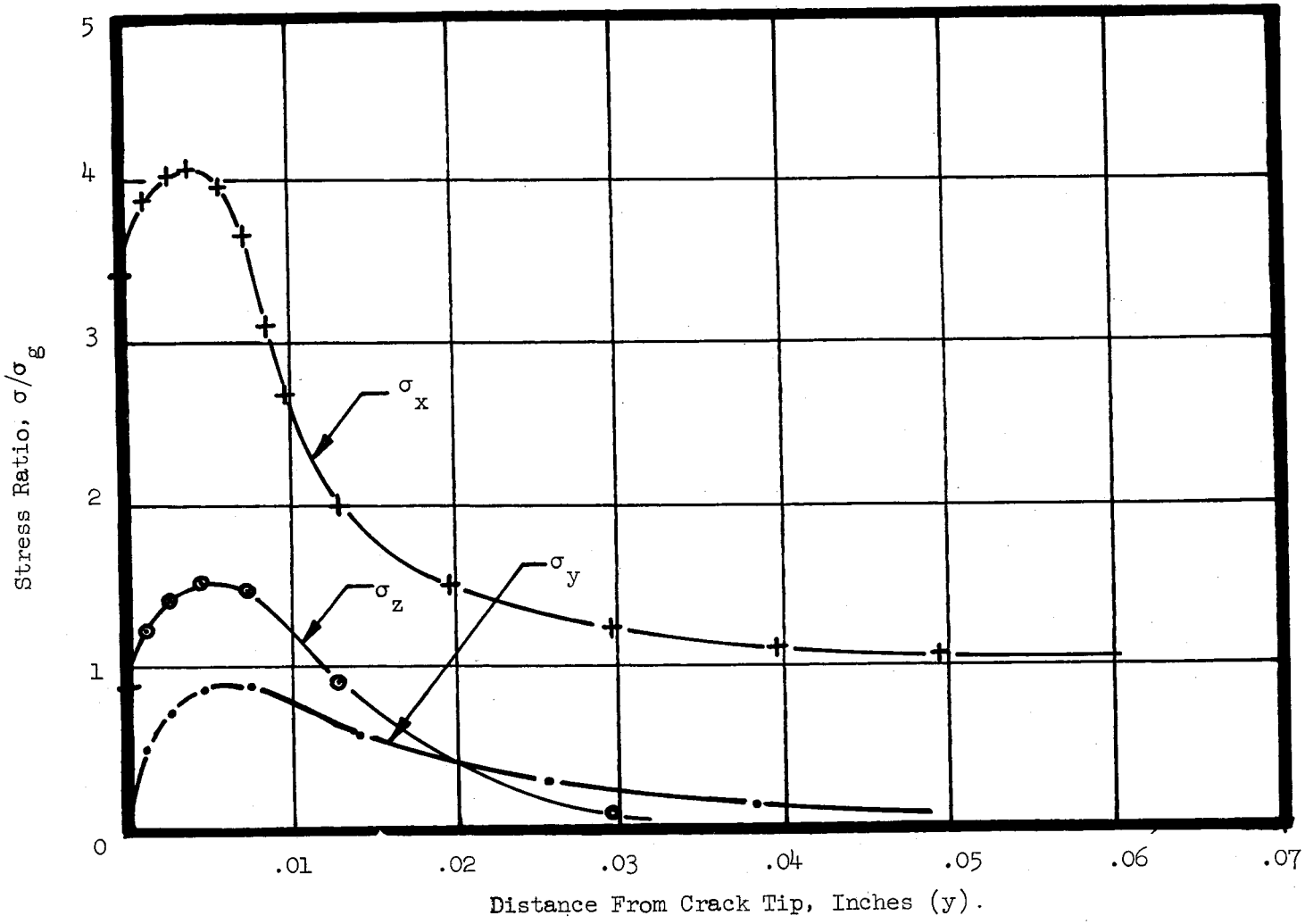

Fig. 52 Elasto-Plastic Stress Distributions, ℓ_{cr} = .1, t = .1, z = 0, and σ_g/σ_1 = .262

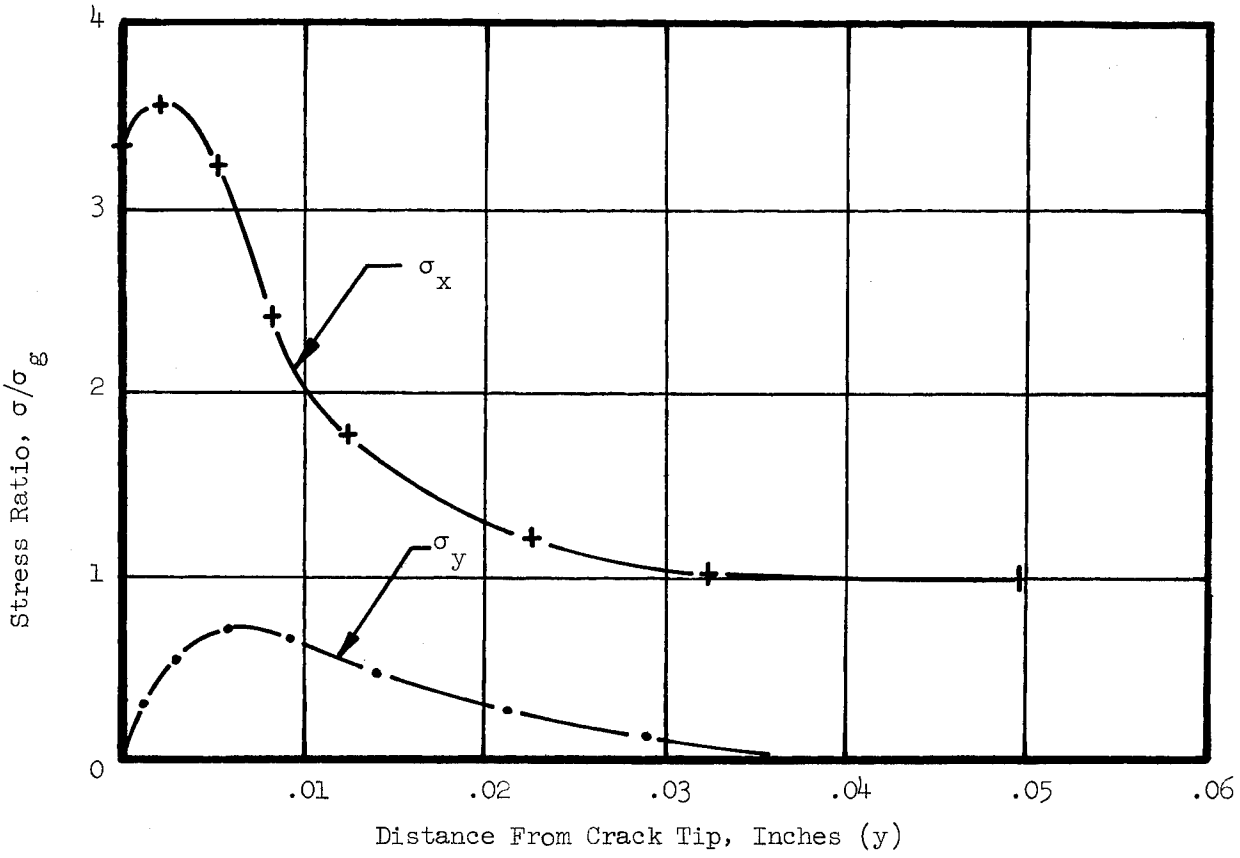

Fig. 53 Elasto-Plastic Stress Distributions, $\ell_{cr} = 0.1$, $t = 0.1$, $z = .05$ and $\sigma_g/\sigma_1 = .262$

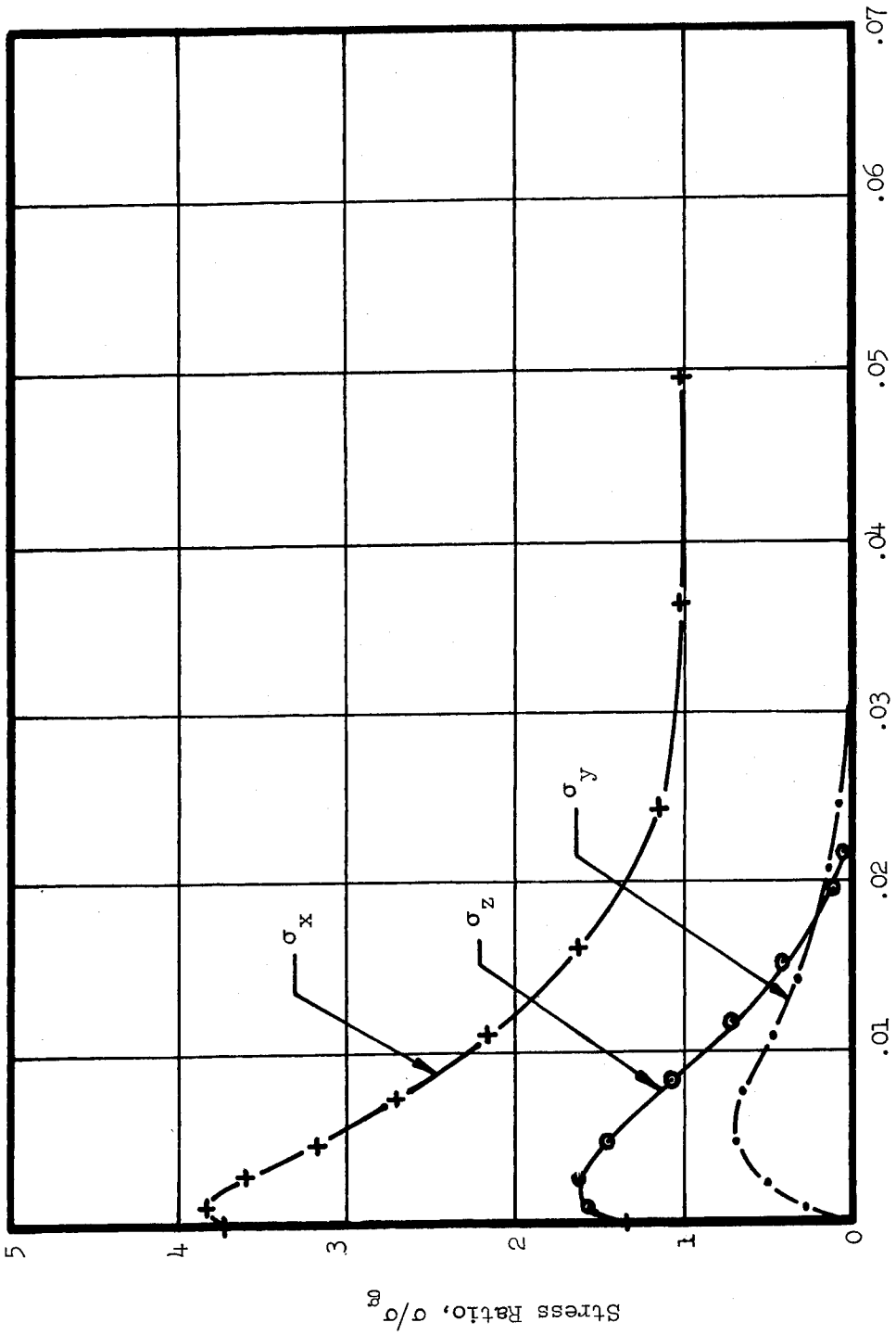

Fig. 54 Elasto-Plastic Stress Distributions, $\ell_{cr} = 0.1$, $t = 0.3$, $z = 0$ and $\sigma_g/\sigma_1 = .177$

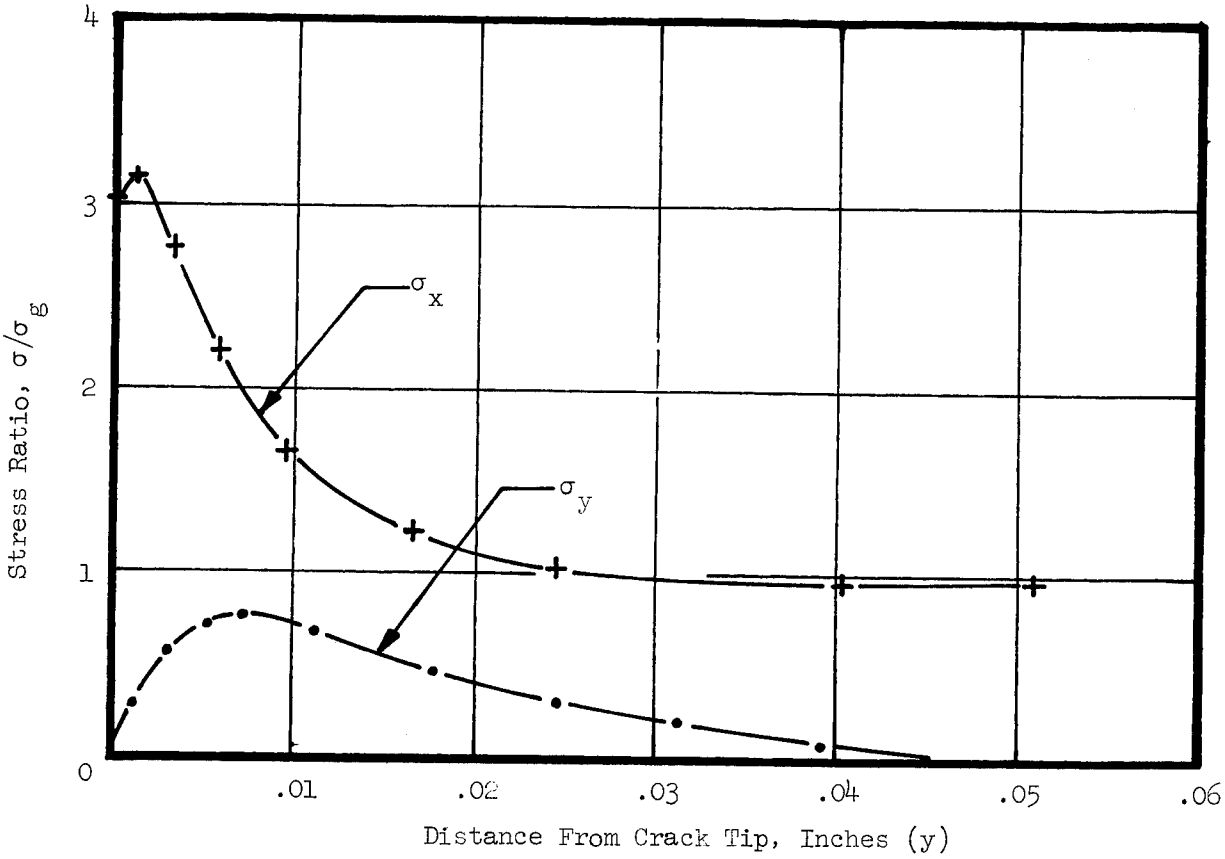

Fig. 55 Elasto-Plastic Stress Distributions, ℓ_{cr} =0.1, t =0.3, z = .15, and σ_g/σ_1 = .177

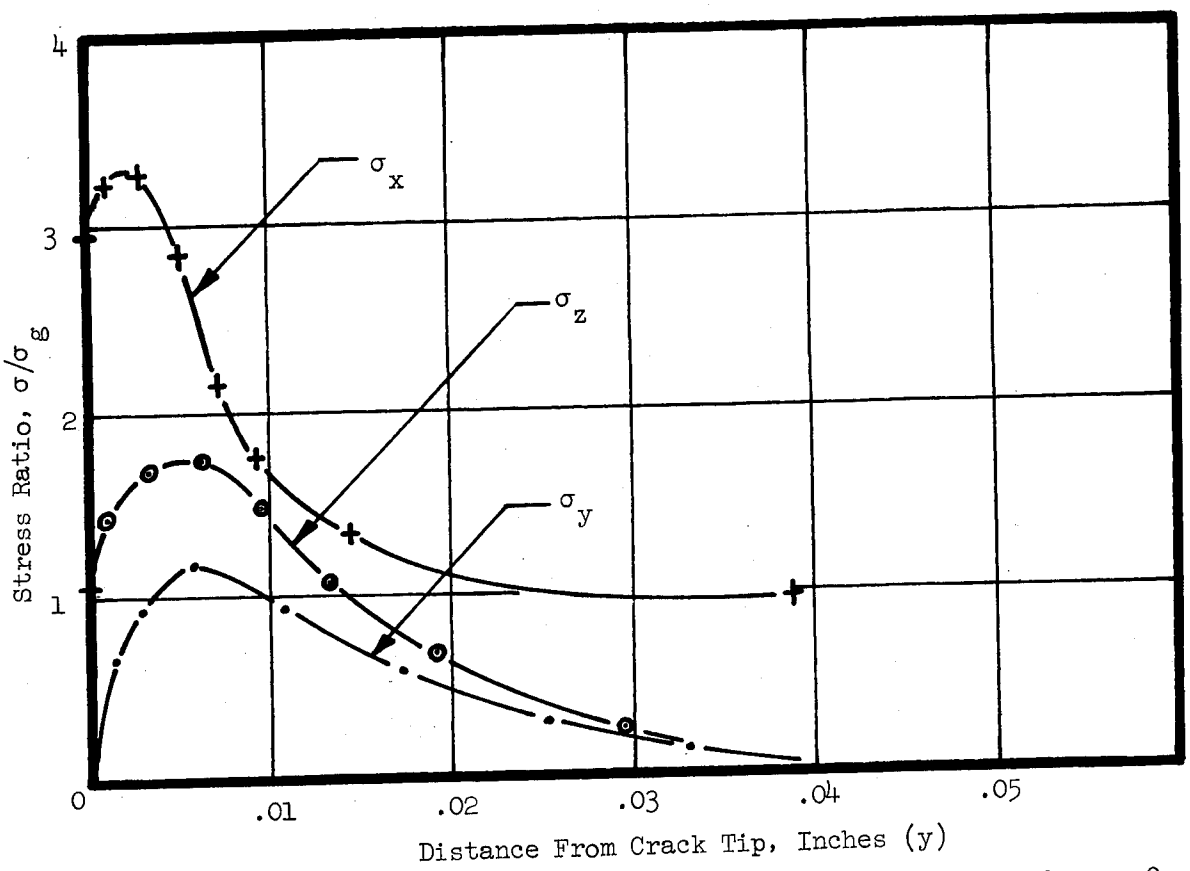

Fig. 56 Elasto-Plastic Stress Distributions, $\ell_{cr} = 0.1$, t = 0.3, z = 0

$\sigma_g/\sigma_1 = .248$

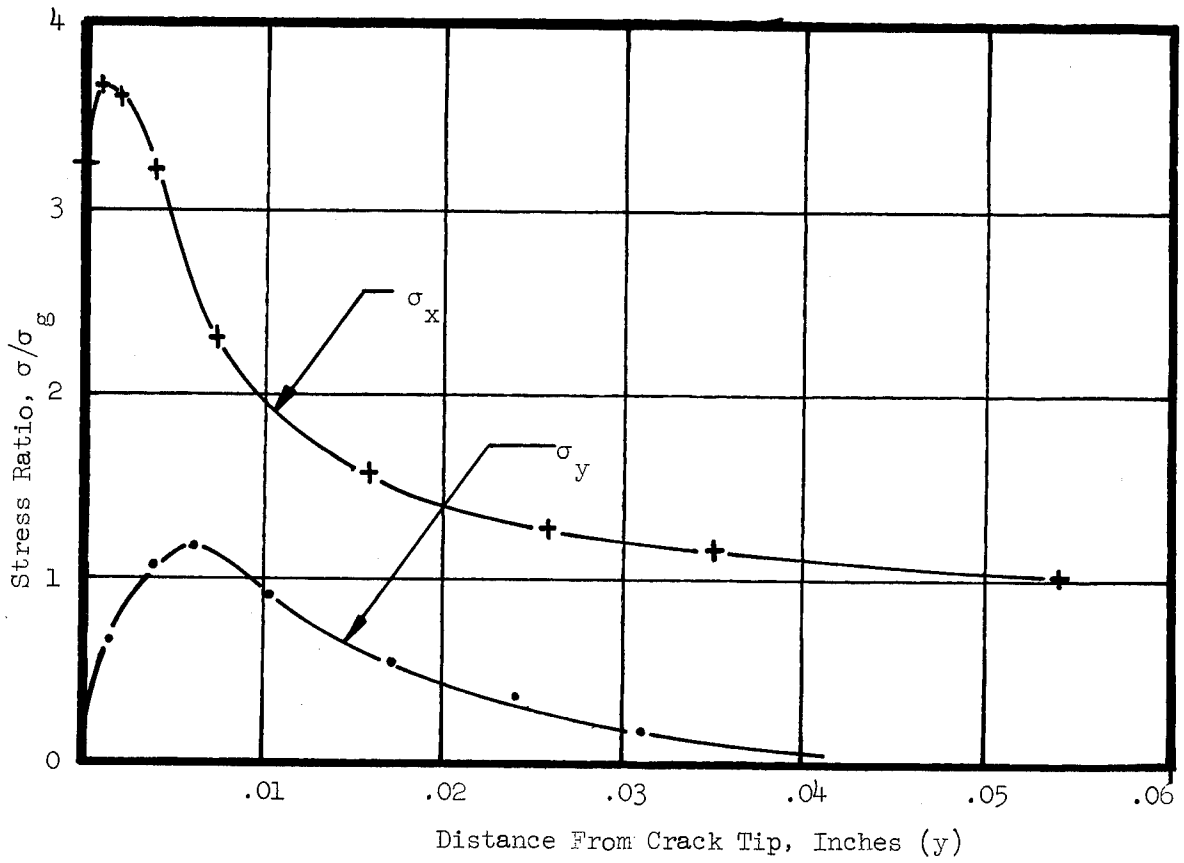

Fig. 57 Elasto-Plastic Stress Distributions, $\ell_{cr} = 0.1$, $t = 0.3$, $z = .15$ and $\sigma_g/\sigma_1 = .248$

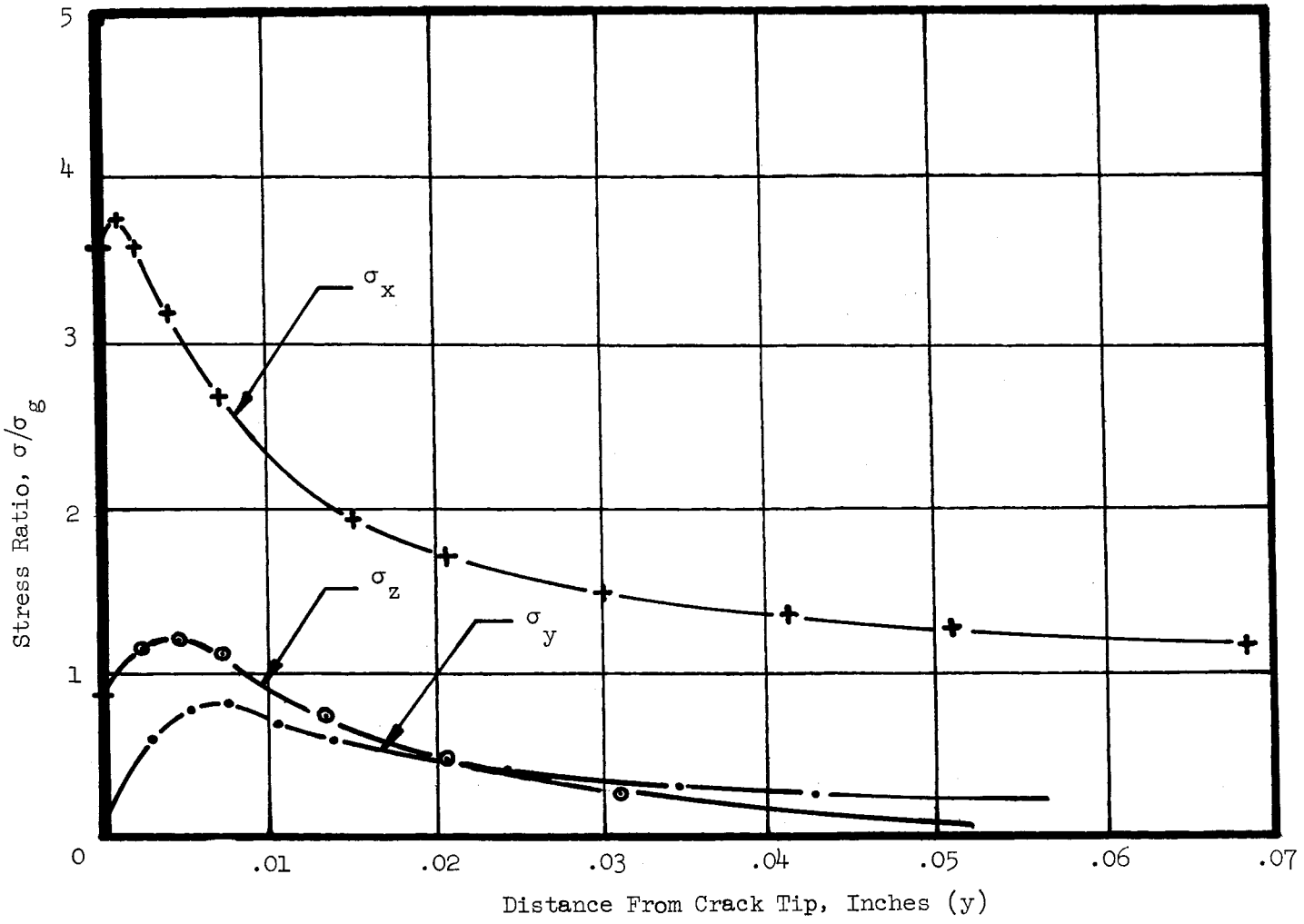

Fig. 58 Elasto-Plastic Stress Distributions, ℓ_{cr} = 0.1, t = 0.5, z = 0, and σ_g/σ_1 = .158

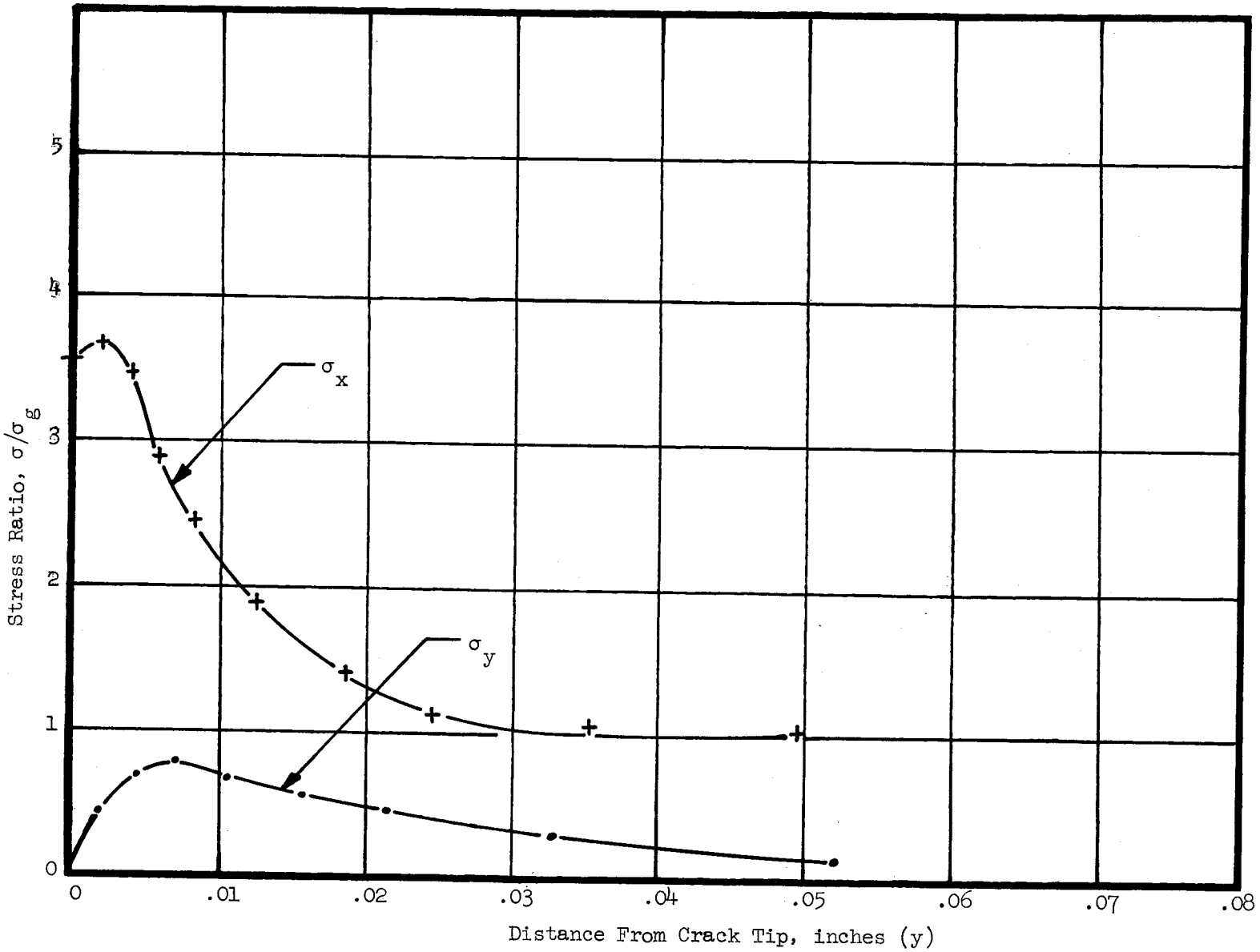

Fig. 59 Elasto-Plastic Stress Distributions, $\ell_{cr} = 0.1$, $t = 0.5$, $z = .25$, and $\sigma_g/\sigma_1 = .158$

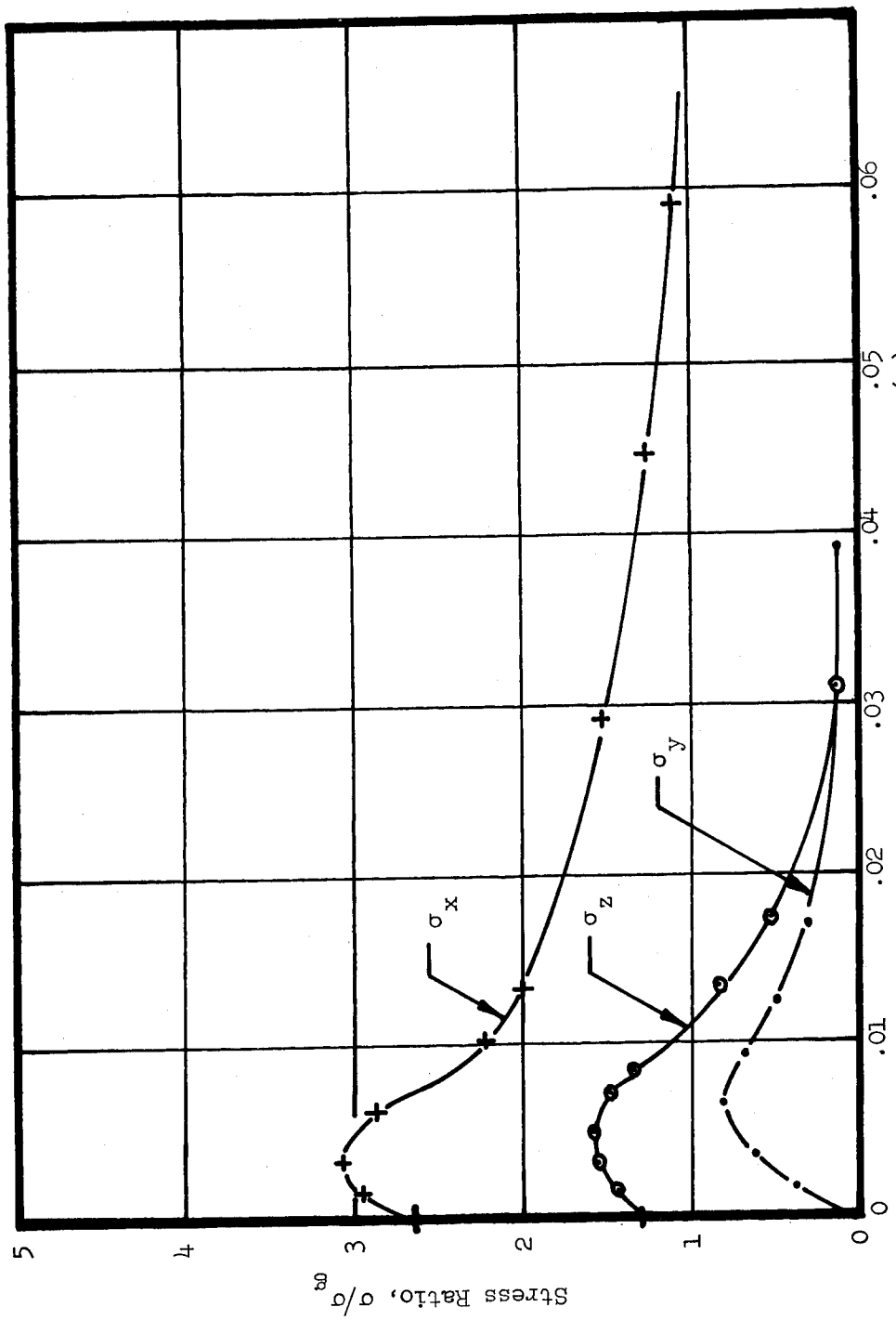

Fig. 60 Elasto-Plastic Stress Distributions, ℓ_{cr} =0.1, t =0.5, z = 0, and σ_g/σ_1 = .240

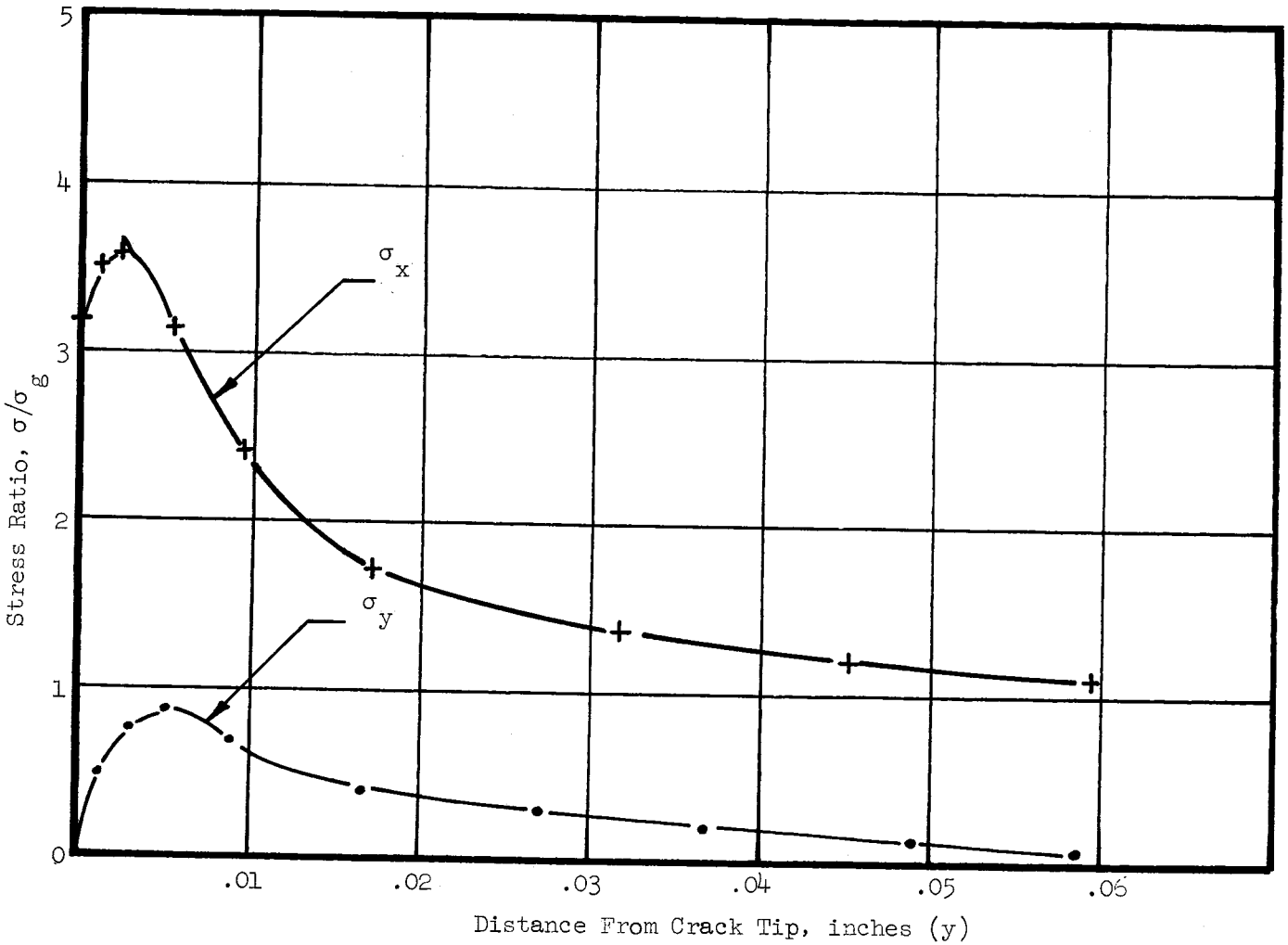

Fig. 61 Elasto-Plastic Stress Distributions, ℓ_{cr}=0.1, t =0.5, z = .25, and σ_g/σ_1 = .240

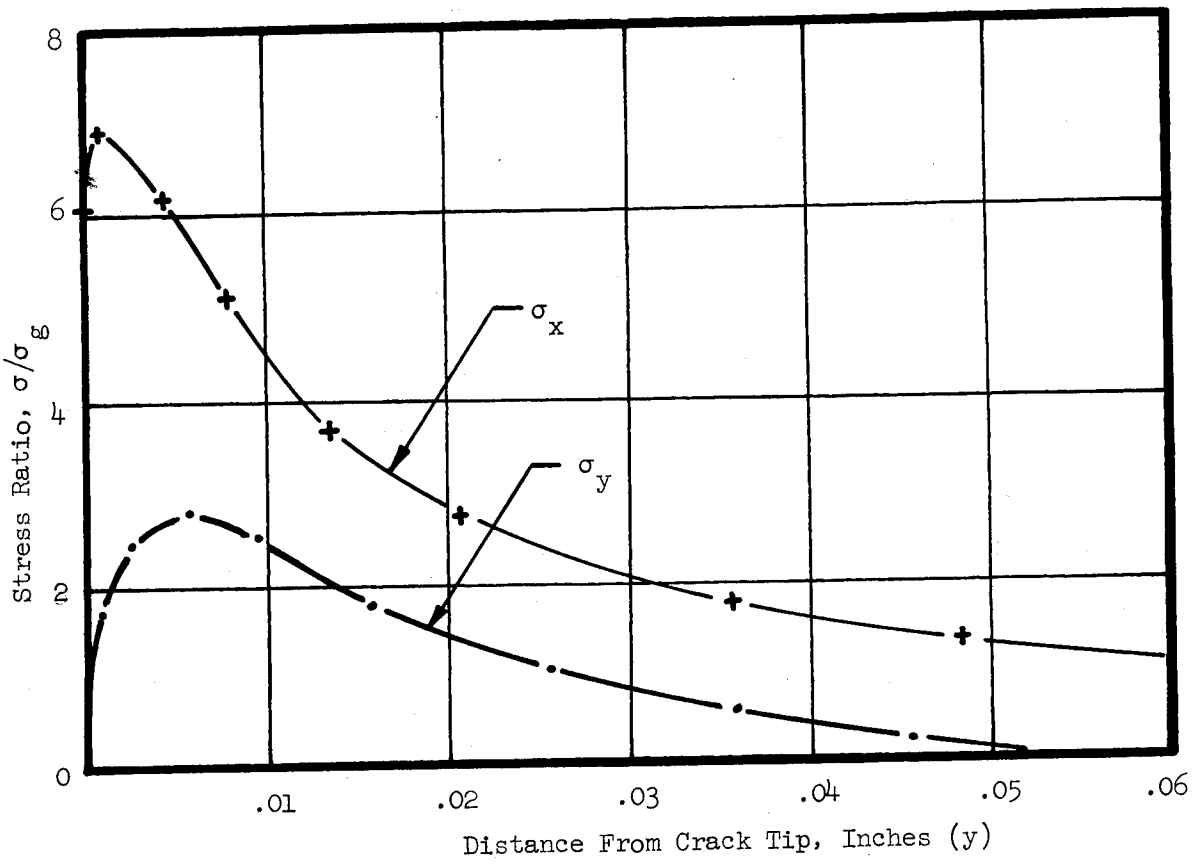

Fig. 62 Elasto-Plastic Stress Distribution, ℓ_{cr} = .05, t = 0.1, z = 0, and σ_g/σ_1 = .209

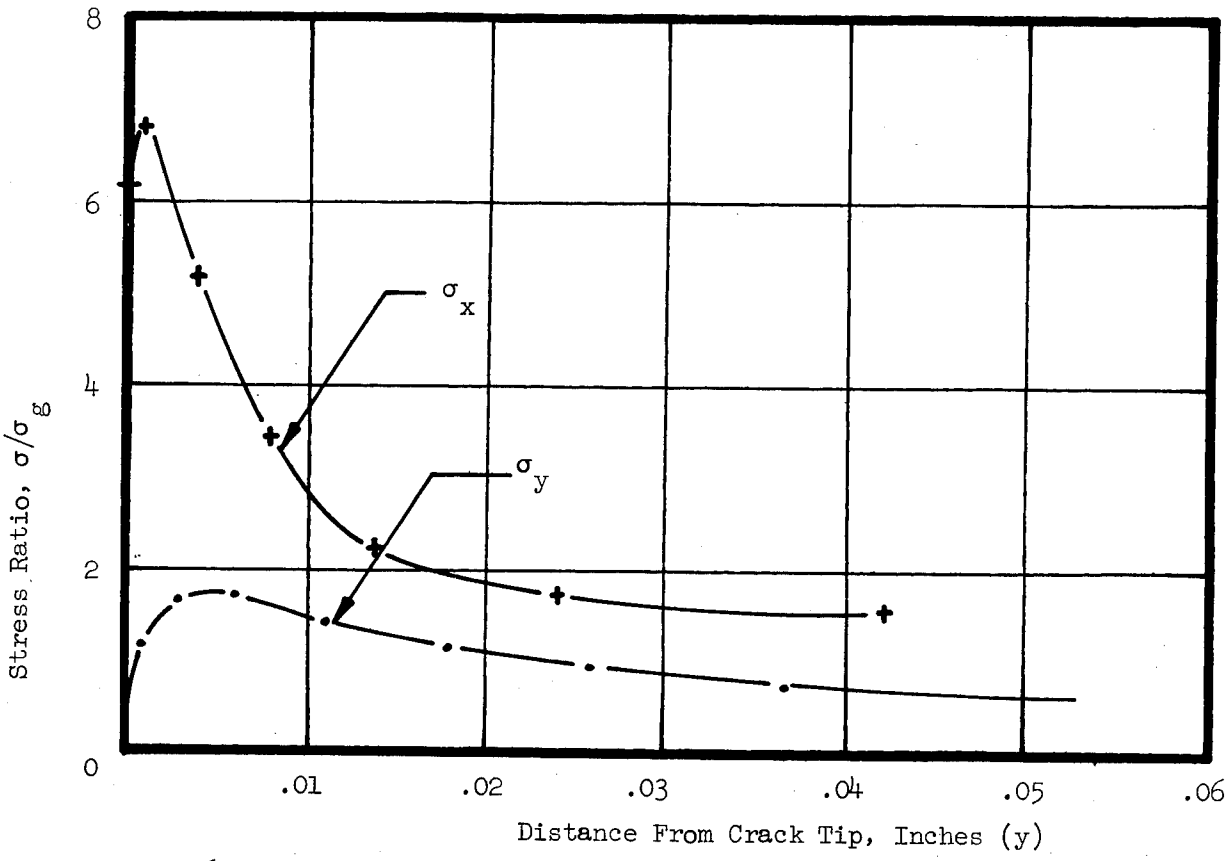

Fig. 63 Elasto-Plastic Stress Distribution, ℓ_{cr} = 0.5, t = 0.1, z = .05

σ_g/σ_1 = .209

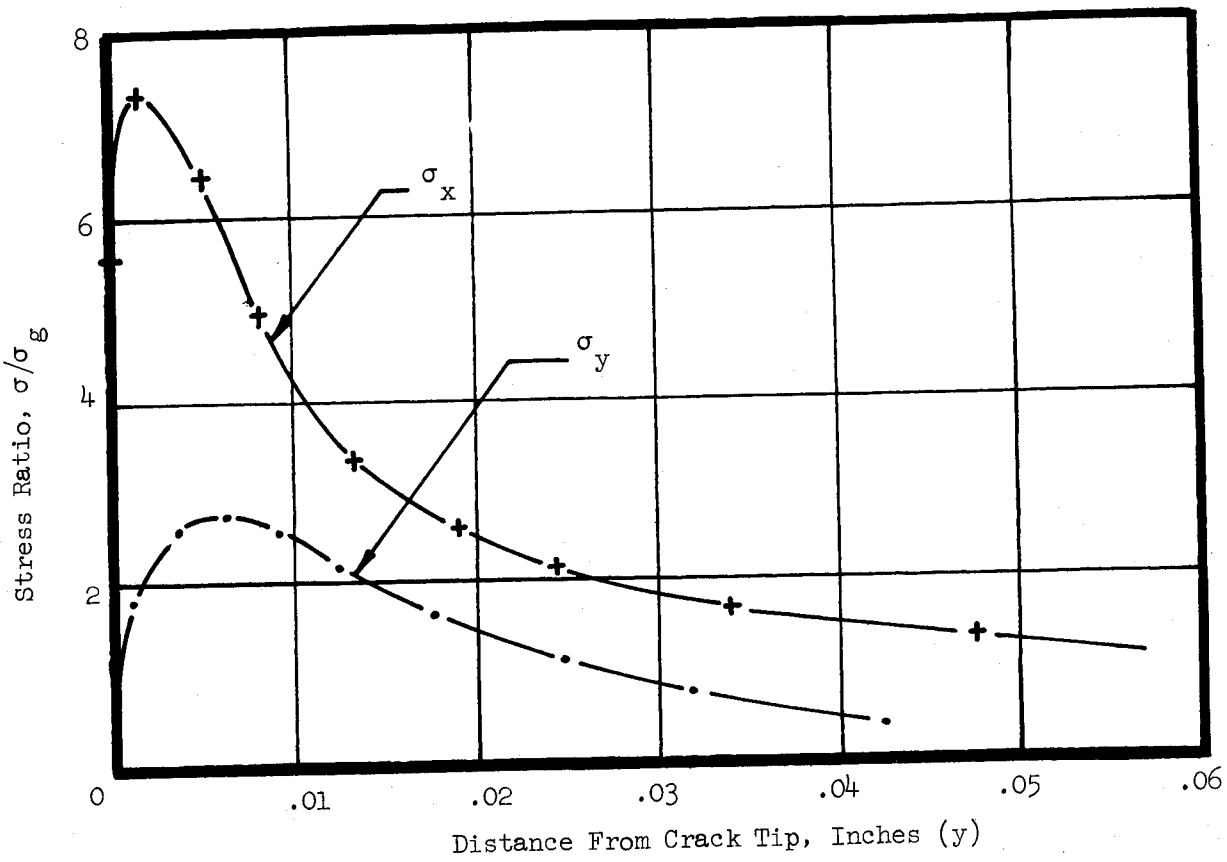

Fig. 64 Elasto-Plastic Stress Distributions, $\ell_{cr} = 0.5$, t = 0.1, z = 0, and $\sigma_g/\sigma_1 = .280$

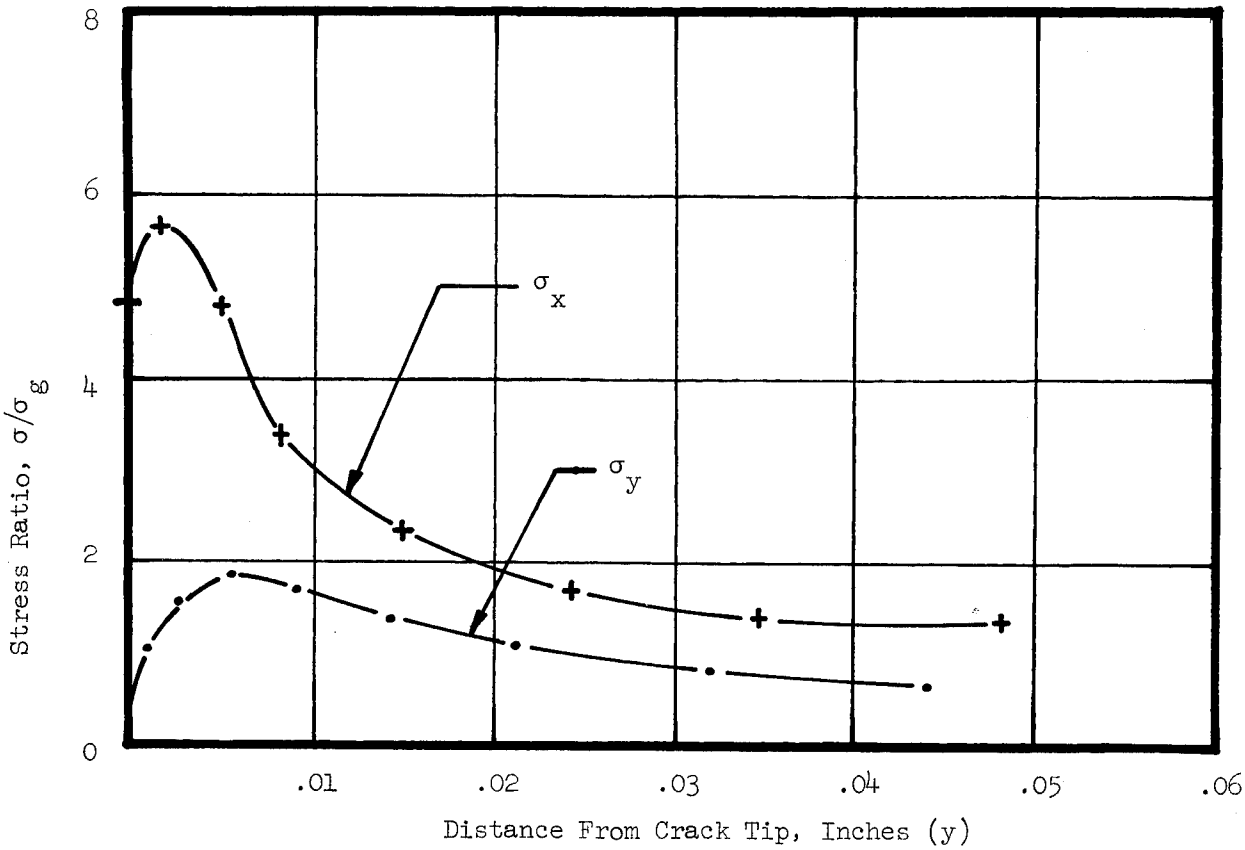

Fig. 65 Elasto-Plastic Stress Distributions, $\ell_{cr} = 0.5$, t = 0.1, z = 0.05, and $\sigma_g/\sigma_1 = .280$

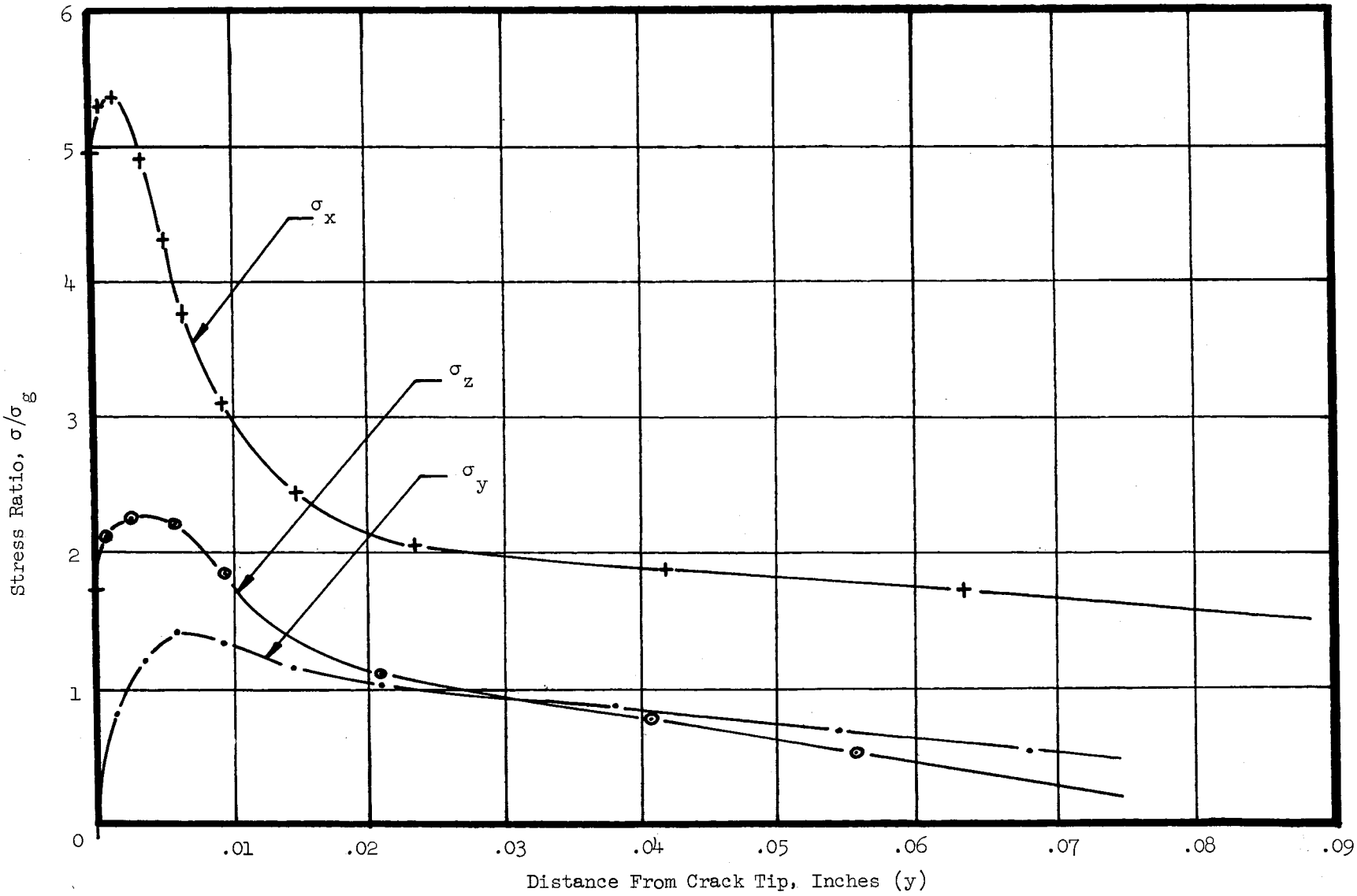

Fig. 66 Elasto-Plastic Stress Distribution, $\ell_{cr} = 0.5$, $t = 0.3$, $z = 0$, and $\sigma_g/\sigma_1 = .280$

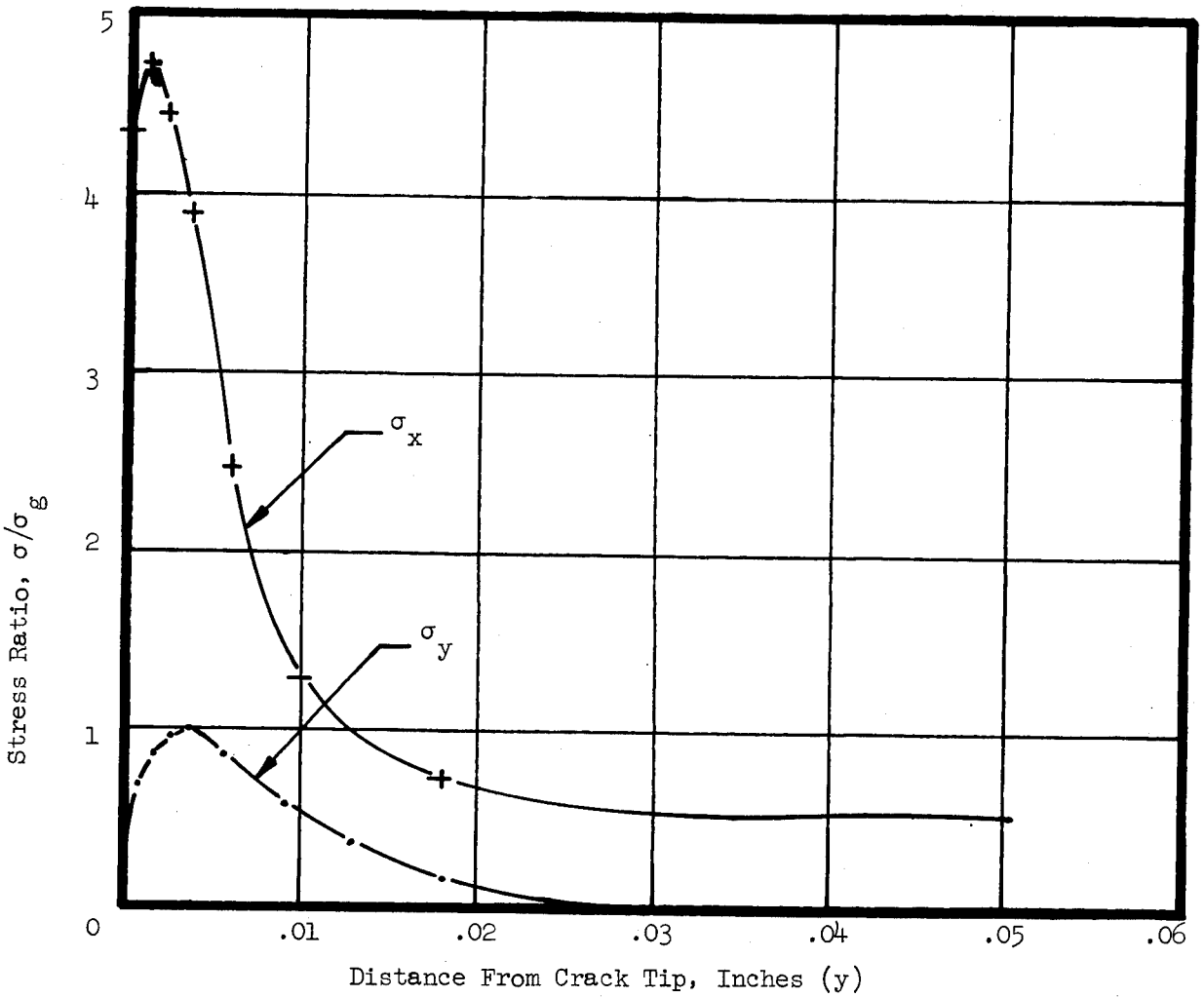

Fig. 67 Elasto-Plastic Stress Distributions, ℓ_{cr} =0.5, t =0.3, z = .15, and σ_g/σ_1= .280

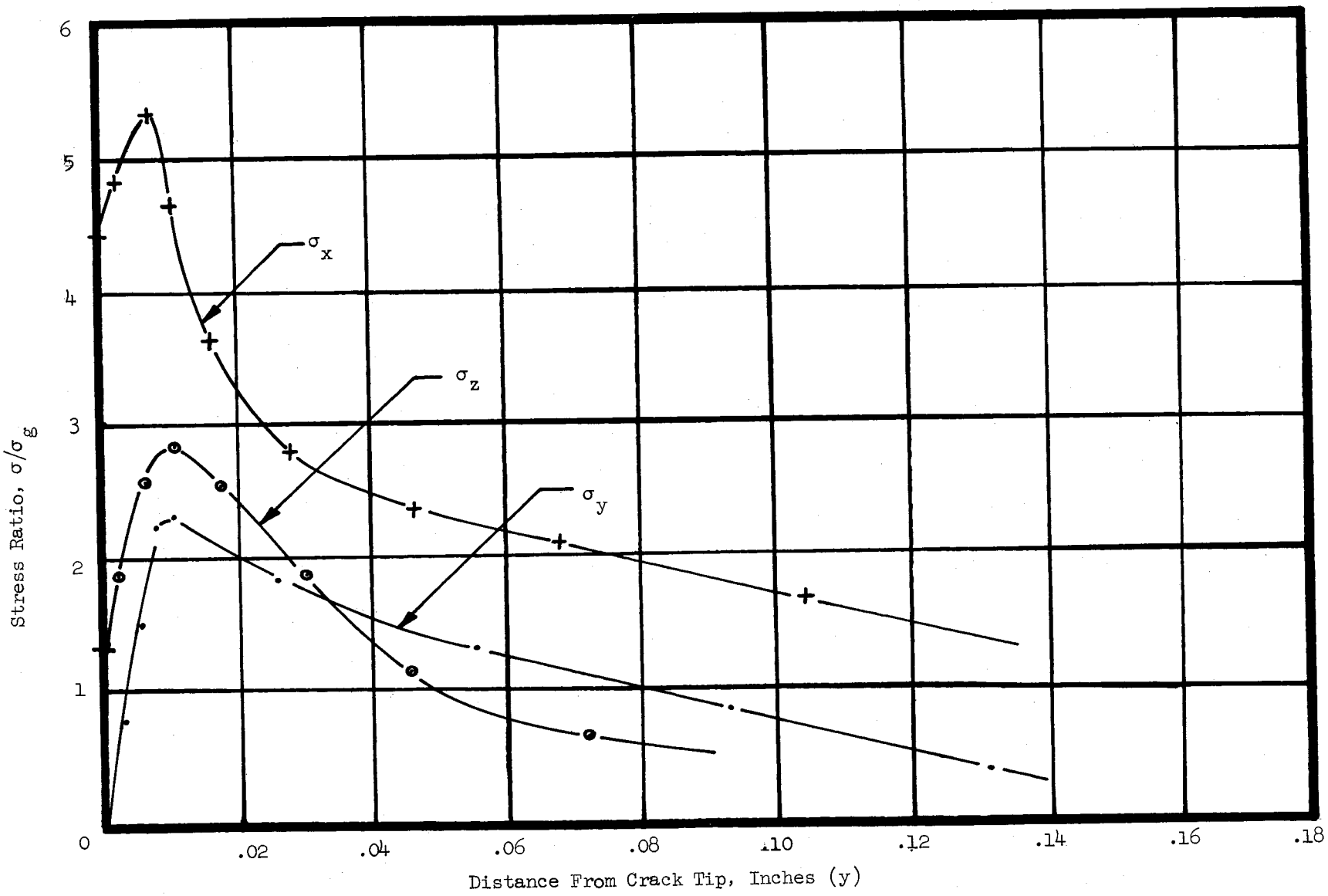

Fig. 68 Elasto-Plastic Stress Distribution, ℓ_{cr} =0.5, t =0.3, z = 0, and σ_g/σ_1 = .354

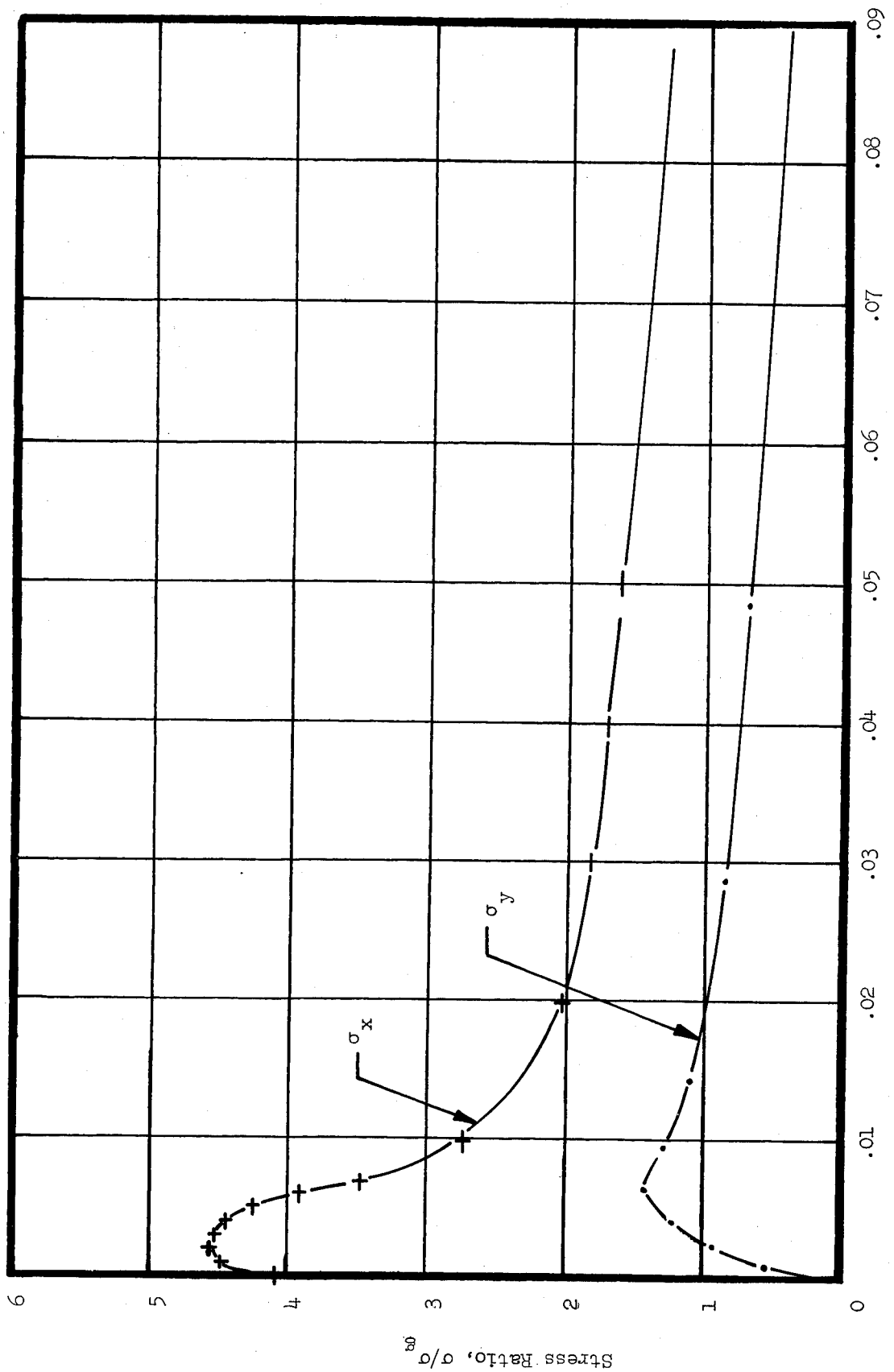

Fig. 69 Elasto-Plastic Stress Distribution, ℓ_{cr} = 0.5, t =0.3, z = .15, and σ_g/σ_1 = .354

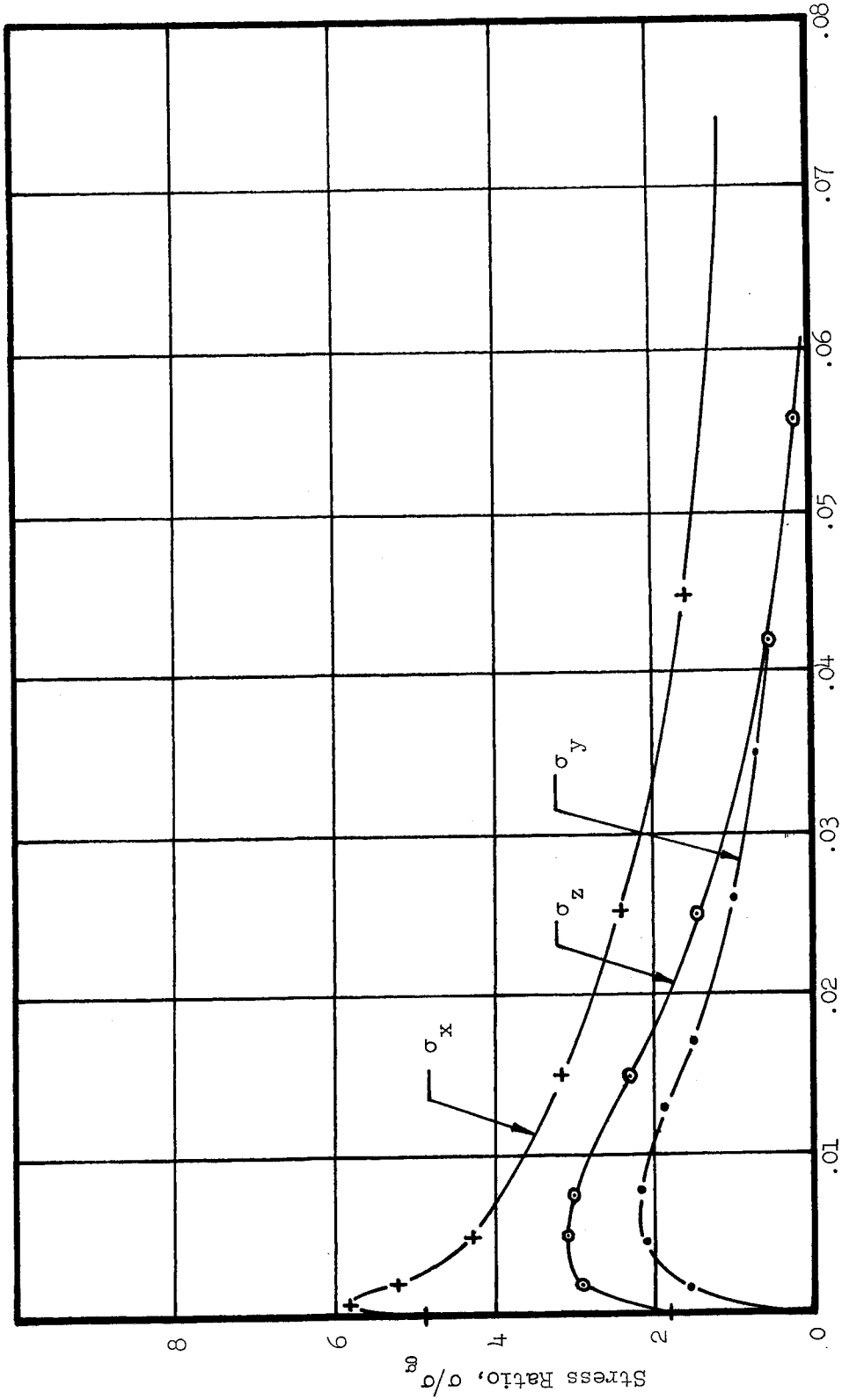

Fig. 70 Elasto-Plastic Stress Distribution, ℓ_{cr} = 0.5", t = 0.5, z = 0, and σ_g/σ_1 = .209

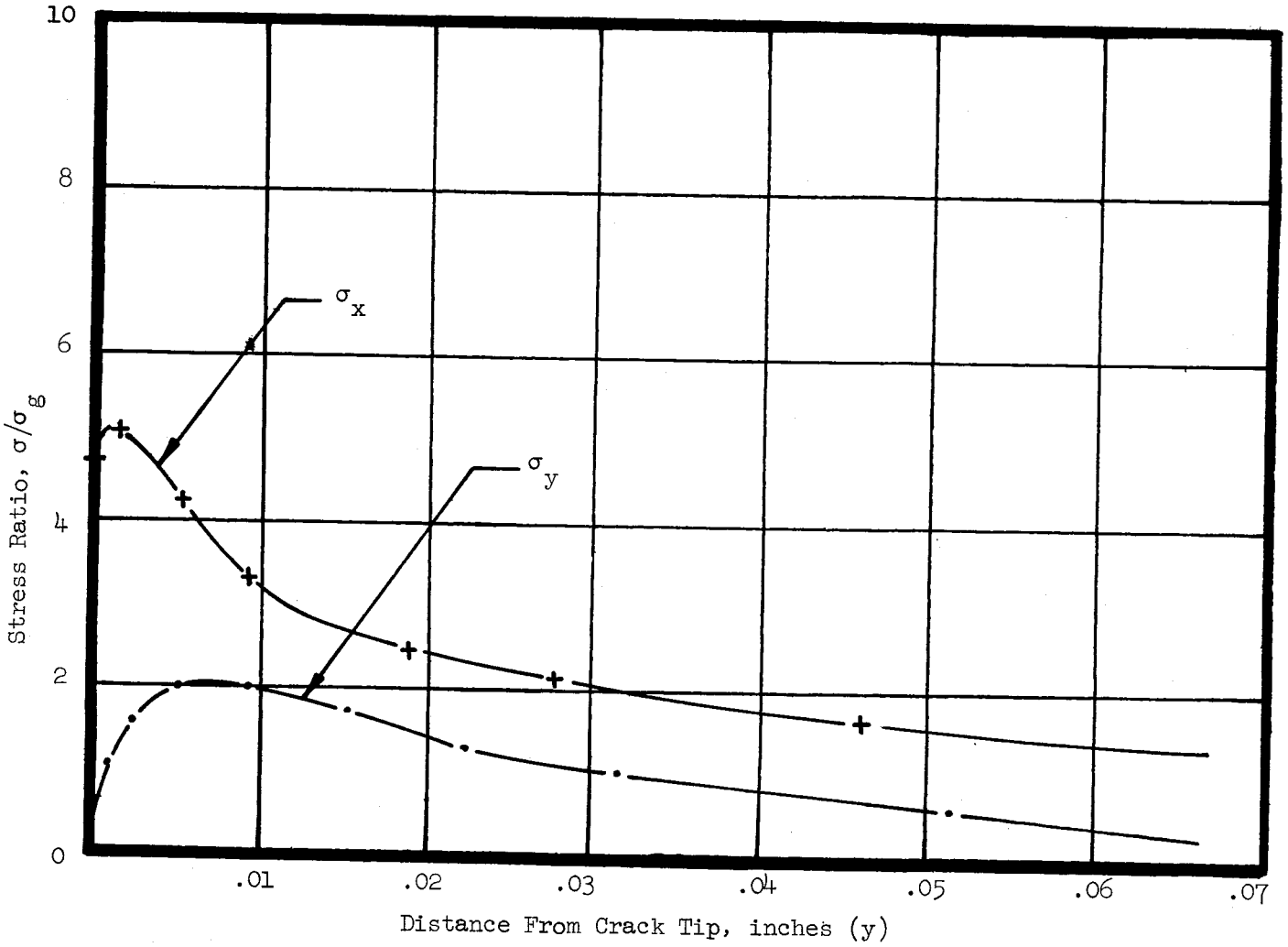

Fig. 71 Elasto-Plastic Stress Distribution, ℓ_{cr} =0.5, t =0.5, z = .25, and σ_g/σ_1 = .209

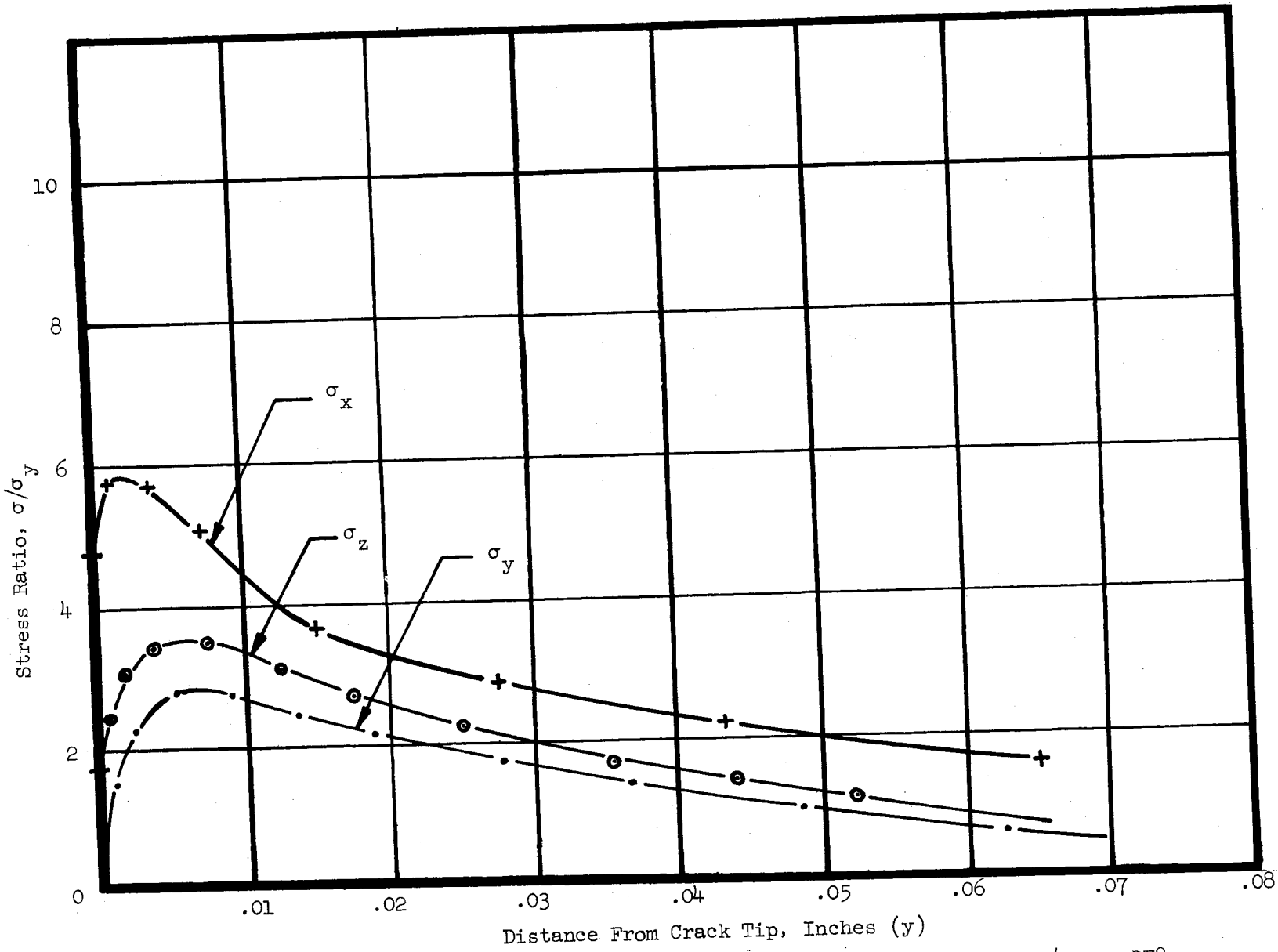

Fig. 72 Elasto-Plastic Stress Distribution, $\ell_{cr} = 0.5$, $t = 0.5$, $z = 0$, and $\sigma_g/\sigma_1 = .278$

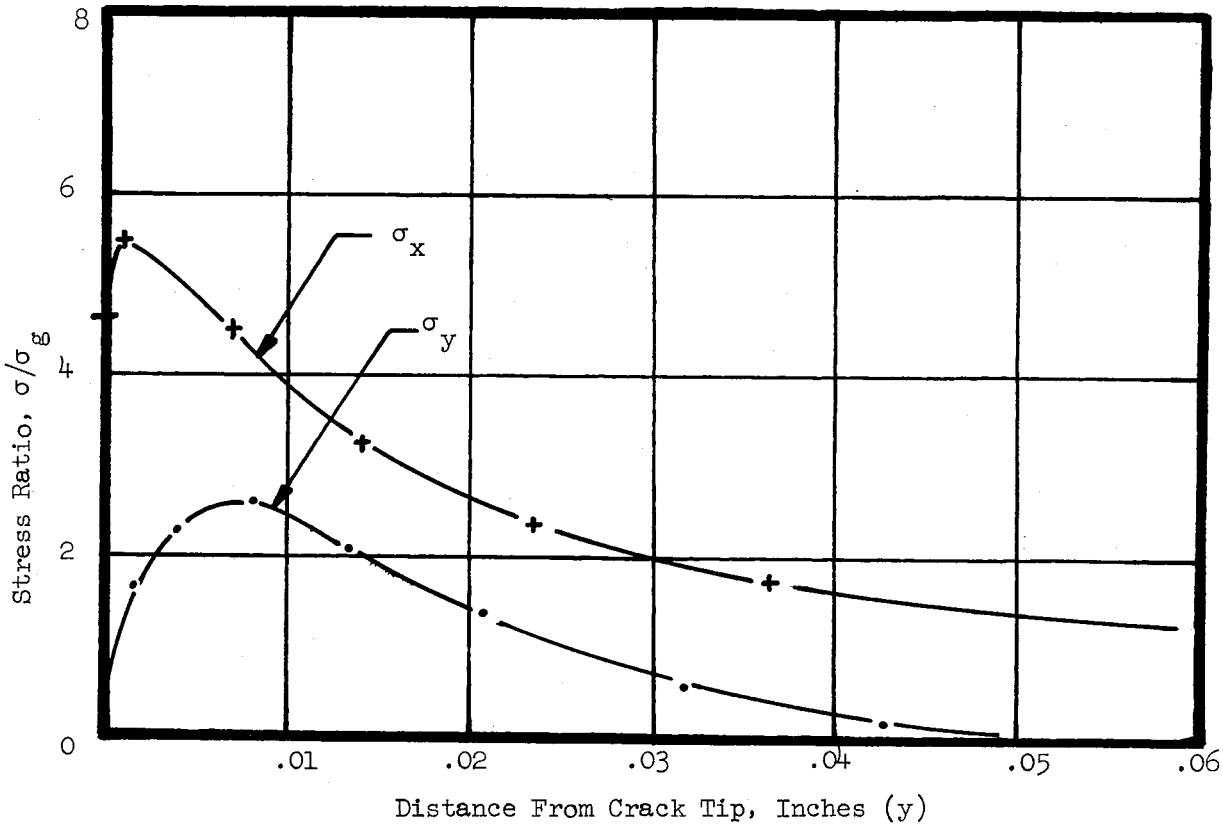

Fig. 73 Elasto-Plastic Stress Distribution, $\ell_{cr} = 0.5$, t = 0.5, z = .25, and $\sigma_g/\sigma_1 = .278$

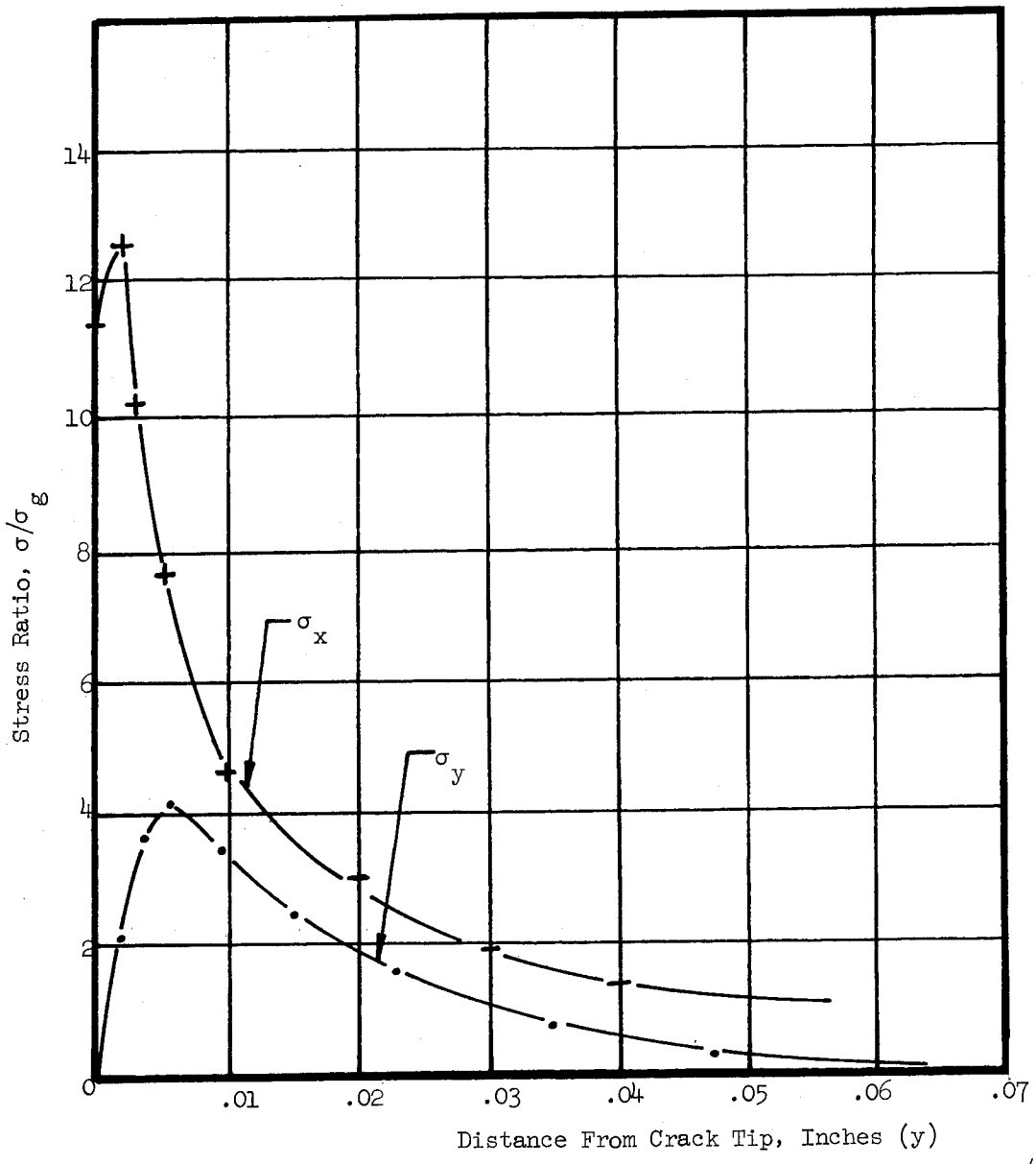

Fig. 74 Elasto-Plastic Stress Distributions, ℓ_{cr} =0.8, t =0.1, z = 0, and σ_g/σ_1 = .095

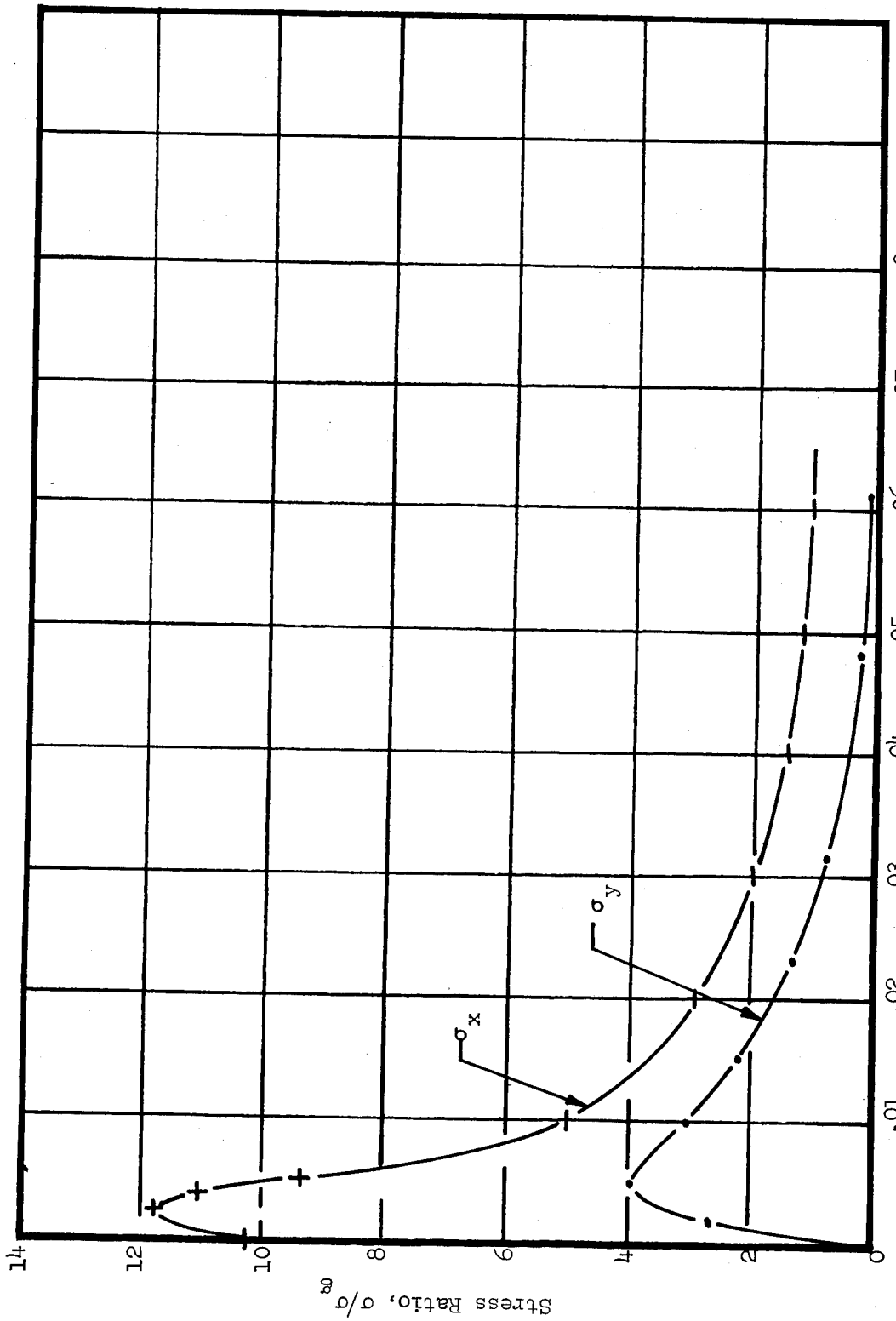

Fig. 75 Elasto-Plastic Stress Distributions, ℓ_{cr} =0.8, t = 0.1, z = .05, and σ_g/σ_1 = .095

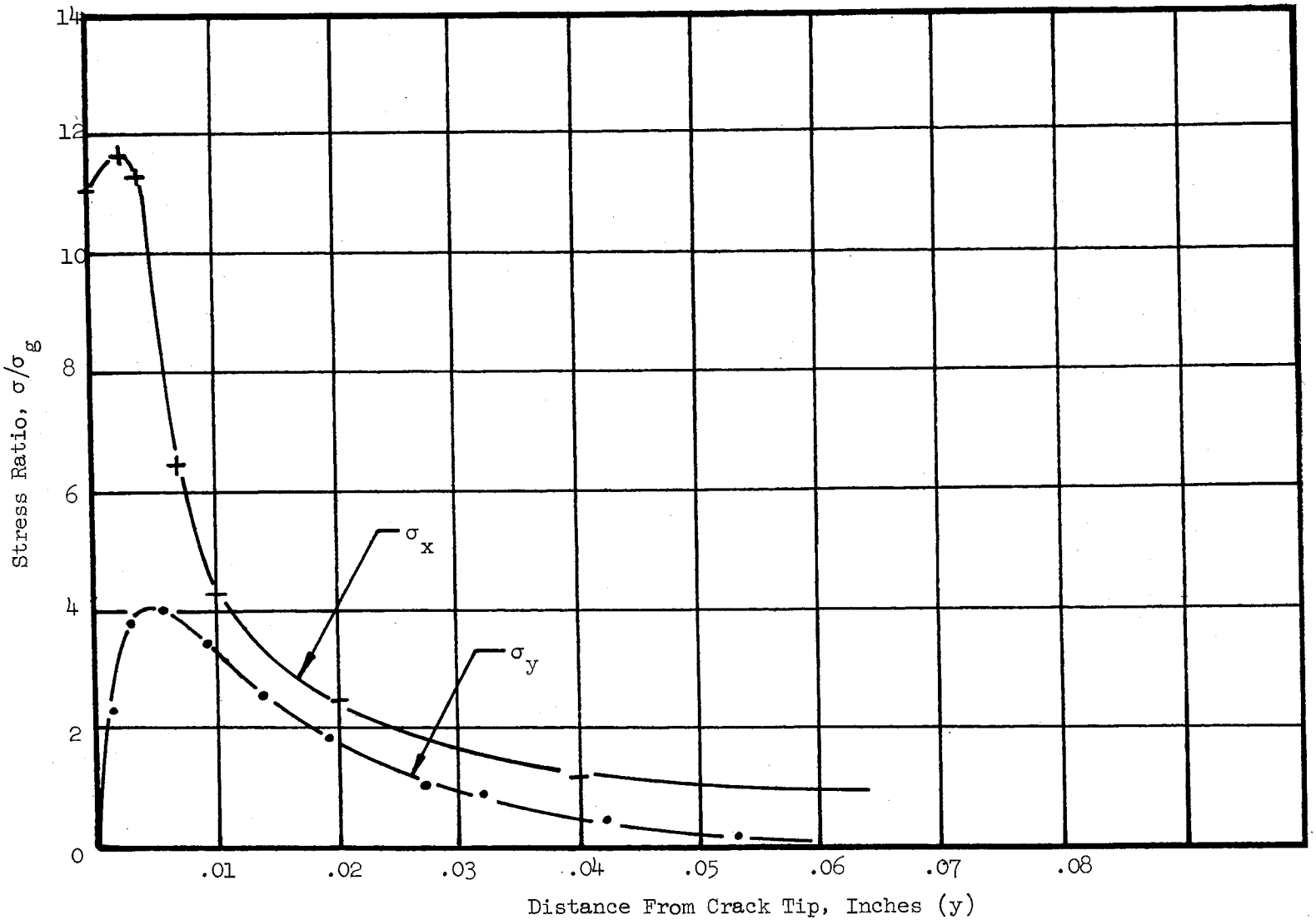

Fig. 76 Elasto-Plastic Stress Distributions, ℓ_{cr} =0.8, t =0.1, z = 0, and σ_g/σ_1 = .126

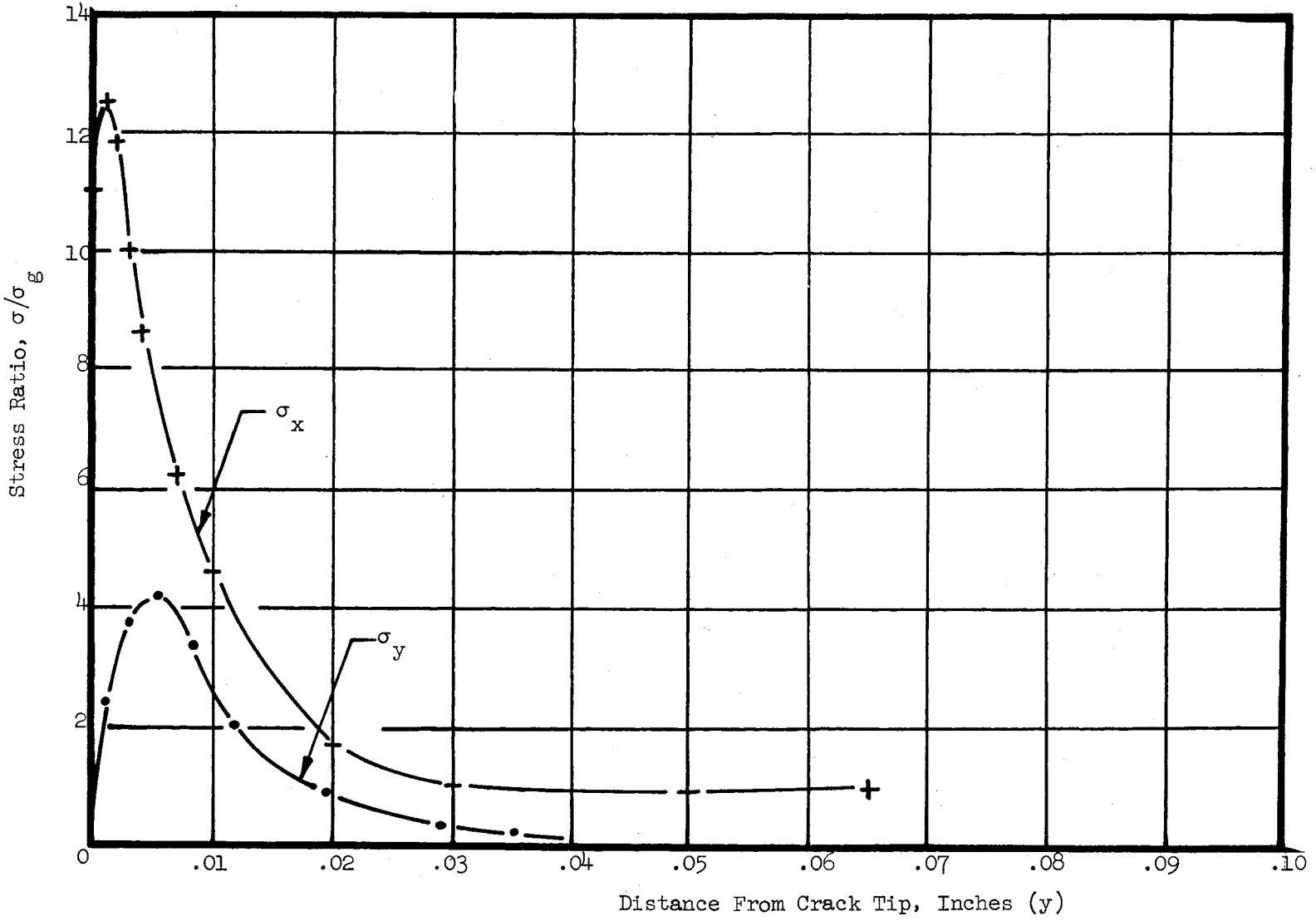

Fig. 77 Elasto-Plastic Stress Distributions, ℓ_{cr} = 0.8, t = 0.1, z = .05, and σ_g/σ_1 = .126

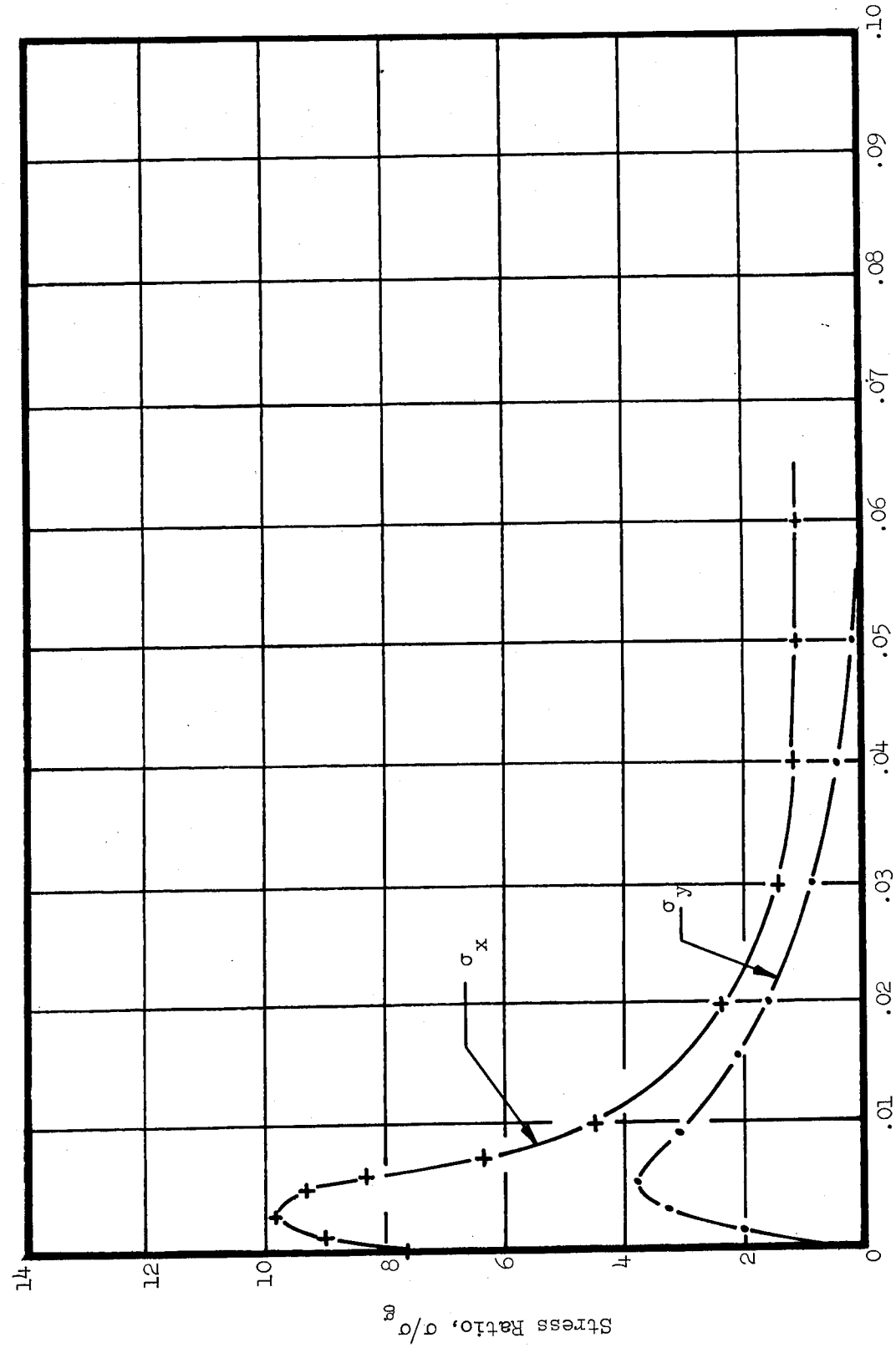

Fig. 78 Elasto-Plastic Stress Distributions, $\ell_{cr} = 0.8$, $t = 0.1$, $z = 0$, and $\sigma_g/\sigma_1 = .190$

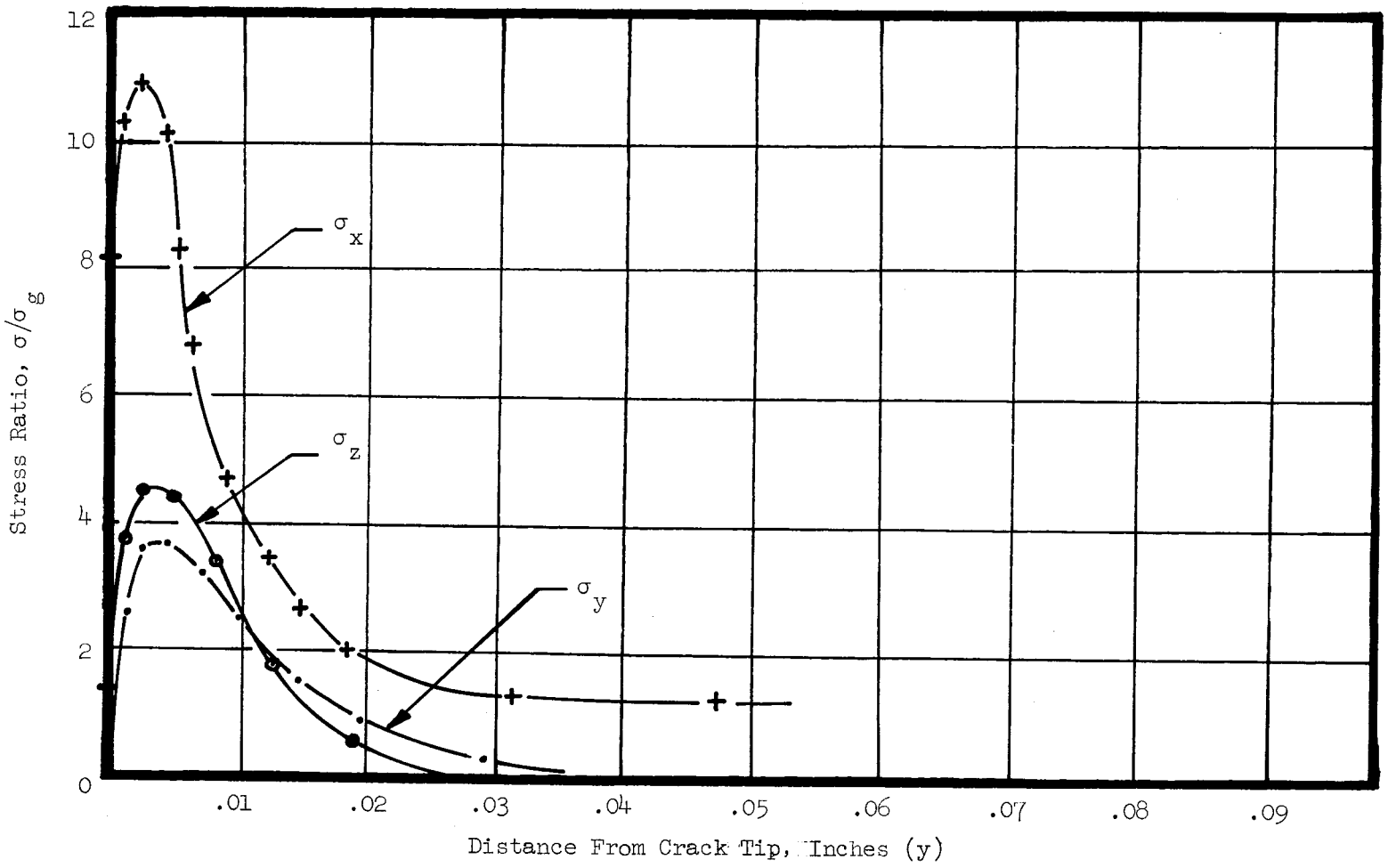

Fig. 79 Elasto-Plastic Stress Distributions, ℓ_{cr} = 0.8, t = 0.3, z = 0, and σ_g/σ_1 = .126

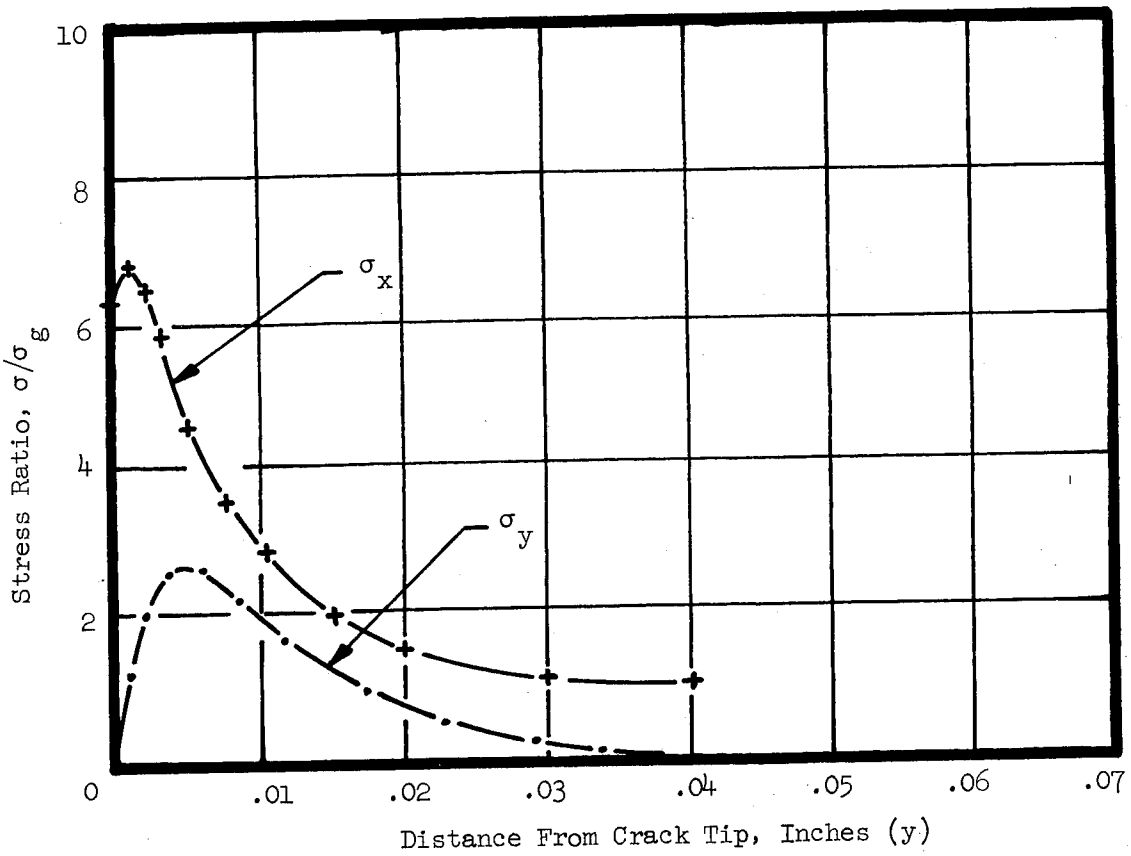

Fig. 80 Elasto-Plastic Stress Distributions, $\ell_{cr} = 0.8$, $t = 0.3$, $z = .15$, and $\sigma_g/\sigma_1 = .126$

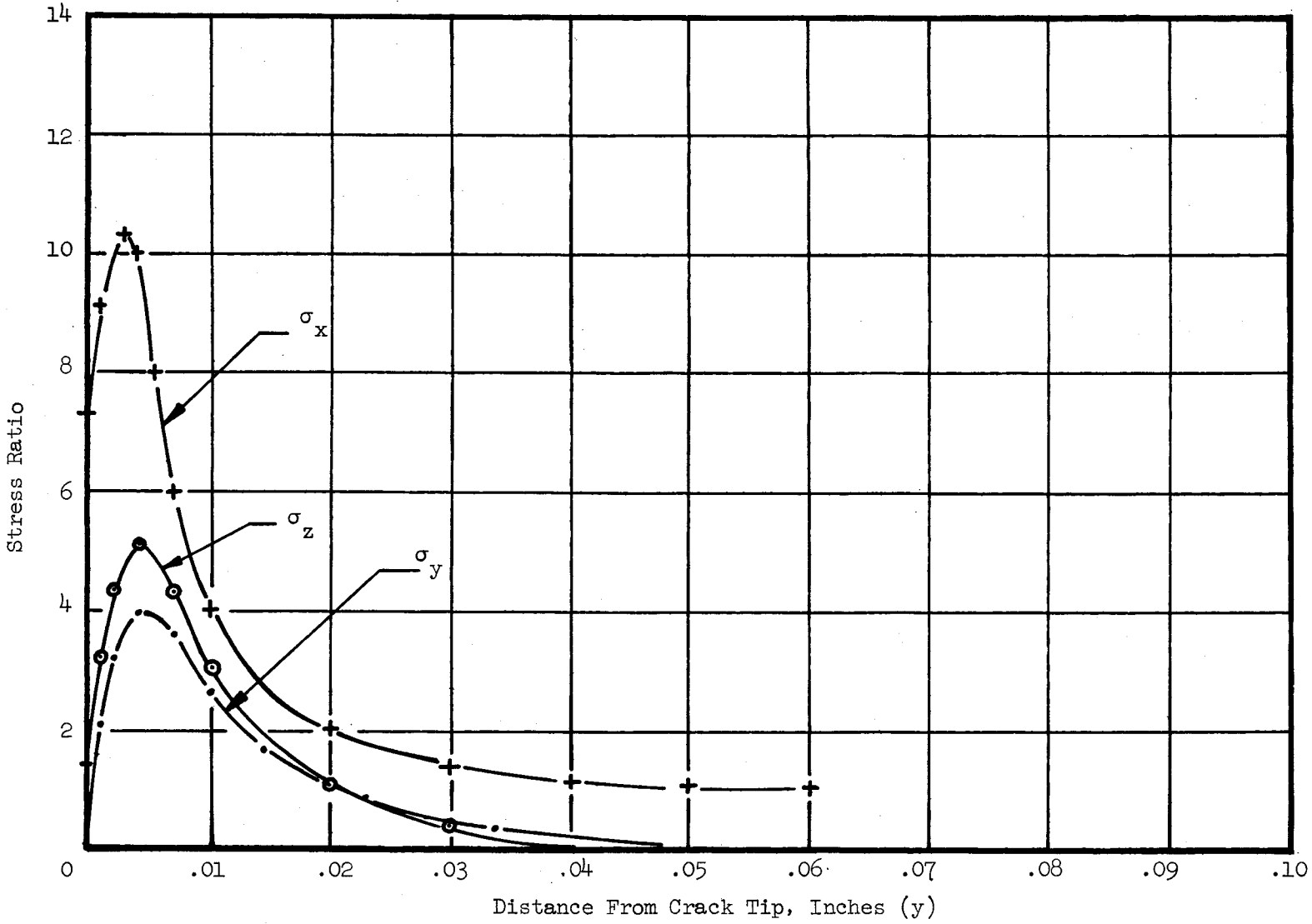

Fig. 81 Elasto-Plastic Stress Distributions, ℓ_{cr} =0.8, t =0.3, z = 0, and σ_g/σ_1 = .19

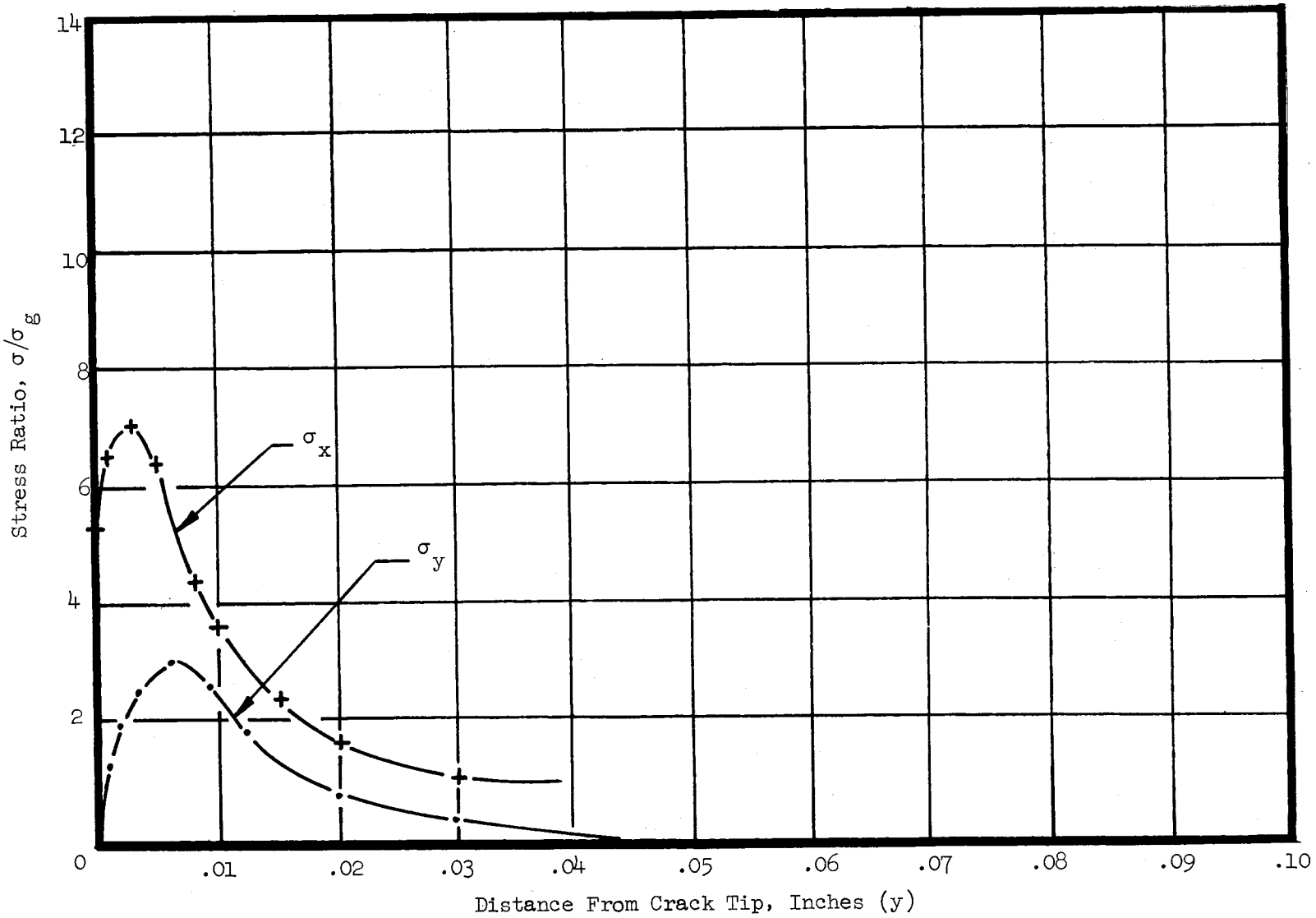

Fig. 82 Elasto-Plastic Stress Distributions, ℓ_{cr} =0.8, t =0.3, z = .15, and σ_g/σ_1 = .190

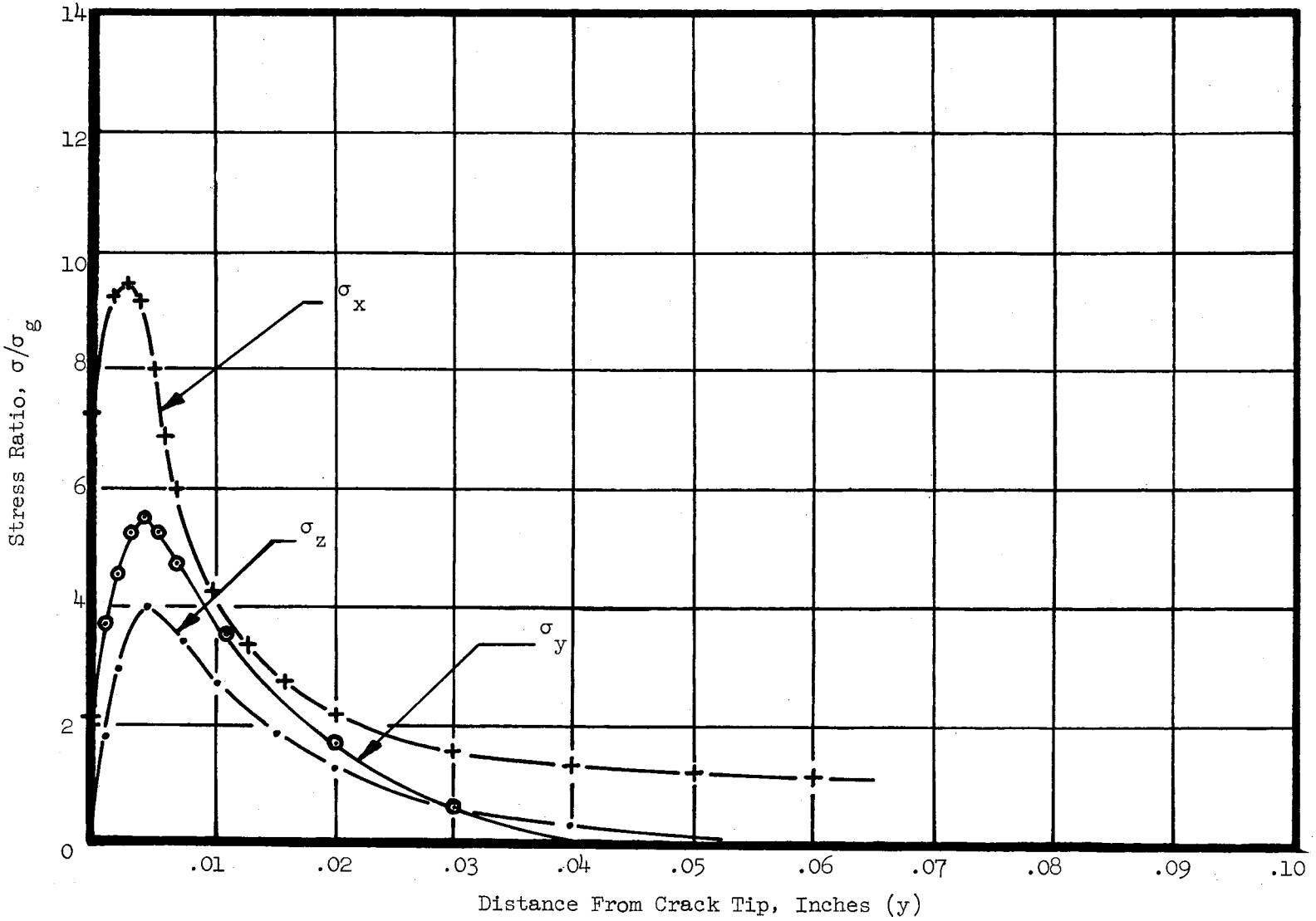

Fig. 83 Elasto-Plastic Stress Distributions, ℓ_{cr} =0.8, t =0.5, z = 0, and σ_g/σ_1 = .126

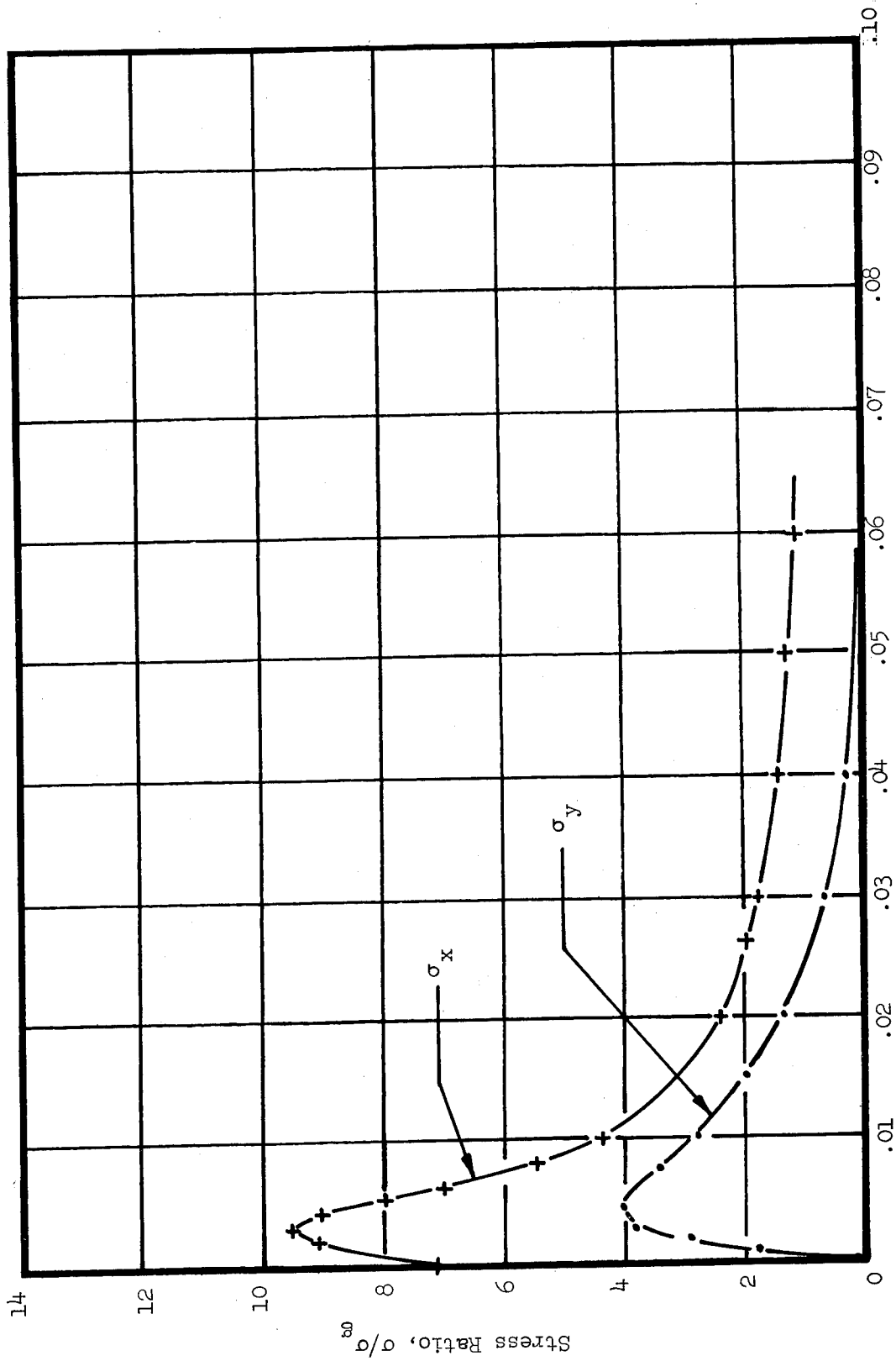

Fig. 84 Elasto-Plastic Stress Distribution, ℓ_{cr} =0.8, t =0.5, z = .25, and σ_g/σ_1 = .126

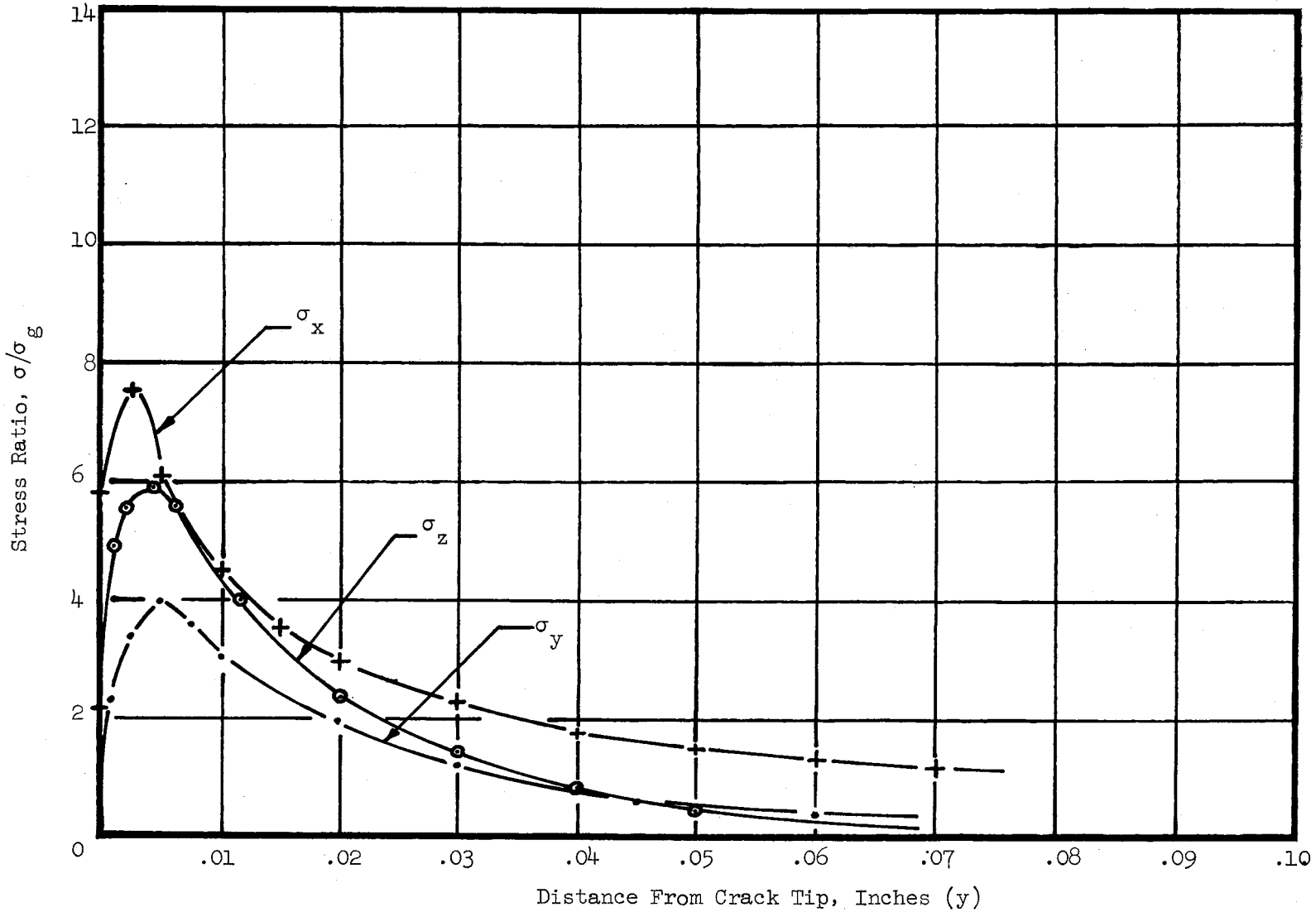

Fig. 85 Elasto-Plastic Stress Distributions, ℓ_{cr} =0.8, t =0.5, z = 0, and σ_g/σ_1 = .190

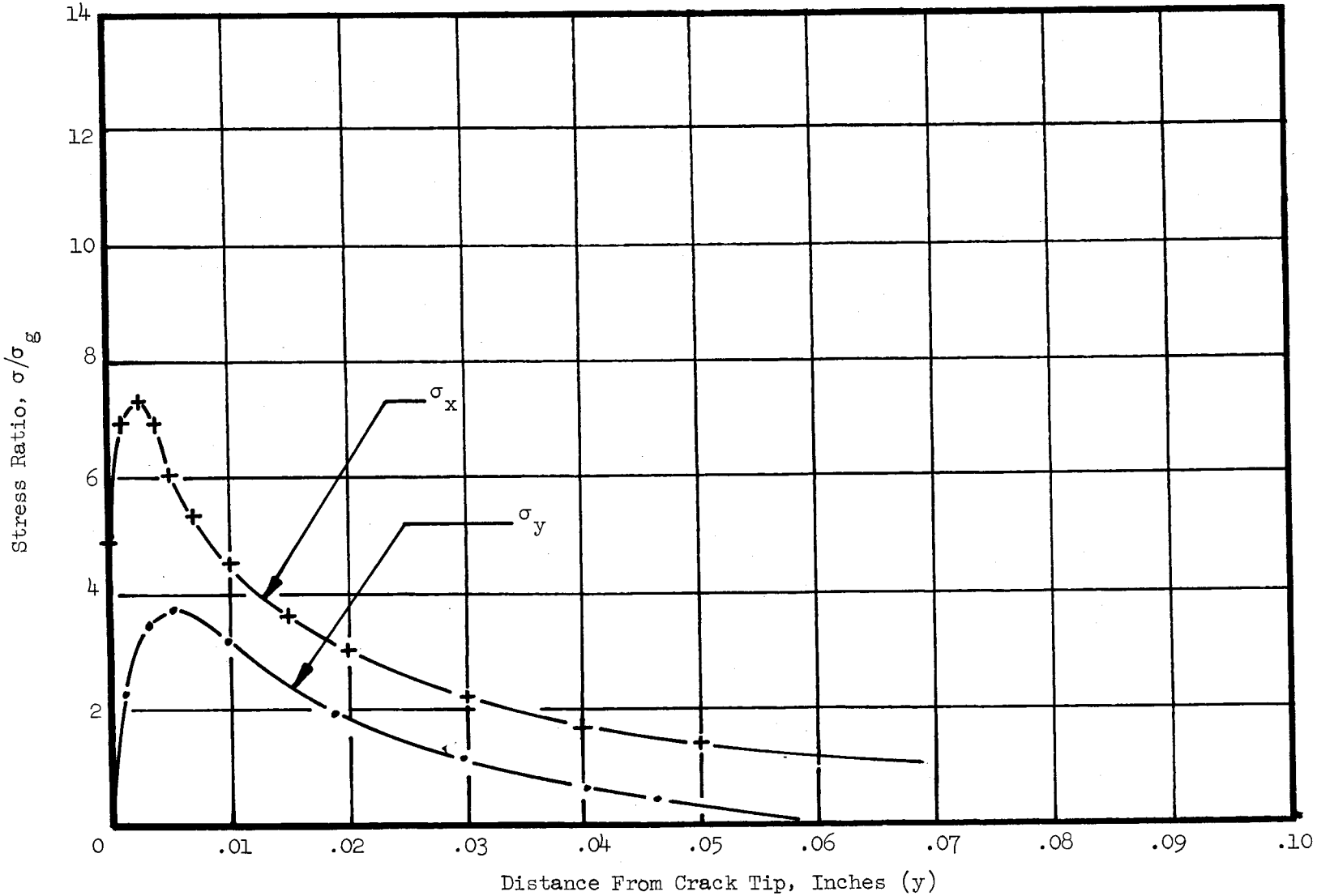

Fig. 86 Elasto-Plastic Stress Distributions, ℓ_{cr} =0.8, t =0.5, z = .25, and σ_g/σ_1 = .190

Section 6
DISCUSSION OF RESULTS (SIMULATED CRACKS)

Based on the elasto-plastic stress distributions, some general observations can be made. First it should be noted that the σ_x stress has a maximum value, not at the tip of the crack, but a short distance from the tip. This is caused by the yield condition at the edge of the crack tip being one based on a uniaxial stress (biaxial at the midplane) while at a short distance from the crack tip the yield condition depends on the biaxial stress state (tri-axial at midplane). Second, the magnitude of the maximum σ_y stress occurs at approximately 6 to 7 mils from the crack tip. The magnitude of this stress tends to be higher at the midplane than at the surface. Third, at the midplane at least for the thicker specimens, a rather high value for σ_z develops. It should also be noted that, similar to σ_x, the σ_z value is higher at a short distance from the tip of the crack than it is at the edge of the crack.

The photoelastic analysis shows stress concentration factors of 14.5 for the 0.8 in. crack length, 11 for the 0.5 in. crack length and 6.1 for 0.1 in. crack length. The elasto-plastic stress concentration factors are shown in Figs. 87 through 92. Figures 87 through 89 represent elasto-plastic stress concentration factors for the surface slices ($z = t/2$) as a function of the level of plasticity (σ_g/s_1). In these figures an attempt has been made to show the effect or lack of effect of plate thickness upon the surface stress concentration factors. These figures indicate the tendency of the stress concentration to be higher for the 0.1 in. thick plates than for the thicker plates at least for intermediate levels of plasticity. Also, the surface stress concentration factors have a tendency to become independent of plate thickness for higher levels of plasticity. For the 0.3 and 0.5 in. plate thickness, the stress concentration data is represented by the same curve. Figures 90 through 92 represent the elasto-plastic stress concentration factors for the midplanes ($z = 0$). Here a slightly different trend is observed. In general the stress concentration factors tend to be higher for the thinner

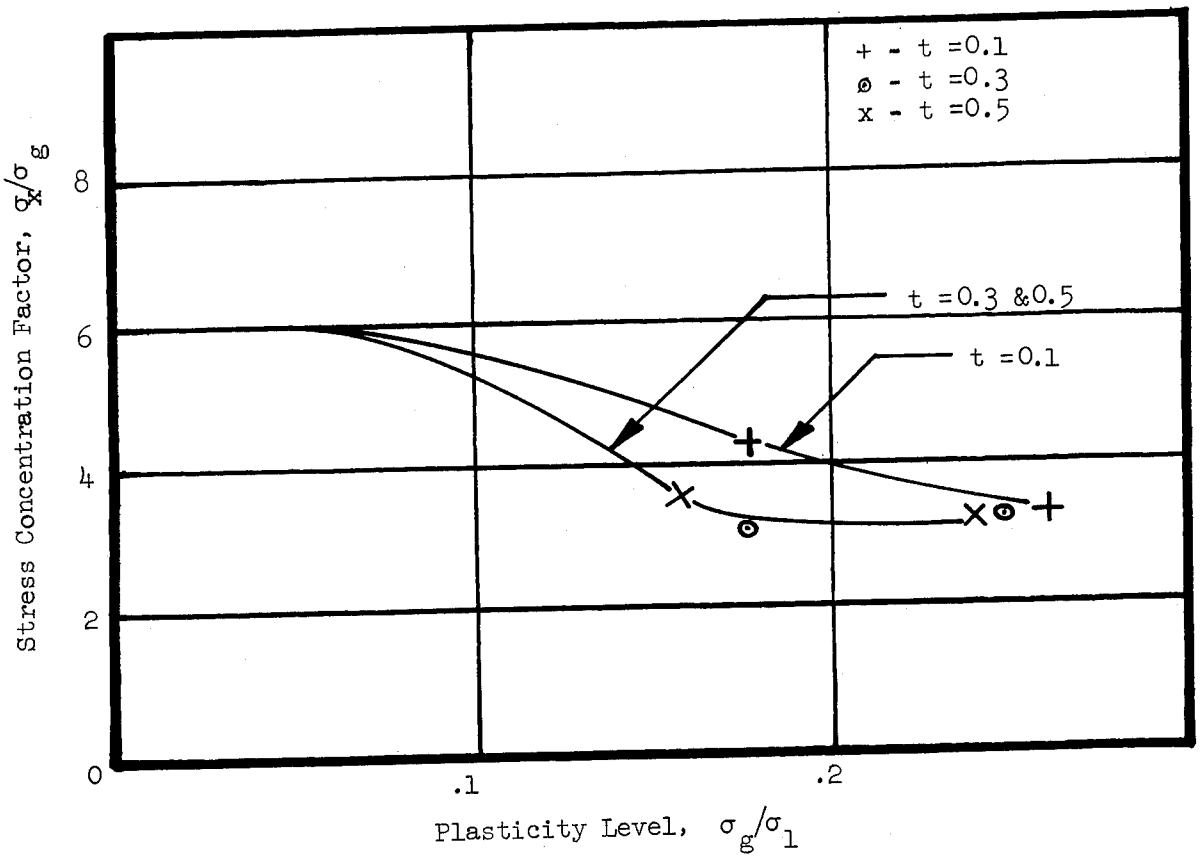

Fig. 87 Stress Concentration Factor For Various Levels of Plasticity at the Surface for $\ell_{cr} = 0.1$

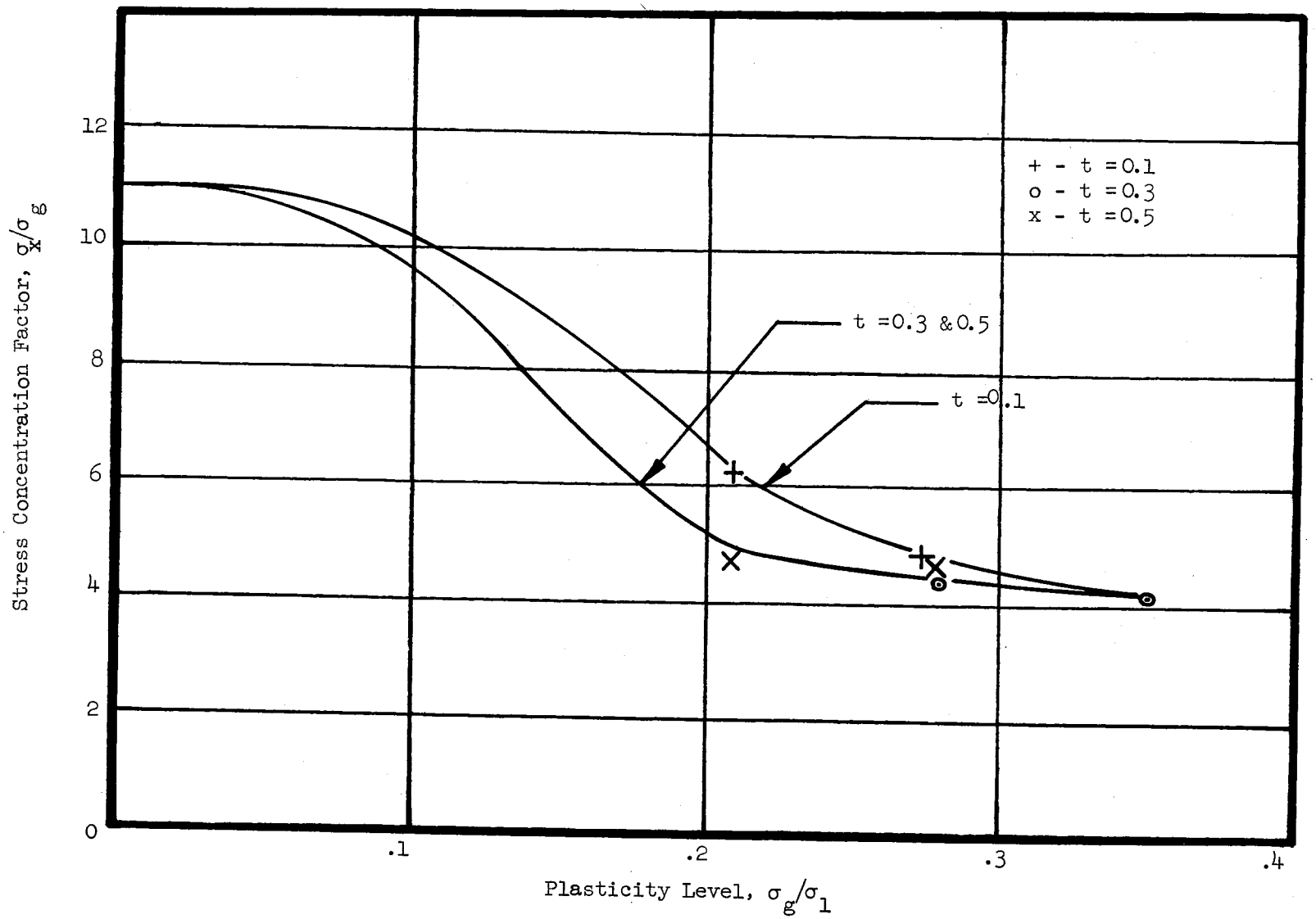

Fig. 88 Stress Concentration Factors For Various Levels of Plasticity at the Surface for $\ell_{cr} = 0.5$

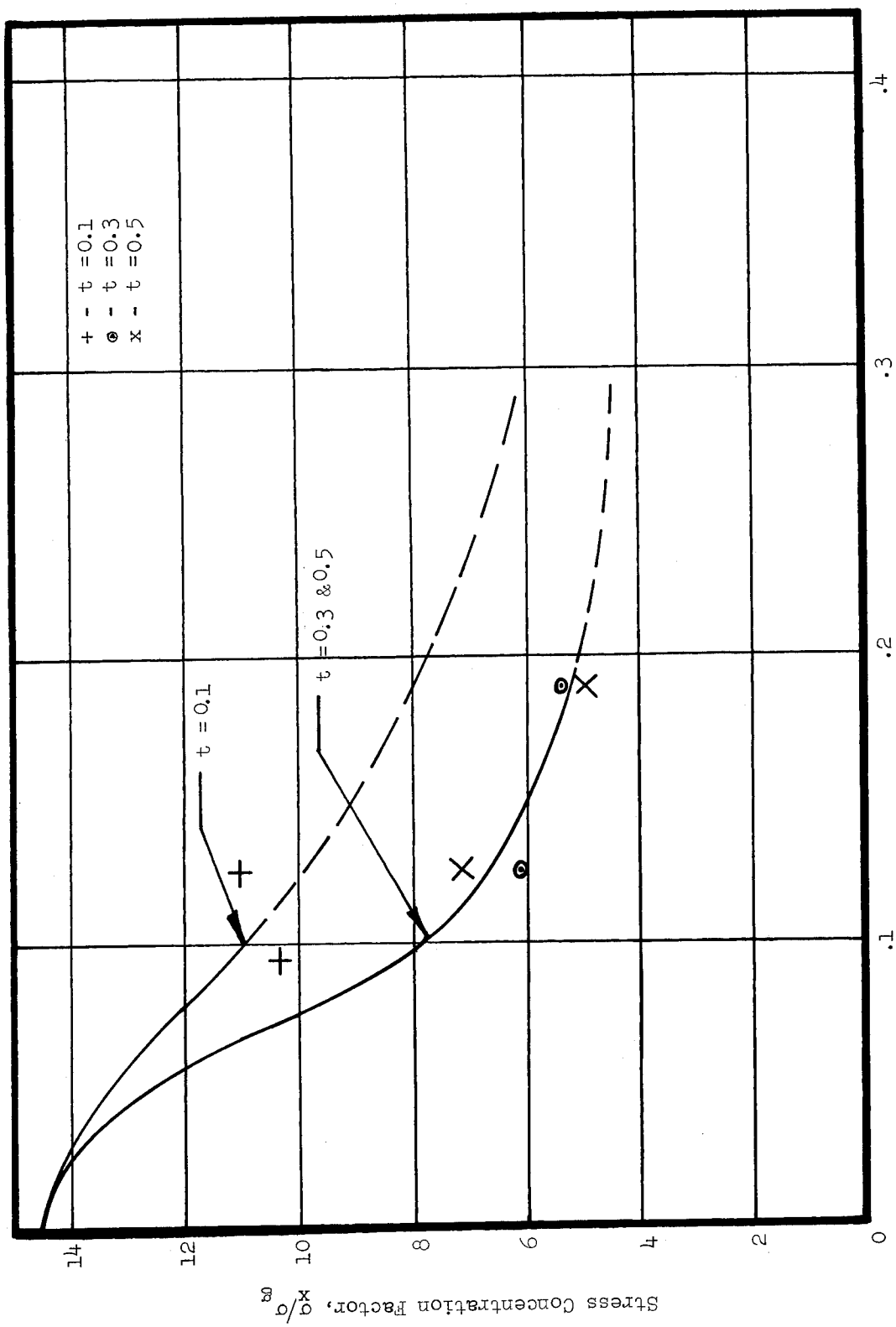

Fig. 89 Stress Concentration Factors at the Surface For Various Levels of Plasticity
$\dot{\ell}_{cr} = 0.8$

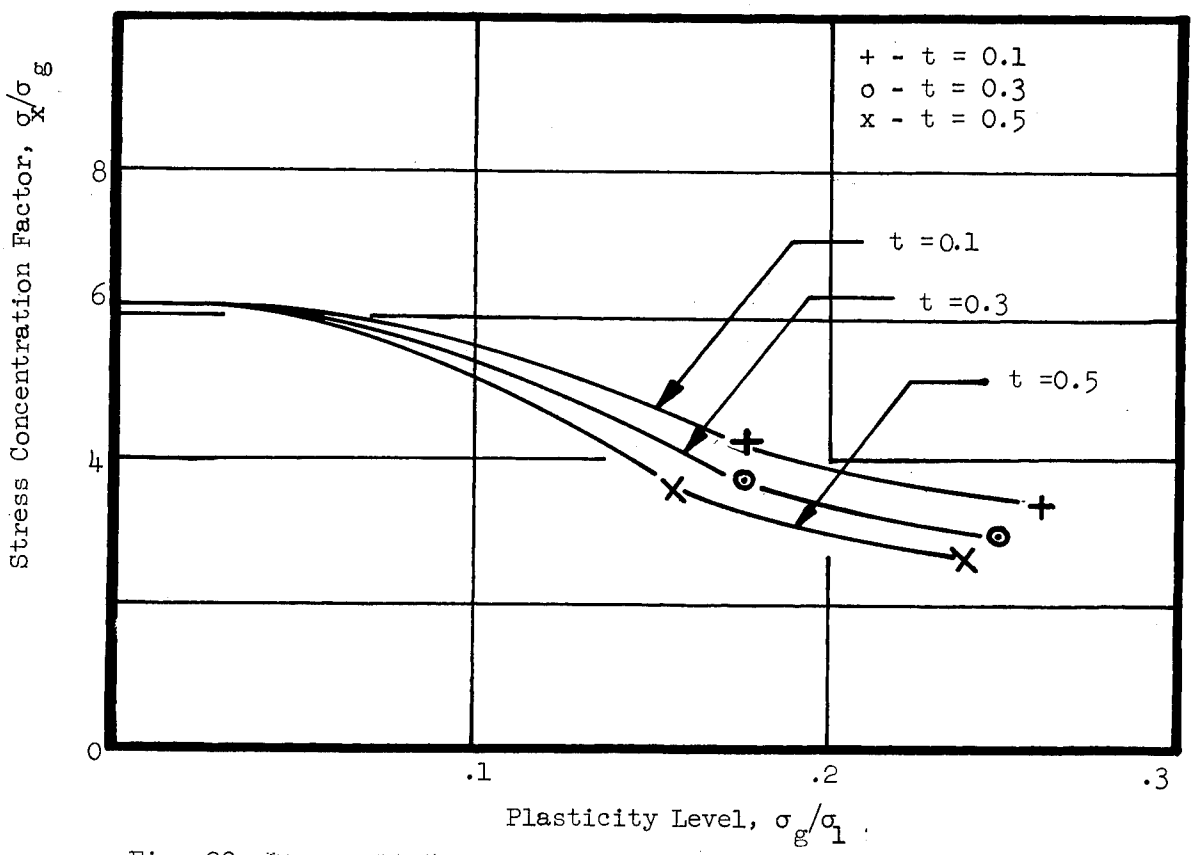

Fig. 90 Stress Concentration Factors for Various Levels of Plasticity at the Midplane for $\ell_{cr} = 0.1$.

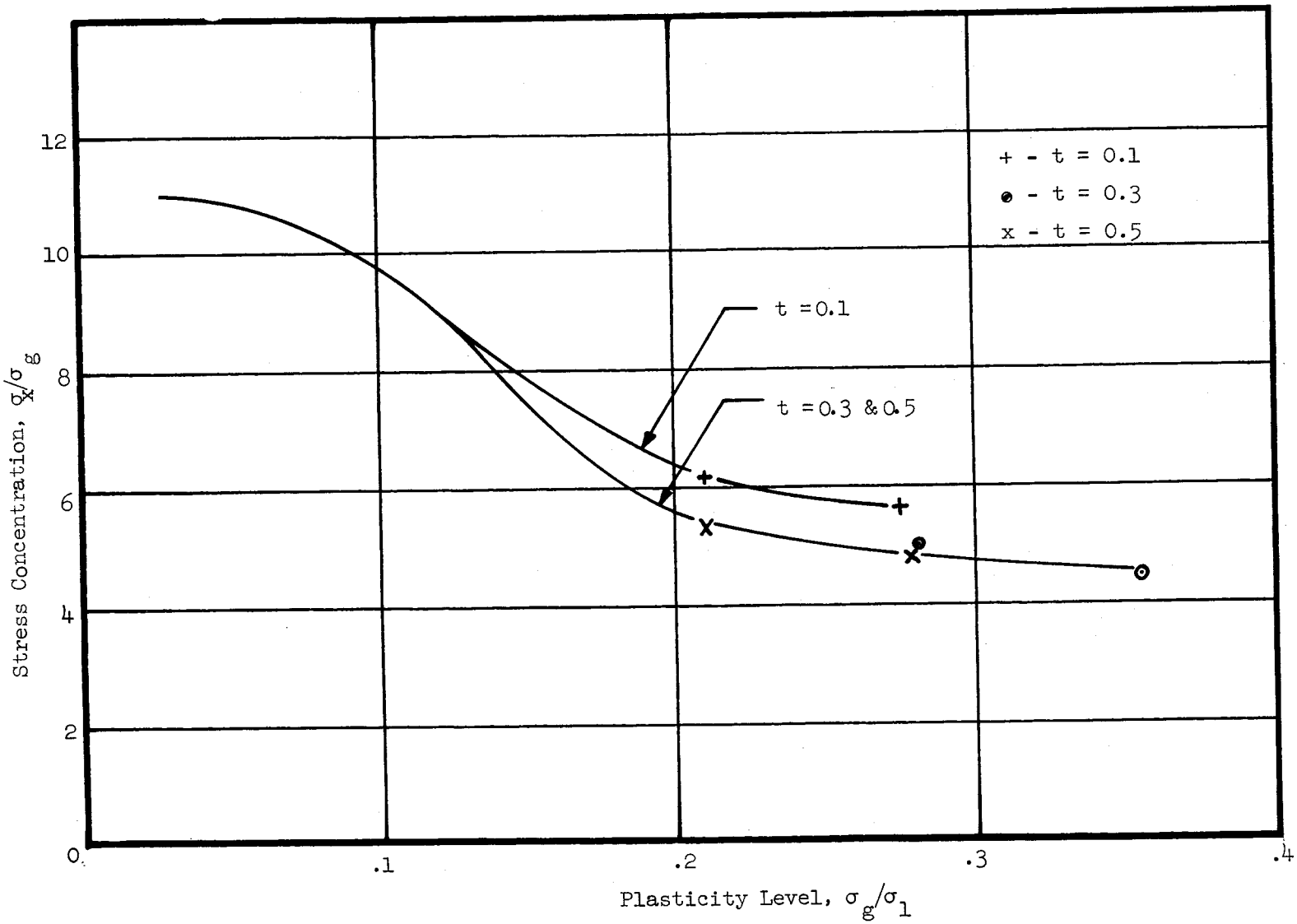

Fig. 91 Stress Concentration Factors For Various Levels of Plasticity, Midplane ℓ_{cr} = .5

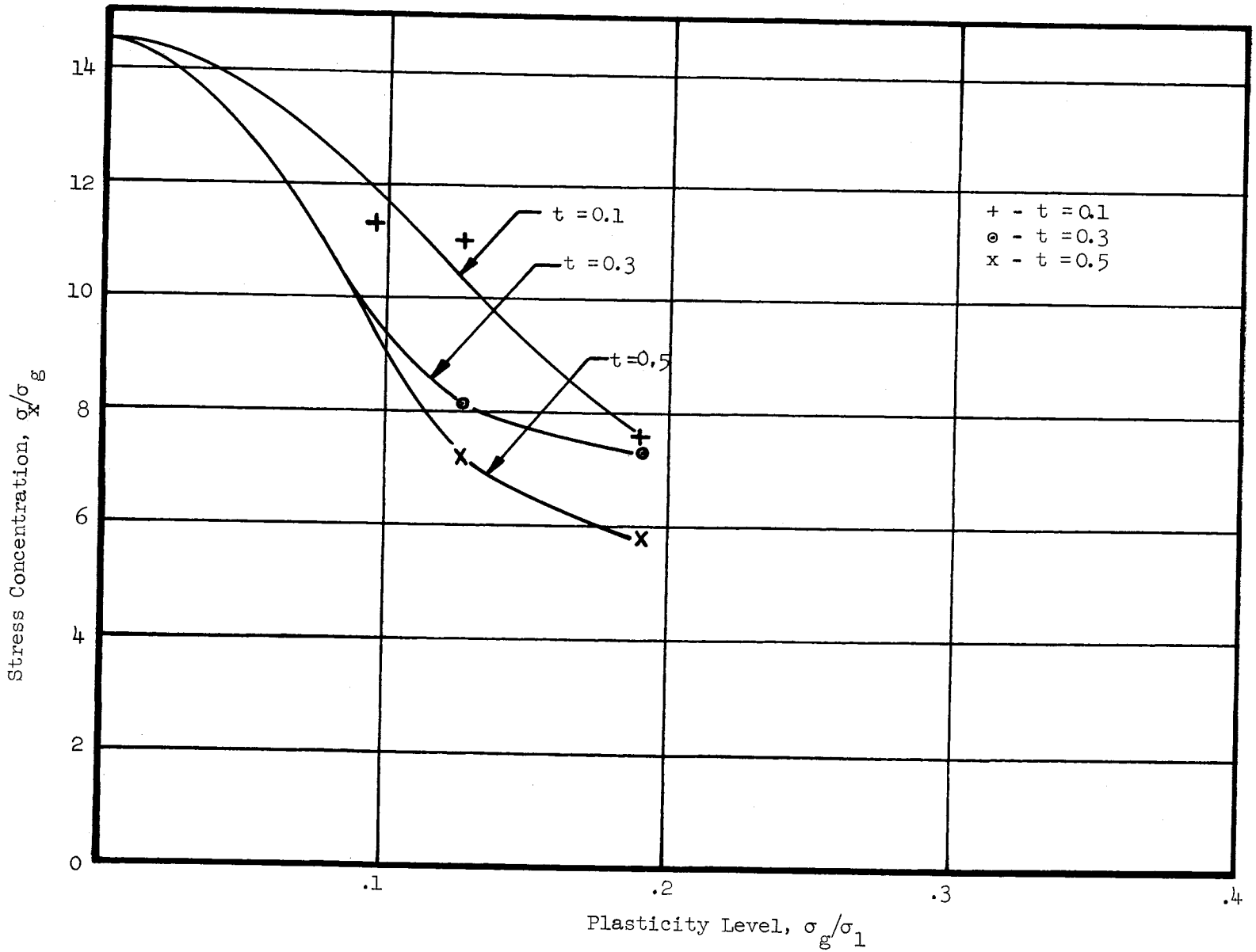

Fig. 92 Stress Concentration Factors for Various Levels of Plasticity, Midplane $\ell_{cr} = 0.8$

plates and do not come together at the higher plasticity levels as was the tendency at the surface. It is realized that based on the limited number of data points perhaps too much significance may be placed on these trends and that the stress concentration curves would be more reasonably represented by average curves. However, the trends do appear to exist and the figures representing stress concentration factors are presented in their present form to stimulate discussion.

The maximum σ_z stress measured at the midplane is plotted as a function of the plate thickness in Figs. 93 through 95. For the 0.8 crack length (Fig. 93) the maximum σ_z as a function of plate thickness exhibits the same general trend as observed for the 0.5 in. crack length (Fig. 94). However, higher values are observed for the 0.8 crack length. For the 0.1 in. crack length (Fig. 95), a rather unusual behavior is indicated for the maximum σ_z stress as a function of plate thickness. The points on the curves in Fig. 95 are not for the same gross stress (σ_g) but are close enough to indicate the behavior as shown by the curves. An explanation for this behavior is not available. However, it should be noted that each point in Fig. 95 represents an individual test and test specimen. Should this behavior be attributed to experimental error, it is unlikely that the two curves would show the same trend.

Utilizing the elasto-plastic stress distributions and the distortion energy theory, the approximate elastic-plastic boundaries through plate thickness were determined. Based on the distortion energy theory, principal stresses are related to the uniaxial yield stress (σ_o) in the following manner:

$$(\bar{\sigma}_x - \sigma_z)^2 + (\sigma_z - \sigma_y)^2 + (\sigma_y - \bar{\sigma}_x)^2 = 2\sigma_o^2 \qquad (14)$$

where σ_o = proportional limit (600 psi, reference Fig. 34). From measured values of σ_y and σ_z at a point, a $\bar{\sigma}_x$ was computed which represents the σ_x stress value at yield required to support the measured σ_y and σ_z. If the measured σ_x stress is greater than the $\bar{\sigma}_x$ stress then the point is in the plastic state. The location at which σ_x equals $\bar{\sigma}_x$ represents the elastic-plastic boundary. Figures 96 through 101 show

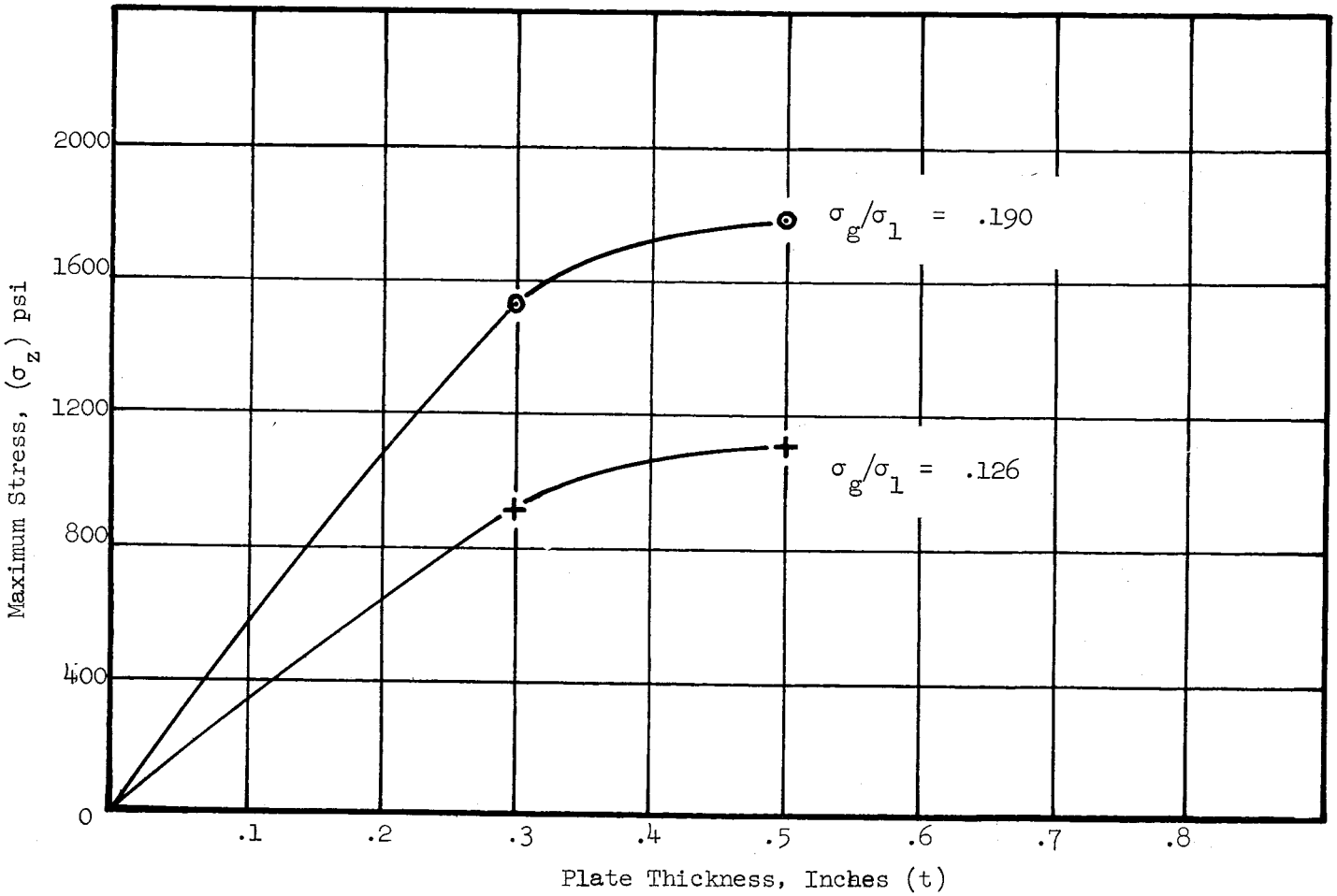

Fig. 93 Maximum Stress (σ_z) Measured at z = 0 For ℓ_{cr} = 0.8

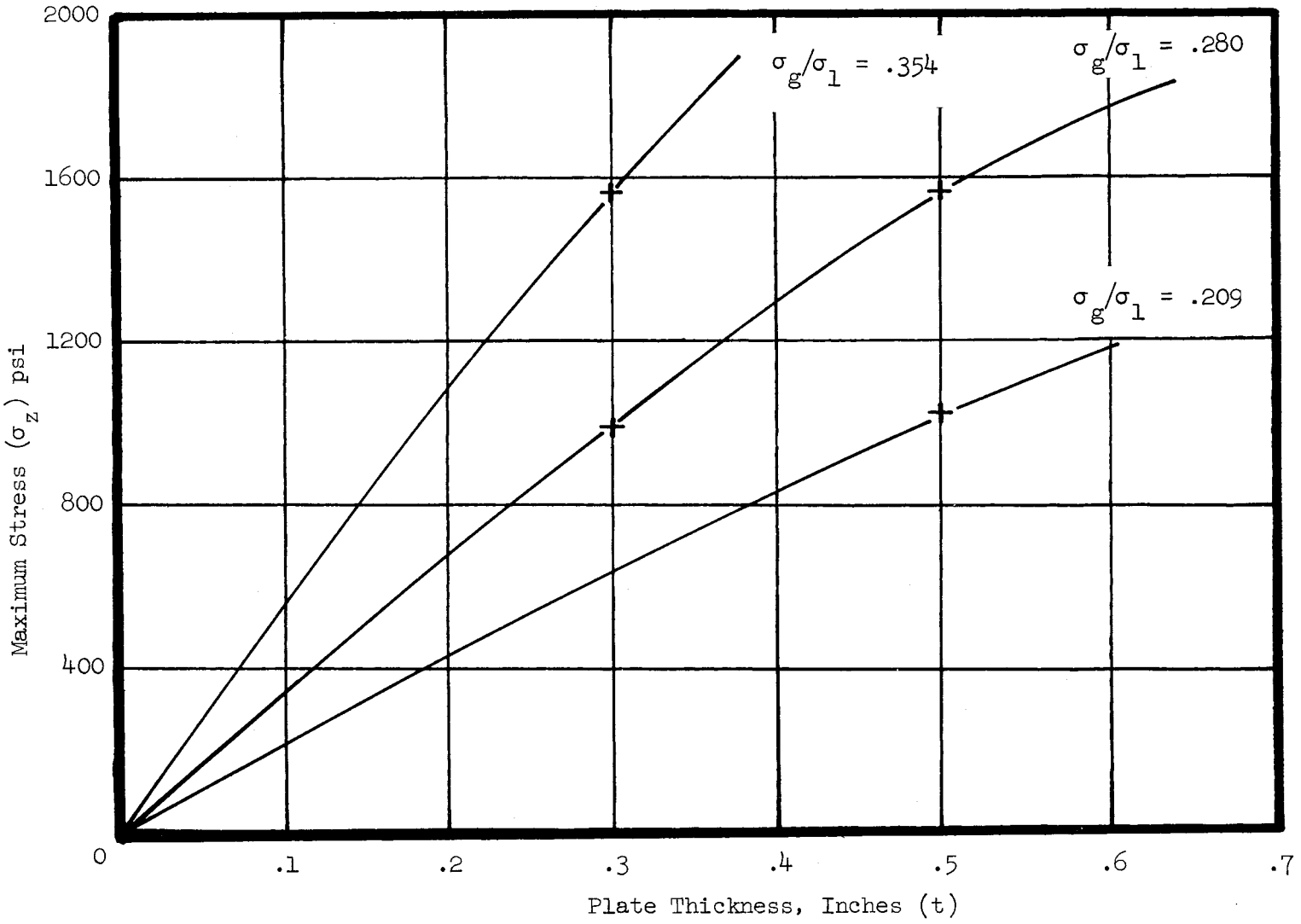

Fig. 94 Maximum Stress (σ_z) Measured at z = 0 For ℓ_{cr} = 0.5

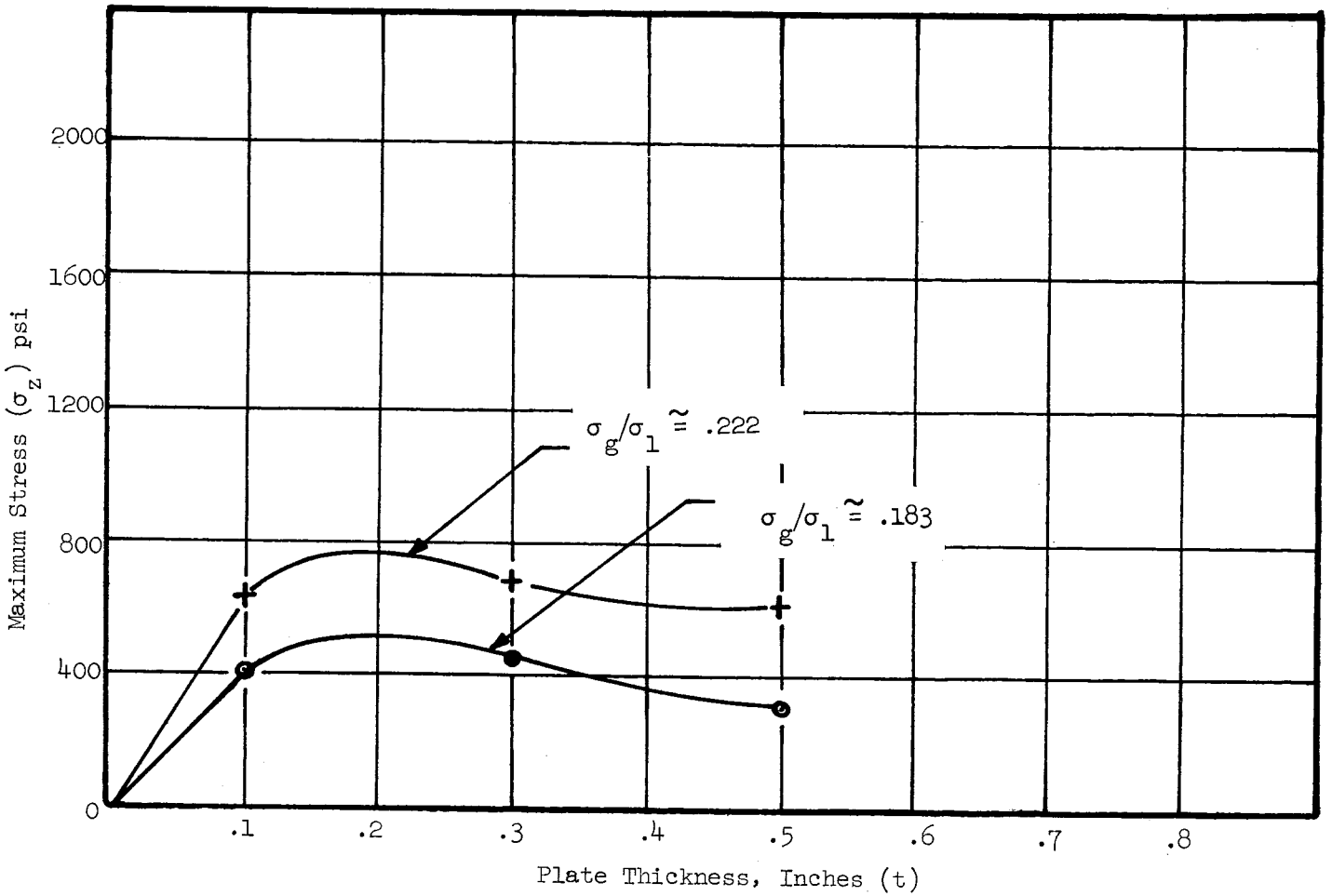

Fig. 95 Maximum Stress (σ_z) Measured at z = 0 for ℓ_{cr} = 0.1

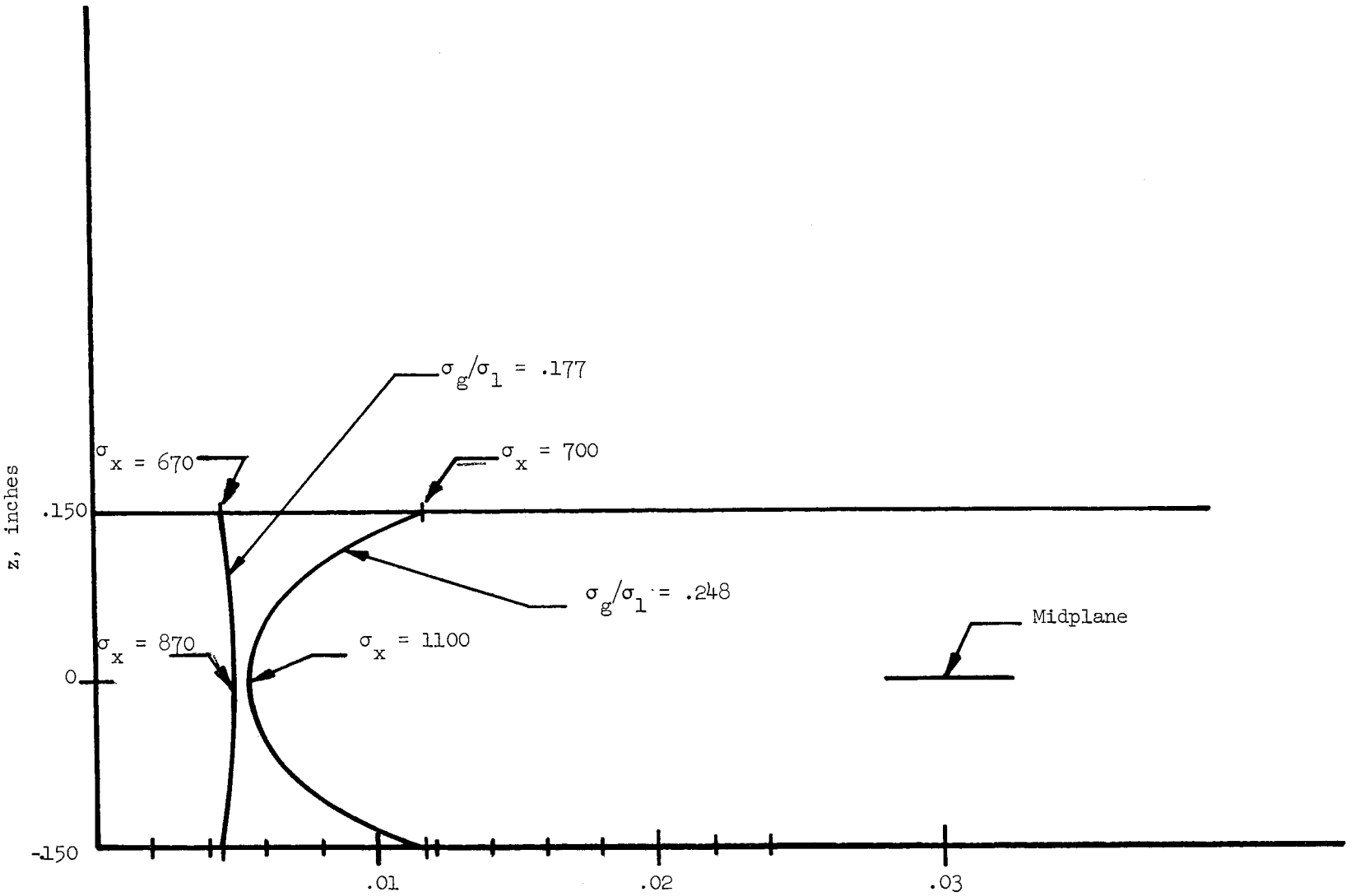

Fig. 96 Plastic Zone Penetration Through Thickness For ℓ_{cr} =0.1 and t =0.3

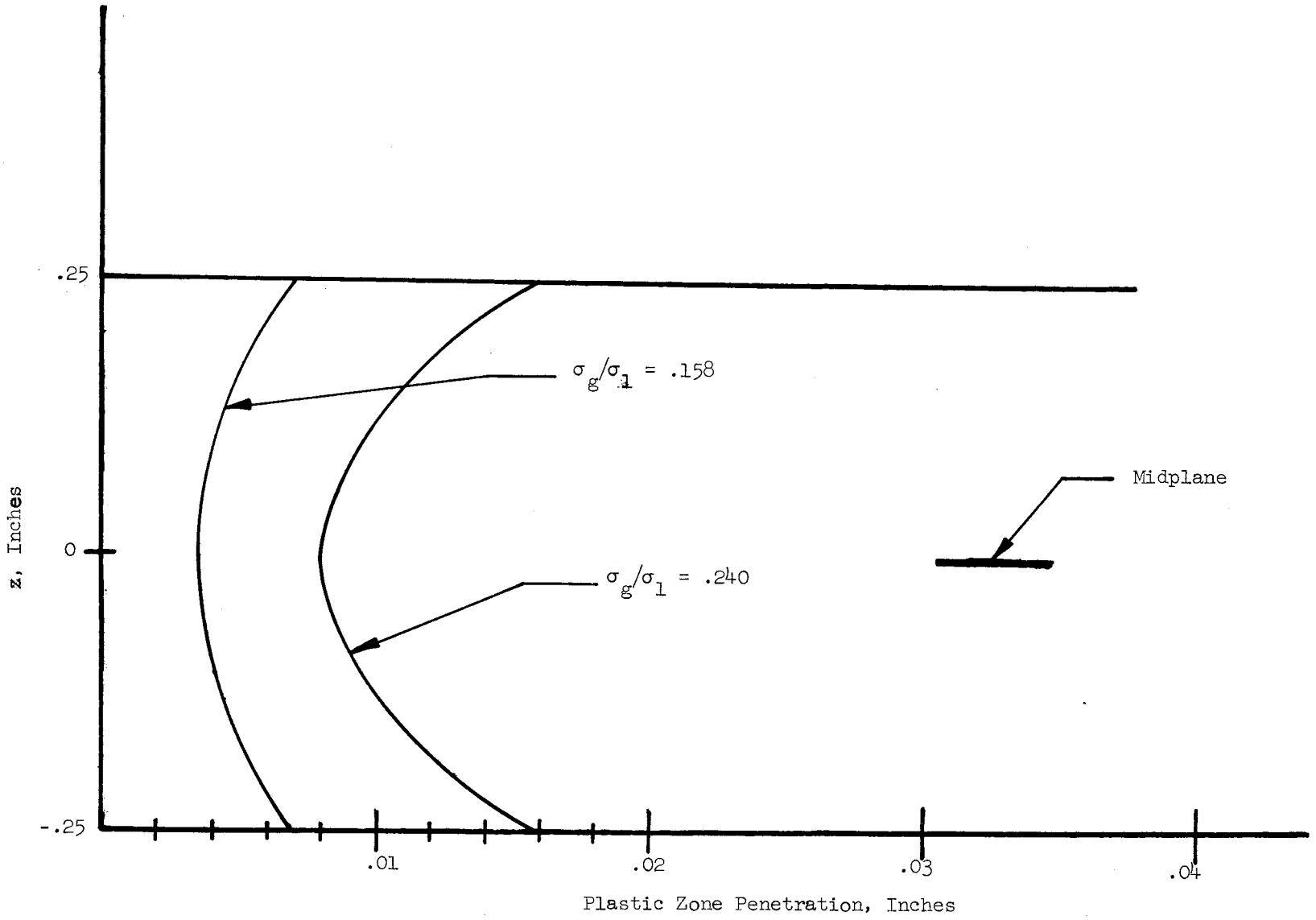

Fig. 97 Plastic Zone Penetration Through Thickness For ℓ_{cr} = 0.1 and t = 0.5

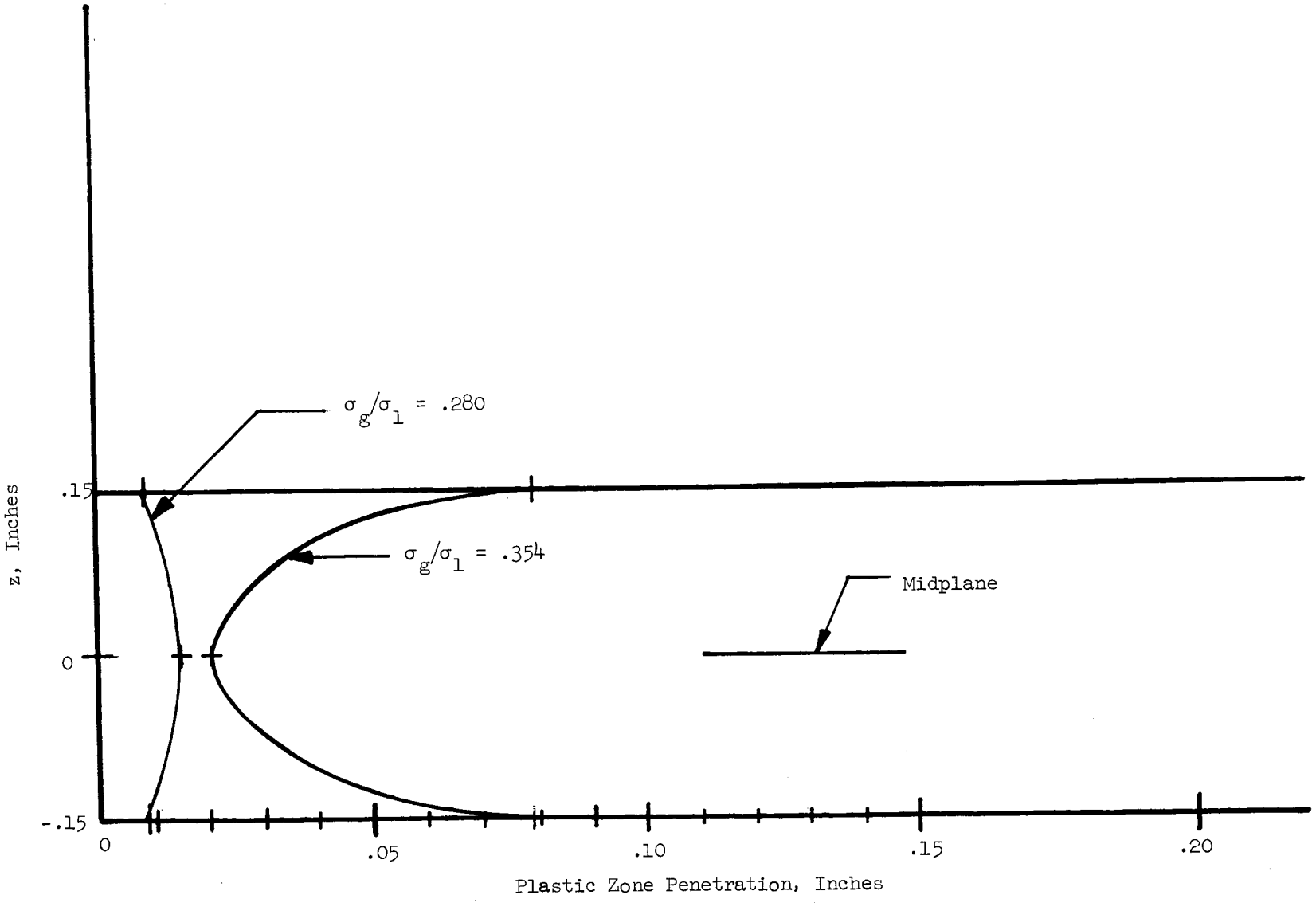

Fig. 98 Plastic Zone Penetration Through Thickness For ℓ_{cr} = 0.5 and t = 0.3

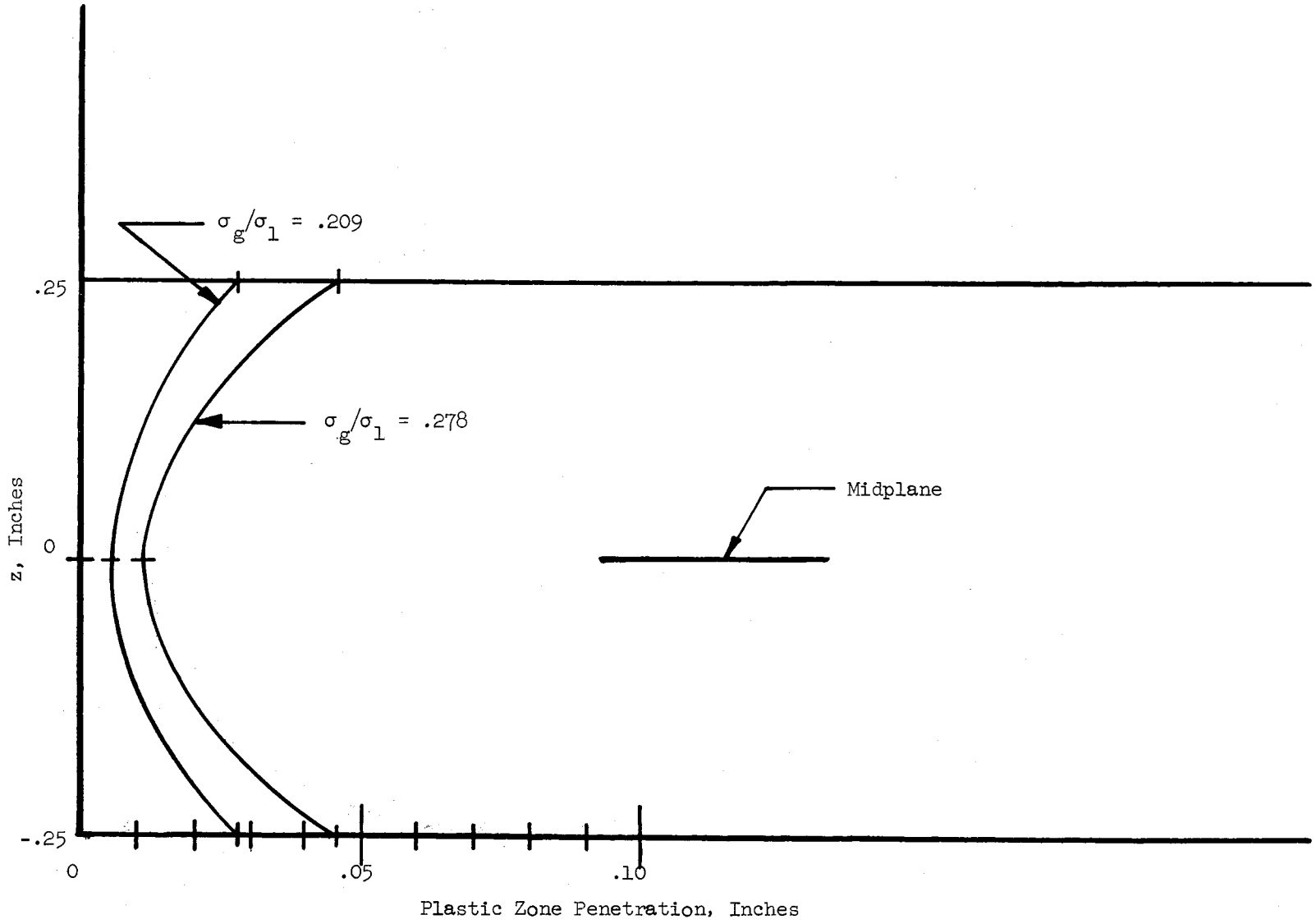

Fig. 99 Plastic Zone Penetration Through Thickness for ℓ_{cr} = 0.5 and t = 0.5

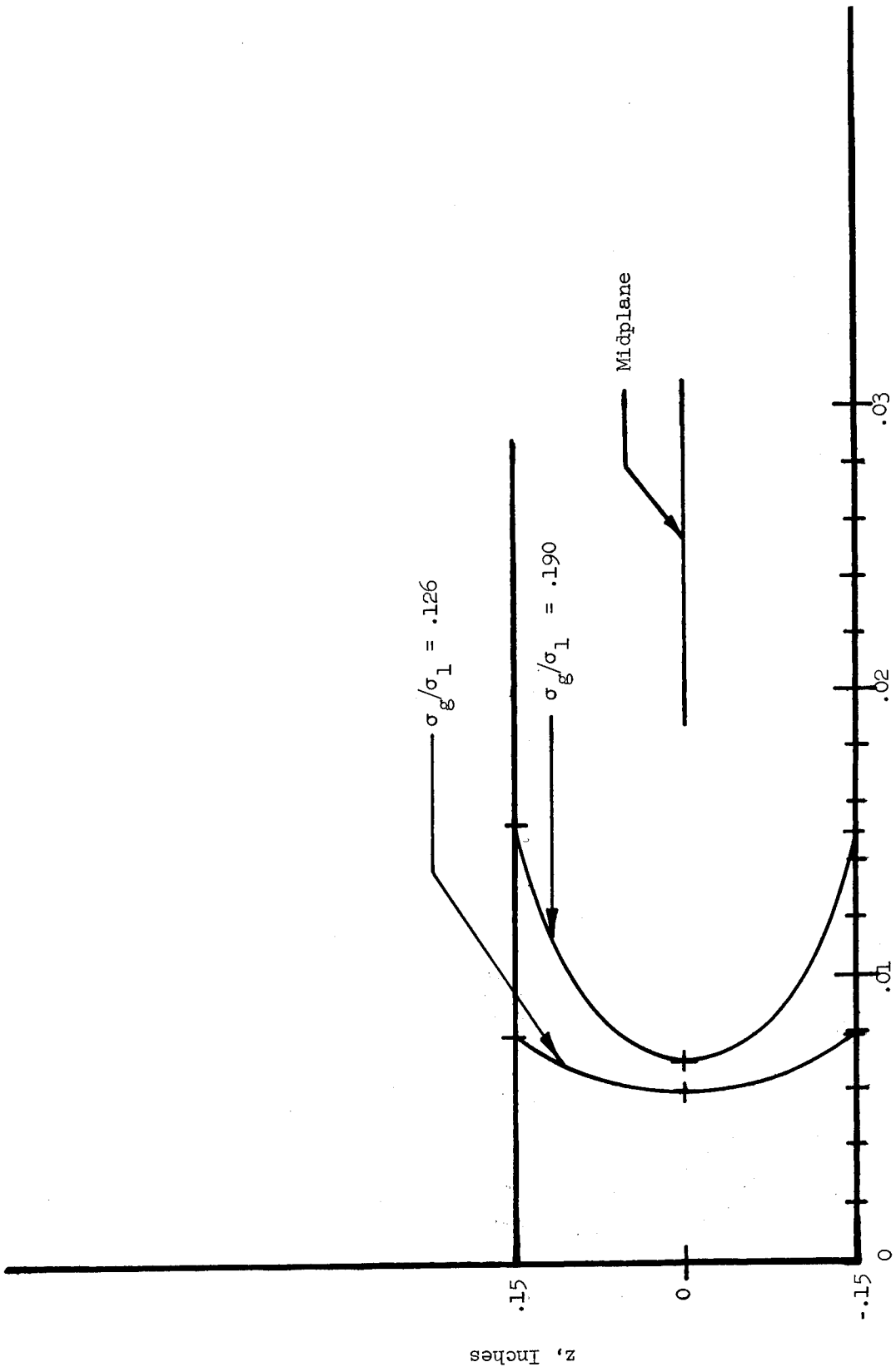

Plastic Zone Penetration, Inches

Fig. 100 Plastic Zone Penetration Through Thickness For ℓ_{cr} =0.8 and t =0.3

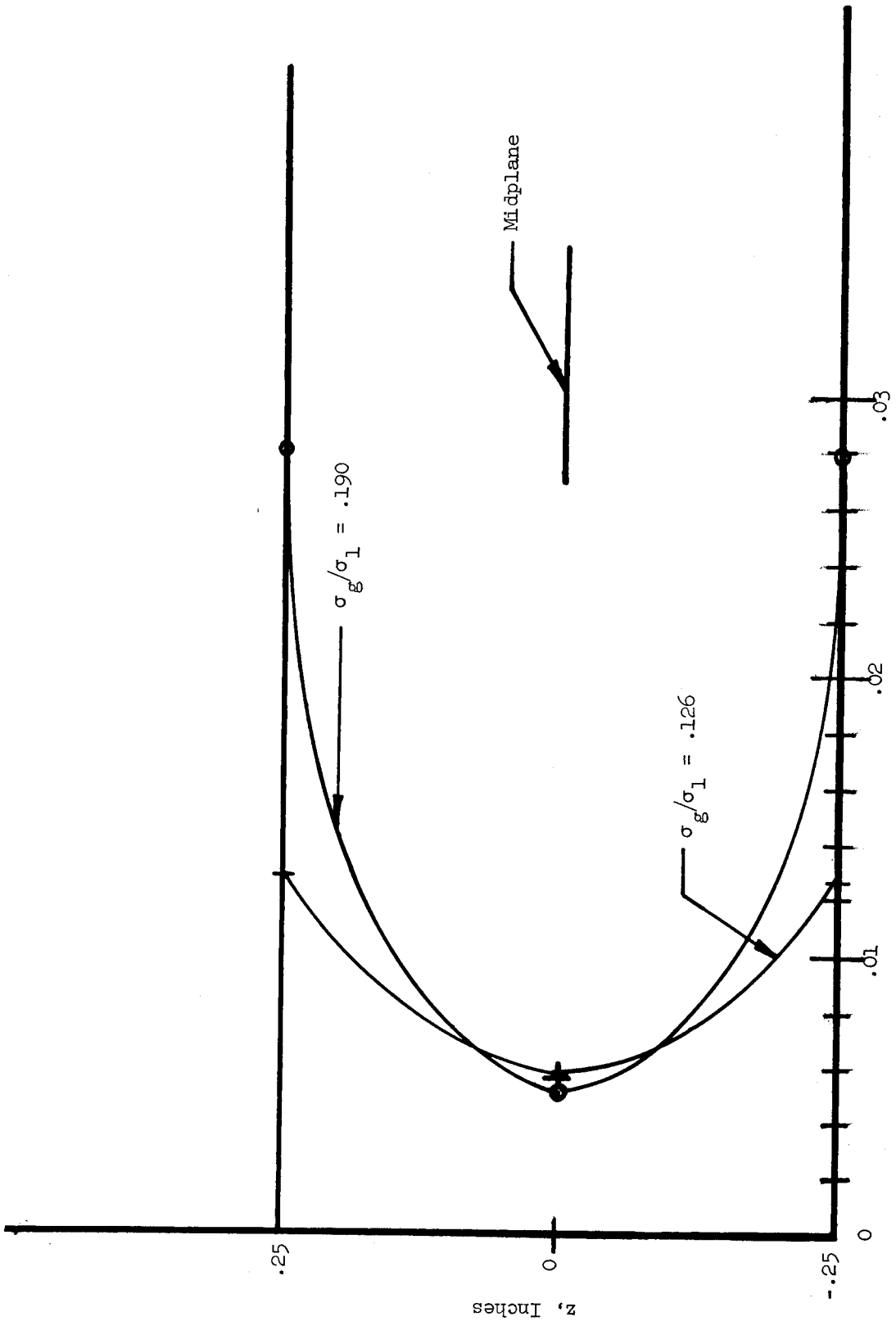

Fig. 101 Plastic Zone Penetration Through Thickness For ℓ_{cr} = 0.8 and t = 0.5

the elastic-plastic boundary through the plate thickness. These figures indicate that the plastic zone penetration extends farther from the crack tip at the surface than at the midplane yet the stresses at the elastic-plastic boundary of the midplane are much higher than at the elastic-plastic boundary at the surface. This is caused by the higher yield condition at the midplane. For example, consider Fig. 96, σ_g/σ_1 is equal to 0.248. The σ_x stress at the elastic-plastic boundary for the surface is 700 psi while for the midplane σ_x is 1100 psi. For the lower level of plasticity ($\sigma_g/\sigma_1 = 0.177$) the σ_x stress at the elastic-plastic boundary of the surface is 670 psi while for the midplane σ_x is 870. This indicates that the stress condition for the surface has not increased significantly due to the higher loading, but the higher loading has increased the plastic zone penetration. On the other hand at midplane, the plastic zone penetration has increased only slightly but the yield condition has increased almost 30 percent. In general the same type of behavior is observed in the other figures (Figs. 97 through 101). This, in effect, is compatible with observations of fracture surfaces for thick aluminum plates, i.e., crack propagation by brittle fracture at the midplane resulting in the "tunneling" effect.

Therefore, the elastic-plastic boundaries through the thickness indicate a tendency toward midplane brittle fracture and surface yielding (tunneling effect). In addition, two specimens fractured inadvertently during the elasto-plastic stress freezing operation. Nevertheless, examination of these fracture surfaces is very significant in that it further illustrates the above mentioned "tunneling" effect.

Figure 102 shows the crack configuration in a transverse slice for $\ell_{cr} = 0.8$ and $t = 0.5$. This crack has initiated at the midplane but has not propagated far enough to extend to the surface. Yet, already it exhibits the tunneling configuration. Figure 103 represents the complete fracture surface of another specimen of $\ell_{cr} = 0.8$ and $t = 0.5$. Here again the "tunneling" effect and midplane brittle fracture is indicated. Figure 104 represents the fracture surface for a specimen with $\ell_{cr} = 0.1$ and $t = 0.5$, indicating the same phenomena.

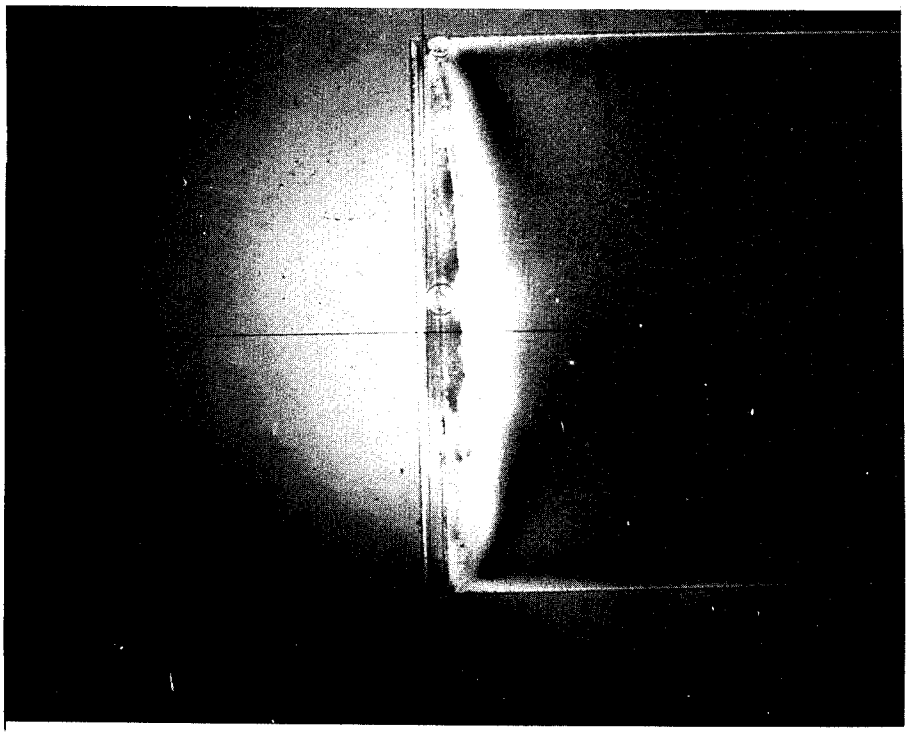

Fig. 102 Crack Initiated in a Plate of ℓ_{cr} = 0.8 and t = 0.5 as Viewed in Transverse Slice

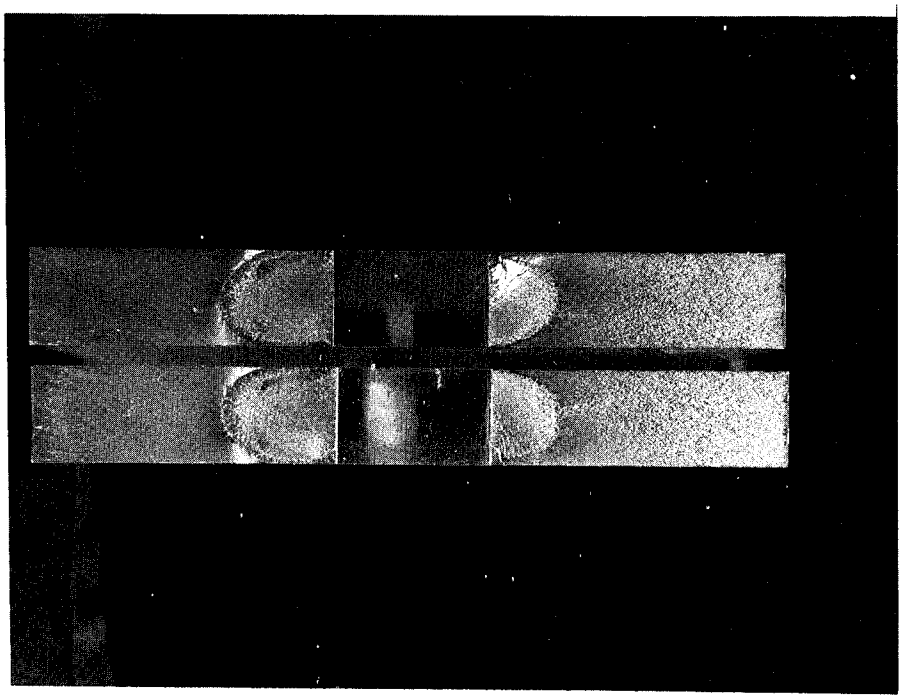

Fig. 103 Fracture Surface for Plate with ℓ_{cr} = 0.8 and t = 0.5

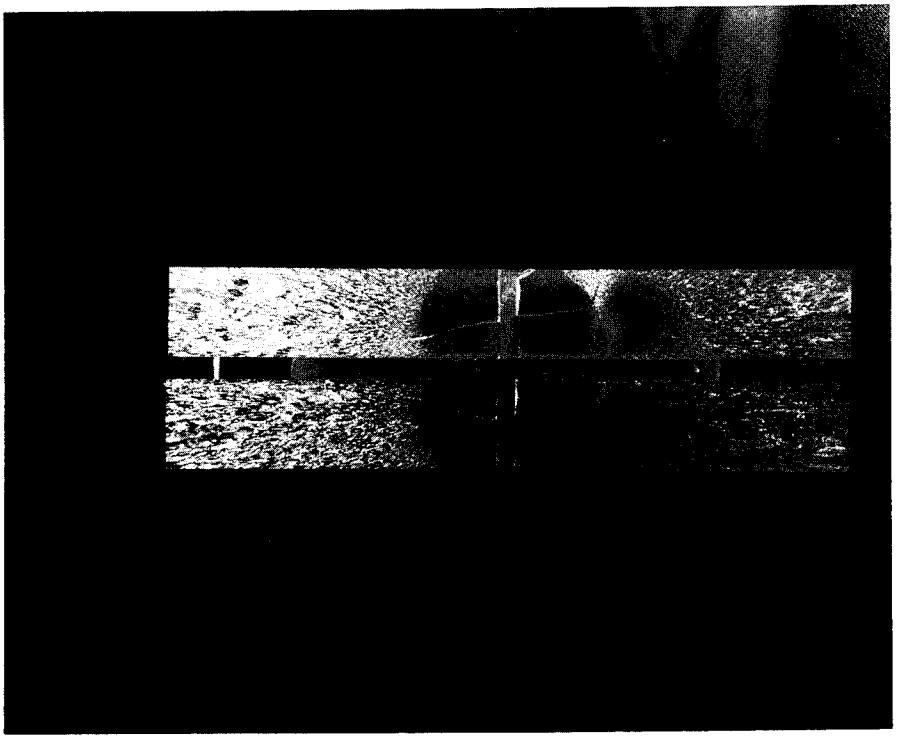

Fig. 104 Fracture Surface for Plate with $\ell_{cr} = 0.1$ and $t = 0.5$

Section 7
CONCLUSIONS

Based upon the experimental work of this program concerning the development and application of the photoelasto-plastic method to study the stresses associated with plastic flow in the vicinity of a simulated crack, the following conclusions have been reached:

- It is possible to generate an effective stress-strain curve similar to an aluminum alloy by the "frozen" stress technique using an appropriate thermal cycle whose maximum temperature is significantly below the critical temperature of the model material.
- The above-mentioned method can be used to determine the stress concentration factors in infinite plates with centrally located holes for elasto-plastic situations.
- The method also yields realistic information concerning stress concentration factors and stress variation through plate thickness caused by plastic flow in plates with centrally located simulated cracks. No theory exists for an accurate comparison.
- This method also yields the same type of fracture surface (tunneling) for thick plates as has been observed for aluminum alloys.

Section 8

REFERENCES

1. H. Neuber, "Theory of Notch Stresses," AEC-TR 4547, 1961
2. M. W. Brossman, and T. A. Kies, "Energy Release Rates During Fracturing of Perforated Plates," U. S. Naval Research Laboratory, Memorandum Report No. 370, April 1955
3. A. Wells, and D. Post, "The Dynamic Stress Surrounding a Running Crack – A Photoelastic Analysis," Proceedings of the Society for Experimental Stress Analysis, XVI, No. 1, 1957, pp. 69–92
4. J. Dixon, "Stress Distribution Around a Central Crack in a Plate Loaded in Tension; Effect of Finite Width of Plate," Journal Roy. Aeron. Soc., Vol. 64, 1960, pp. 141–145
5. J. Dixon, "Some Studies of Elastic-Plastic Strain Distributions in Flat Bars Containing Holes and Notches," DSIR Report No. PM 303, National Engineering Laboratory, East Kilbride, Glasgow, 1961
6. K. Kawata, "Analysis of Elasto-Plastic Behavior of Metals by Means of Photoelastic Coating Method," Jour. Sci. Res. Inst., Vol. 52, Tokyo, 1958, pp. 17–40
7. W. Gerberich, "Stress Distribution About a Slowly Growing Crack Determined by Photoelastic Coating Method," Experimental Mechanics, Dec 1962, p. 359
8. M. Frocht, and M. Leven, "On the State of Stress in Thick Bars," J. App. Phys., 13 May 1942
9. W. Ramberg, and W. Osgood, "Description of Stress-Strain Curves by Three Parameters," NACA TN 902, July 1943
10. J. B. Alblas, "Theorie von de driedimensionale spanningstoestand in een doorboorde ploat," Amsterdam, 1957

11. B. Budiansky, and R. Videnšek, "Analysis of Stresses in the Plastic Range Around a Circular Hole in a Plate Subjected to Uniaxial Tension," NACA TN 3542

12. H. Neuber, "Theory of Stress Concentration for Shear-Strained Prismatical Bodies With Arbitrary Nonlinear Stress-Strain Law," J. Appl. Mechanics, Dec 1961, p. 544

13. H. Hardrath and L. Ohman, "A Study of Elastic and Plastic Stress Concentration Factors Due to Notches and Fillets in Flat Plates," NACA Report 1117

14. ANC-5 Handbook

15. Inglis, Trans. Naval Architects London, Vol. 60, p. 219, 1913

16. M. Frocht, "Photoelasticity," Vol. 2, John Wiley & Sons

"The aeronautical and space activities of the United States shall be conducted so as to contribute . . . to the expansion of human knowledge of phenomena in the atmosphere and space. The Administration shall provide for the widest practicable and appropriate dissemination of information concerning its activities and the results thereof."

—NATIONAL AERONAUTICS AND SPACE ACT OF 1958

NASA SCIENTIFIC AND TECHNICAL PUBLICATIONS

TECHNICAL REPORTS: Scientific and technical information considered important, complete, and a lasting contribution to existing knowledge.

TECHNICAL NOTES: Information less broad in scope but nevertheless of importance as a contribution to existing knowledge.

TECHNICAL MEMORANDUMS: Information receiving limited distribution because of preliminary data, security classification, or other reasons.

CONTRACTOR REPORTS: Technical information generated in connection with a NASA contract or grant and released under NASA auspices.

TECHNICAL TRANSLATIONS: Information published in a foreign language considered to merit NASA distribution in English.

SPECIAL PUBLICATIONS: Information derived from or of value to NASA activities. Publications include conference proceedings, monographs, data compilations, handbooks, sourcebooks, and special bibliographies.

TECHNOLOGY UTILIZATION PUBLICATIONS: Information on technology used by NASA that may be of particular interest in commercial and other nonaerospace applications. Publications include Tech Briefs; Technology Utilization Reports and Notes; and Technology Surveys.

Details on the availability of these publications may be obtained from:

SCIENTIFIC AND TECHNICAL INFORMATION DIVISION

NATIONAL AERONAUTICS AND SPACE ADMINISTRATION

Washington, D.C. 20546